Two-dimensional constrained anisotropic inversion of magnetotelluric data

vorgelegt von
Diplom-Ingenieur (Angewandte Geophysik)
Xiaoming Chen

von der
Mathematisch-Naturwissenschaftlichen Fakultät
der Universität Potsdam
zur Erlangung des akademischen Grades
Doktor der Naturwissenschaften
-Dr. rer. nat.-
genehmigte Dissertation

Potsdam 2012

Published online at the
Institutional Repository of the University of Potsdam:
URL http://opus.kobv.de/ubp/volltexte/2012/6316/
URN urn:nbn:de:kobv:517-opus-63163
http://nbn-resolving.de/urn:nbn:de:kobv:517-opus-63163

Betreuerin: Dr. Ute Weckmann

Gutachter:
1. Gutachterin: Dr. Ute Weckmann (Universität Potsdam, GeoForschungsZentrum Potsdam)
2. Gutachter: Prof. Dr. Michael Weber (Universität Potsdam, GeoForschungsZentrum Potsdam)
3. Gutachter: Prof. Dr. Josef Pek (Academy of Science, Czech Republik)

Tag der wissenschaftlichen Aussprache: 15. 11. 2012

Eidesstattliche Erklärung

Hiermit versichere ich, dass ich meine Dissertation selbstständig verfasst und keine anderen als die angegebenen Quellen und Hilfsmittel benutzt habe, alle Ausführungen, die anderen Schriften wörtlich oder sinngemäß entnommen wurden, kenntlich gemacht sind und die Arbeit in gleicher oder ähnlicher Fassung noch nicht Bestandteil einer Studien- oder Prüfungsleistung war.

Unterschrift des Verfassers

Zusammenfassung

Tektonische und geologische Prozesse verursachen häufig eine strukturelle Anisotropie des Untergrundes, welche von verschiedenen geophysikalischen Methoden beobachtet werden kann. Zur Erstellung und Interpretation geeigneter, realistischer Modelle der Erde sind Inversionsalgorithmen notwendig, die einen anisotropen Untergrund einbeziehen können. Für die vorliegende Arbeit habe ich einen magnetotellurischen (MT) Datensatz vom Cape Fold Gürtel in Südafrika untersucht. Diese Daten weisen auf eine ausgeprägte Anisotropie der Kruste hin, da z.B. die MT Phasen außerhalb des erwarteten Quadranten liegen und nicht durch standardisierte isotrope Inversionsalgorithmen angepasst und ausgewertet werden können. Um dieses Problem zu beheben, habe ich eine zweidimensionale Inversionsmethode entwickelt, welche eine anisotrope elektrische Leitfähigkeitsverteilungen in den Modellen zulässt.

Die MT Inversion ist im allgemeinen ein nichtlineares, schlecht gestelltes Minimierungsproblem mit einer hohen Anzahl an Freiheitsgraden. Im isotropen Fall wird jeder Gitterzelle eines Modells ein elektrischer Leitfähigkeitswert zugewiesen um den Erduntergrund nachzubilden. Ein Modell mit beispielsweise 100 x 50 Zellen besitzt 5000 unbekannte Modellparameter. Im Gegensatz dazu haben wir im anisotropen Fall die sechsfache Anzahl, da hier aus dem einfachen Zahlenwert der elektrischen Leitfähigkeit ein symmetrischer, reellwertiger Tensor wird, wobei die Anzahl der Daten gleich bleibt. Für die erfolgreiche Inversion von anisotropen Leitfähigkeiten und um die Nicht-Eindeutigkeit der Lösung des inversen Problems zu überwinden, ist eine geeignete Einschränkung der möglichen Modelle absolut notwendig. Dies wird umso wichtiger, da die Sensitivität von MT Daten nicht für alle Anisotropieparameter gleich ist. In der vorliegenden Arbeit habe ich einen Algorithmus entwickelt, welcher die Lösung des anisotropen Inversionsproblems unter Minimierung einer globalen Straffunktion berechnet. Diese besteht aus drei Teilen: der Datenanpassung, den Zusatzbedingungen an die Glätte des Modells und die Anisotropie. Im Gegensatz dazu werden beim isotropen Fall nur die ersten zwei Parameter minimiert. Der neu definierte Anisotropieterm wird mit Hilfe der Summe der quadratischen Abweichung der Hauptleitfähigkeitswerte des Modells gemessen. Die grundlegende Idee dieser Zusatzbedingung ist einfach. Falls ein isotropes Modell die Daten ausreichend gut anpassen kann, wird keine elektrische Anisotropie zusätzlich in das Modell eingefügt.

Der vorgestellte Inversionsalgorithmus verwendet die Finite-Volumen-Methode und ist in das Modellierungs- und Inversionsprogrammpaket ModEM (Egbert and Kelbert, 2012) eingearbeitet. Das Grundgerüst hinter ModEM sind allgemein anwendbare Vorwärtsmodellierungs-, Inversions- und Hilfsroutinen, welche durch spezielle Anwendungen erweitert werden können.

In meiner Erweiterung des Programmpakets werden die Glätte des Modells und die Nebenbedingungen an die Anisotropie auf den gesamten Modellraum angewendet und die globale Straffunktion wird mit Hilfe des Levenberg-Marquardt-Verfahrens, welches auf der bekannten Gauss-Newton Methode basiert, minimiert .

Die Sensitivitätsmatrix ist als die erste Ableitung der berechneten Daten nach den Modellparametern definiert und beschreibt wie stark sich die berechneten Daten bei kleinen Modifizierungen der Modellparameter ändern. Die Berechnung dieser Matrix ist der Kernpunkt fast aller Inversionsalgorithmen. Dies gilt vor allem für Newtonverfahren. Im anisotropen Fall ist die elektrische Eigenschaft jeder Modellzelle als symmetrischer Tensor zweiter Ordnung definiert. Aus praktischen Gründen werden anstelle des vollen Tensors stellvertretend die Hauptwerte und Eulerwinkel für die numerische Berechnung verwendet. Die Berechnung der Sensitivitätsmatrix ist daher nicht direkt möglich wie im isotropen Fall. Ich stelle im Rahmen meiner Arbeit einen geeigneten Algorithmus für die Matrixberechnung bei einer anisotropen Leitfähigkeitsverteilung vor.

Um eine erfolgreiche Inversion zu garantieren müssen geeignete Regularisierungsparameter für die verschiedenen Nebenbedingungen an das Modell gewählt werden. Für eine Inversion mit solchen Nebenbedingungen wird die Straffunktion in zwei Schritten minimiert. Im ersten Schritt hofft man, dass die Datenanpassung anfangs im Vergleich zu den Nebenbedingungen an das Modell die Inversion dominiert und vorrangig großskalige Strukturen im Modell erzeugt werden. Wenn sich danach die Datenanpassung mit jedem weiteren Inversionsschritt verbessert, geht der Inversionsprozess im zweiten Schritt dazu über nur kleine Strukturen zu erzeugen und arbeitet lediglich an der Feinabstimmung des Endmodells. Die Anwendung einer geeigneten Regularisierung des Problems strebt danach den "optimalen" Übergang zwischen diesen beiden Stadien der Inversion festzulegen und das "richtige" Inversionsmodell zu finden. Tests mit synthetischen Modellen zeigen, dass bei festgesetzten Regularisierungsparametern die Inversion meistens entweder in einem glatten Modell mit hohem RMS Fehler oder einem groben Modell mit kleinem RMS Fehler endet. Dies weist im ersten Fall auf eine Inversion hin, bei der der erste Schritt kaum ausgeführt wurde und im zweiten Fall auf eine Inversion, bei der der erste Schritt dominiert und wenig oder gar keine Feinheiten in das Modell eingearbeitet wurden. Die Anwendung einer Relaxationsbedingung auf die Regularisierung nach jedem Iterationsschritt resultiert in glatteren Inversionsmodellen und einer höheren Konvergenz und scheint ein ausgereifter Weg zur Wahl der Parameter zu sein. Die vorgestellte Inversionsmethode ist im allgemeinen in der Lage die Hauptleitfähigkeiten in der horizontalen Ebene zu finden. Wenn keine der Hauptrichtungen der Anisotropiestruktur mit der vorgegebenen Streichrichtung übereinstimmt, können nur die dazugehörigen effektiven Leitfähigkeiten, welche

die Projektion der Hauptleitfähigkeiten auf die Koordinatenachsen des Modells darstellen, aufgelöst werden. Allerdings gehen die Informationen über die Rotationswinkel verloren.

Am Ende meiner Arbeit werden die MT Daten des Cape Fold Gürtels in Südafrika analysiert. Die MT Daten zeigen in einem Abschnitt des Messprofils (> 10 km) Phasen über $90°$. Dieser Teil der Daten kann nicht mit herkömmlichen isotropen Modellierungsverfahren angepasst und daher mit diesen auch nicht vollständig ausgewertet werden. Die vorgestellte Inversionsmethode konnte die außergewöhnlich hohen Phasenwerte nicht wie gewünscht im Inversionsergebnis erreichen, was mit dem erwähnten Informationsverlust der Rotationswinkel begründet werden kann. MT Phasenaußerhalb des ersten Quadranten können für gewöhnlich bei Anomalien mit geneigter Streichrichtung der Anisotropie gemessen werden. Um diese auch in den Inversionsergebnissen zu erreichen ist eine Weiterentwicklung des Algorithmus notwendig. Vorwärtsmodellierungen des MT Datensatzes haben allerdings gezeigt, dass eine hohe Leitfähigkeitsheterogenität an der Oberfläche in Kombination mit einer Zone elektrischer Anisotropie in der mittleren Kruste notwendig sind um die Daten anzupassen. Aufgrund geologischer und tektonischer Informationen kann diese Zone in der mittleren Kruste als tiefer Aquifer interpretiert werden, der im Zusammenhang mit den zerrütteten Gesteinen der Table Mountain Group des Cape Fold Gürtels steht.

Summary

Tectonic and geological processes on Earth often result in structural anisotropy of the subsurface, which can be imaged by various geophysical methods. In order to achieve appropriate and realistic Earth models for interpretation, inversion algorithms have to allow for an anisotropic subsurface. Within the framework of this thesis, I analyzed a magnetotelluric (MT) data set taken from the Cape Fold Belt in South Africa. This data set exhibited strong indications for crustal anisotropy, e.g. MT phases out of the expected quadrant, which are beyond of fitting and interpreting with standard isotropic inversion algorithms. To overcome this obstacle, I have developed a two-dimensional inversion method for reconstructing anisotropic electrical conductivity distributions.

The MT inverse problem represents in general a non-linear and ill-posed minimization problem with many degrees of freedom: In isotropic case, we have to assign an electrical conductivity value to each cell of a large grid to assimilate the Earth's subsurface, e.g. a grid with 100×50 cells results in 5000 unknown model parameters in an isotropic case; in contrast, we have the sixfold in an anisotropic scenario where the single value of electrical conductivity becomes a symmetric, real-valued tensor while the number of the data remains unchanged. In order to successfully invert for anisotropic conductivities and to overcome the non-uniqueness of the solution of the inverse problem it is necessary to use appropriate constraints on the class of allowed models. This becomes even more important as MT data is not equally sensitive to all anisotropic parameters. In this thesis, I have developed an algorithm through which the solution of the anisotropic inversion problem is calculated by minimization of a global penalty functional consisting of three entries: the data misfit, the model roughness constraint and the anisotropy constraint. For comparison, in an isotropic approach only the first two entries are minimized. The newly defined anisotropy term is measured by the sum of the square difference of the principal conductivity values of the model. The basic idea of this constraint is straightforward. If an isotropic model is already adequate to explain the data, there is no need to introduce electrical anisotropy at all.

The proposed inversion method is implemented into a numerical finite volume framework and embedded in the ModEM modeling and inversion software package (Egbert and Kelbert, 2012). The philosophy behind the ModEM is a generally applicable set of forward modeling, inversion and auxiliary routines which can be extended by more specific applications. Within my supplement, the model roughness and the anisotropy constraints are applied for the entire model space and the global penalty functional is minimized by using the Levenberg-Marquardt method which is based on the well-known Gauss-Newton scheme.

The sensitivity matrix is defined as the first derivative of predicted data with respect to model parameters and describes how sensitive the predicted data are towards a small changes in the model parameters. The calculation of the sensitivity matrix is the key point for almost all inversion methods, especially for the Newton type method. In the anisotropic case, the electrical property of each grid cell has to be defined with a symmetric second-order tensor and for practical reason its representatives (the principal values and the Euler angles) are used for all numerical calculation instead of the tensor itself. Hence, the calculation of the sensitivity matrix is not as straightforward as it in isotropic case. In this thesis, I present an algorithm which is adequate to calculate the sensitivity matrix for an anisotropic conductivity distribution.

In order to ensure successful inversion, appropriate trade-off parameters, also known as regularization parameters, have to be chosen for the different model constraints. For an inversion containing of model constraints, the minimization of penalty functional is done in two stages. In the first step, at early stages we hope that the data misfit is dominant compared to the model constraints and hence mainly large-scale structures are created. While the data misfit decreases from iteration to iteration, the inversion process will transit into a later stage, where only small-scale structures are added. In this stage, the inversion performs a fine-tuning and only changes the appearance of the resulting model. Application of appropriate trade-off parameters aims to identify the "optimum" transition of the two stages and achieve the "best" inversion model. Synthetic tests show that using fixed trade-off parameters usually causes the inversion to end up by either a smooth model with large RMS error, which implies a premature inversion in which the early stage is barely executed, or a rough model with small RMS error, a postmature inversion result, in which the early stage is dominant for the entire inversion process and less or even no fine-tuning is performed. Using of a relaxation approach on the regularization parameters after each successful inversion iteration will result in smoother inversion model and a better convergence. This approach seems to be a sophisticated way for the selection of trade-off parameters. In general, the proposed inversion method is adequate for resolving the principal conductivities defined in horizontal plane. Once none of the principal directions of the anisotropic structure is coincided with the predefined strike direction, only the corresponding effective conductivities, which is the projection of the principal conductivities onto the model coordinate axes direction, can be resolved and the information about the rotation angles is lost.

In the end the MT data from the Cape Fold Belt in South Africa has been analyzed. The MT data exhibits an area (> 10 km) where MT phases over 90° occur. This part of data cannot be modeled by standard isotropic modeling procedures and hence can not be

properly interpreted. The proposed inversion method, however, could not reproduce the anomalous large phases as desired because of losing the information about rotation angles. MT phases outside the first quadrant are usually obtained by different anisotropic anomalies with oblique anisotropy strike. In order to achieve this challenge, the algorithm needs further developments. However, forward modeling studies with the MT data have shown that surface highly conductive heterogeneities in combination with a mid-crustal electrically anisotropic zone are required to fit the data. According to known geological and tectonic information the mid-crustal zone is interpreted as a deep aquifer related to the fractured Table Mountain Group rocks in the Cape Fold Belt.

Contents

Chapter 1.

Introduction

Magnetotellurics (MT) is an electromagnetic geophysical method. It was introduced by the French geophysicist Louis Cagniard and Russian geophysicist Andrey Nikolayevich Tikhonov in the early 1950s (see Tikhonov, 1950, Cagniard, 1953). The MT method involves measuring variations of the natural electric and magnetic fields in orthogonal directions at the Earth's surface. Thereby the electrical conductivity structure of the Earth at depths ranging from a few tens of meters to several hundreds of kilometers can be determined. With advances in instrumentation, data processing and modeling, MT has become one of the most important tools in research of the deep Earth and at shallow and drillable depths in case of exploration, site characterization and reservoir monitoring. Since a direct investigation of the conductivity in a great depth is rarely possible, the interpretation of MT measurements always represents a modeling problem, including forward and inverse modeling. The task is to find a concept (or model) of the Earth's structure on the basis of electrical conductivity distribution.

Forward modeling scheme represents the numerical simulation of measurements for a given parameter distribution which is generally represented by the solution of partial differential equations and maps the known model (model space) into its responses (predicted data, data space). Thanks to early developments (e.g. Wait, 1954, Wannamaker et al., 1987, Mackie and Madden, 1993a, and many others) the MT forward modeling problem can be solved for any dimensionality model; analytically in simple one-dimensional (1D) cases and numerically in general. However, they are all based on an assumption of a generally isotropic subsurface. Unfortunately, the real subsurface structure does not always fulfill this requirement. In some cases, only anisotropic conductors allow a consistent interpretation of MT data (Weidelt, 1999). Many studies have been done during the past four decades in order to model the effects of the electrical anisotropy on the magnetotelluric data, e.g. Reddy and Rankin (1975), Saraf et al. (1986), Osella and Martinelli (1993), Schmucker (1994), Weidelt (1999),

Pek and Verner (1997), Pek and Santos (2002). Among them the modeling code provided by Pek and Verner (1997) to simulate MT responses above a two-dimensional subsurface with anisotropic structures is only one available for scientific community and thus widely used.

Inversion schemes search the relationships between the measured data and model responses, by modifying the model until an agreement within certain thresholds is yielded. Standard inversion schemes (e.g. Constable et al., 1987, Mackie and Madden, 1993b, Newman and Alumbaugh, 2000, Siripunvaraporn et al., 2005, Egbert and Kelbert, 2012) are developed based on isotropic modeling of different dimensionality. They are widely used to simulate MT field data. Some inversion tools considering electrical anisotropy are also developed for investigation of MT data. An algorithm to solve the 1D inversion problem was developed by Pek and Santos (2002). A pioneering work towards a general anisotropic inversion for 2D MT case was presented by Li et al. (2003). Another 2D anisotropic inversion algorithm, based on the isotropic inversion algorithm presented in Rodi and Mackie (2001) and constrains the anisotropic strike to be parallel to the regional strike, was first used by Baba et al. (2006). Unfortunately, those approaches are not applied routinely. The first two approaches are in an experimental stage and still in development, the latter one is unpublished and no public access exists for scientific community. Recently, Miensopust and Jones (2011) have shown that isotropic inversions in an anisotropic medium can result in severe artifacts and lead to erroneous interpretations.

Numerous MT field experiments suggest electrical anisotropy at various levels, shallow crustal as well as lower crustal and lithospheric mantle depths (e.g. Eisel and Bahr, 1993, Mareschal et al., 1995, Eisel and Haak, 1999, Bahr et al., 2002, Leibecker et al., 2002, Heise and Pous, 2003, Weckmann et al., 2003, Baba et al., 2006, and more others). For analyzing these data sets the standard isotropic inversion schemes become inadequate. Nevertheless, anomalous phases exceeding 90° in off-diagonal components have been frequently observed in many regions. Those anomalous phases can not be modelled using isotropic 1D or 2D approaches but using anisotropic 2D approach by the presence of two anisotropic structures of oblique anisotropy strike directions (Pek and Verner, 1997, Heise and Pous, 2003, Weckmann et al., 2003). Furthermore, Heise and Pous (2003), Weckmann et al. (2003) studied the conditions necessary to induce anomalous phases in the above model. Using their anisotropic model they explained real anomalous phase data obtained in the Variscan terrenes and Namibia.

Within the framework of the German - South African geo-scientific research initiative Inkaba yeAfrica a series of magnetotelluric field experiments were conducted along the Agulhas-Karoo Transect in South Africa which aims to understand the geodynamic processes along

Africa's southern continental margin. Along the MT profile across the Cape Fold Belt we can identify areas (> 10 km) where MT sites exhibit phases over $90°$. Due to the dense site spacing we are able to observe this behaviour consistently at several sites. In order to satisfy the standard inversion procedure a considerable amount of data, especially those with phases greater than $90°$, are excluded from the 2D isotropic inversion. The results obtained by isotropic 2D inversion is adequate to explain most parts along the profile but it is very unsatisfactory not being able to include phases greater than $90°$ and thus neglect a substantial amount of data. Furthermore, according to known geological and tectonic information we believe that the phases greater than $90°$ are caused by some electrically anisotropic structures in the survey area.

All of this motivates me to accomplish this thesis. The objectives of this thesis are threefold: 1) develop two-dimensional anisotropic inversion procedure for magnetotelluric data. 2) carry out detailed synthetic tests to demonstrate the capabilities and show the limitations of the implemented inversion strategy. 3) study the electrical properties of the Cape Fold Belt using magnetotelluric measurements.

This thesis is organized into four parts. The first part, chapter 2, introduces briefly the theoretical background of the magnetotelluric method and the properties of electrical anisotropy. At the end of this part, the general concepts of magnetotelluric induction is derived into cases of different dimensionality, e.g. one-, two- and three-dimensional cases. Comparisons are made between electrical isotropy and anisotropy for each case. The second part of the thesis, chapter 3, details algorithms for solving the anisotropic forward modeling problem in one- and two-dimensional structure. Comparisons are also made between isotropic and anisotropic case. Synthetic 2D model studies are presented at the end of this part in order to show the different between isotropic and anisotropic modeling and to demonstrate the necessary conditions for inducing anomalous phases in a 2D model containing anisotropic structures. The third part of the thesis, chapter 4, details the solution of the 2D MT anisotropic inversion problem. It begins with a general overview of the inversion methodology through which the concept of 2D anisotropic inversion is derived. Synthetic inversion studies are presented at the end of this part in order to demonstrate the capabilities and show the limitations of the implemented inversion procedure. The fourth part of the thesis, chapter 5, is a magnetotelluric study of the Cape Fold Belt. The forward modeling algorithm introduced in the second part and the inversion algorithm introduced in the third part are used to explain these data. The results as well as the implications are presented. Conclusions and suggestions for further work are presented in chapter 6.

Chapter 2.

Basic concepts of magnetotelluric (MT) induction

This chapter outlines the basic concepts of the MT method and describes the main formulations of the induction problem. I will start with a theoretical introduction of electromagnetic induction and show how it is related to the properties of Earth.

2.1. From Maxwell's equations to electromagnetic induction in the earth

The behaviour of electromagnetic (EM) fields is described by Maxwell's equations, which relate the time varying electric and magnetic fields. The first two Maxwell equations in their differential form are:

$$\nabla \times \mathbf{E} = -\frac{\partial \mathbf{B}}{\partial t} \tag{2.1}$$

$$\nabla \times \mathbf{H} = \frac{\partial \mathbf{D}}{\partial t} + \mathbf{J} \tag{2.2}$$

Here, $\mathbf{E}$ is the electric field ($\mathrm{V/m}$), $\mathbf{B}$ is the magnetic flux density ($\mathrm{Vs/m^2}$), $\mathbf{H}$ is the magnetic field ($\mathrm{A/m}$), $\mathbf{D}$ is the electric displacement current ($\mathrm{C/m^2}$), and $\mathbf{J}$ is the current density ($\mathrm{A/m^2}$).

Equation (2.1) is the Faraday's law and describes how a time varying magnetic field excites an electric field. The Ampere's law including Maxwell's correction in equation (2.2) states that

magnetic fields can be generated in two ways: by electrical current (the original Ampere's law) and by time varying electric fields (Maxwell's correction).

Two more Maxwell's equations can be derived from equations (2.1) and (2.2) by applying the divergence operator ($\nabla\cdot$) and making use of the vector identity $\nabla \cdot \nabla \times \mathbf{A} = 0$ ($\mathbf{A}$ represents an arbitrary vector field).

Taking the divergence of equation (2.1) yields:

$$\begin{aligned} \nabla \cdot \nabla \times \mathbf{E} = -\nabla \cdot \frac{\partial \mathbf{B}}{\partial t} = -\frac{\partial}{\partial t}(\nabla \cdot \mathbf{B}) = 0 \\ \Longrightarrow \nabla \cdot \mathbf{B} = 0 \end{aligned} \tag{2.3}$$

Equation (2.3) is the Gauss's law for magnetism and states that magnetic monopoles do not exist. Similarly, taking the divergence of equation (2.2) earn:

$$\begin{aligned} \nabla \cdot \nabla \times \mathbf{H} = \frac{\partial}{\partial t}(\nabla \cdot \mathbf{D}) + \nabla \cdot \mathbf{J} = 0 \\ \Longrightarrow \nabla \cdot \mathbf{J} = -\frac{\partial}{\partial t}(\nabla \cdot \mathbf{D}) \end{aligned} \tag{2.4}$$

Using the continuity equation $\nabla \cdot \mathbf{J} = -\frac{\partial q}{\partial t}$ (q is the charge density ($\mathrm{C/m^3}$)), which shows that the divergence of the current density is equivalent to the rate of accumulation of charge density , in equation (2.4) yields:

$$\nabla \cdot \mathbf{J} = -\frac{\partial q}{\partial t} = -\frac{\partial}{\partial t}(\nabla \cdot \mathbf{D}) \tag{2.5}$$

and thus,

$$\nabla \cdot \mathbf{D} = q \tag{2.6}$$

Equation (2.6) is the Gauss's law for electricity and shows that the electric field is the result of the distribution of electric charge.

Homogeneous earth materials mostly exhibit conductivities of $10^{-4}\ \mathrm{S/m}$ or greater, so that free charges q_e dissipate in less than $10^{-6}\ \mathrm{s}$. Thus, with frequencies employed in deep geophysical sounding usually smaller than $10^5\ \mathrm{Hz}$, it holds $\partial q_e/\partial t \sim 0$, together with equation (2.5) we easily obtain:

$$\nabla \cdot \mathbf{J} = 0 \tag{2.7}$$

However, equation (2.7) does not apply to inhomogeneous regions; at the interface between two different media a surface charge may accumulate and thus $\partial q_e/\partial t \sim 0$ becomes invalid. ((Ward and Hohmann, 1987)).

Equations (2.1), (2.2), (2.3) and (2.6) are uncoupled differential equations and represent the fundamental equations in electromagnetism.

Under necessary assumptions (see Appendix A.1) the Maxwell's equations can be rewritten as:

$$\nabla \times \mathbf{E} = -\frac{\partial \mathbf{B}}{\partial t} \tag{2.8}$$

$$\nabla \times \mathbf{H} = \sigma \mathbf{E} \tag{2.9}$$

$$\nabla \cdot \mathbf{B} = 0 \tag{2.10}$$

$$\nabla \cdot \mathbf{E} = \frac{q}{\varepsilon_0} \tag{2.11}$$

where σ denotes the electrical conductivity in $(\mathrm{S/m})$ and $\varepsilon_0 = 8.85 \cdot 10^{-12}\ \mathrm{As/Vm}$ is a universal constant called the dielectric permittivity of free space.

These equations represent the basic equations of electromagnetic induction in a source-free medium. The fields that satisfy them are time-dependent, but they change sufficiently slow and behave like static fields. Therefore, these fields are called quasi-static fields.

These equations can be transformed from the time domain into the frequency domain, and the solution can be simplified by replacing time derivatives with simple multiplications, i.e.,

$$-\frac{\partial \mathbf{B(t)}}{\partial t} \xrightarrow{\mathcal{F}} -i\omega \mathbf{B}(\omega) \tag{2.12}$$

for a field at frequency ω.

We can use the fact that $\nabla \cdot (\nabla \times \mathbf{A}) = 0$ holds for any vector field $\mathbf{A}$. Applying the divergence $(\nabla\cdot)$ to equation (2.9) yields

$$\nabla \cdot (\sigma \mathbf{E}) = \sigma \nabla \cdot \mathbf{E} + \mathbf{E} \nabla \sigma = 0 \tag{2.13}$$

From equation (2.11) follows that

$$\frac{q}{\varepsilon_0} = -\mathbf{E}\frac{\nabla \sigma}{\sigma} \Rightarrow \frac{q}{\varepsilon_0} = -\mathbf{E} \nabla \ln \sigma \tag{2.14}$$

This results in modified Maxwell's equations:

$$\begin{aligned} \nabla \times \mathbf{E} &= -i\omega\mu_0\mathbf{H} && (2.15)\\ \nabla \times \mathbf{H} &= \sigma\mathbf{E} && (2.16)\\ \nabla \cdot \mathbf{H} &= 0 && (2.17)\\ \nabla \cdot \mathbf{E} &= -\mathbf{E}\nabla \ln\sigma && (2.18) \end{aligned}$$

where $\mu_0 = 4\pi \cdot 10^{-7}\ \mathrm{Vs/Am}$ is also a universal constant called the magnetic permeability of free space.

These four equations can be combined into two equations by taking the curl ($\nabla\times$) of equations (2.15) and (2.16) with concerning of the vector Laplacian operator:

$$\nabla^2 := \nabla(\nabla\cdot) - \nabla \times (\nabla\times) \tag{2.19}$$

For quasi-static fields the corresponding differential equation satisfied by $\mathbf{E}$ is given by taking the curl of equations (2.15) and substituting $\nabla \times \mathbf{H}$ from equation (2.16) and $\nabla \cdot \mathbf{E}$ from equation (2.18)

$$\begin{aligned} \nabla \times \nabla \times \mathbf{E} &= \nabla(\nabla \cdot \mathbf{E}) - \nabla^2\mathbf{E} = -i\omega\mu_0\nabla \times \mathbf{H}\\ \Rightarrow \nabla^2\mathbf{E} &= i\omega\mu_0\sigma\mathbf{E} - \nabla(\mathbf{E}\nabla \ln\sigma) && (2.20) \end{aligned}$$

Similarly, the corresponding differential equation satisfied by $\mathbf{H}$ can be derived by taking the curl of equation (2.16) and substituting $\nabla \times \mathbf{E}$ from equation (2.15) with concerning the fact that $\nabla \times (\alpha\mathbf{A}) := \alpha\nabla \times \mathbf{A} - \mathbf{A} \times \nabla\alpha$ holds for any vector field $\mathbf{A}$ and scalar field α

$$\begin{aligned} \nabla \times \nabla \times \mathbf{H} &= \nabla(\nabla \cdot \mathbf{H}) - \nabla^2\mathbf{H} = \sigma\nabla \times \mathbf{E} - \mathbf{E} \times \nabla\sigma\\ \Rightarrow \nabla^2\mathbf{H} &= i\omega\mu_0\sigma\mathbf{H} + \mathbf{E} \times \nabla\sigma && (2.21) \end{aligned}$$

Equations (2.20) and (2.21) describe the magnetic and electric fields under the above assumptions in their most general form.

The orthogonal components of the horizontal electric and magnetic fields are related through a quantity called impedance tensor $\underline{\underline{\mathbf{Z}}}$:

$$\mathbf{E}(\omega) = \underline{\underline{\mathbf{Z}}}(\omega) \cdot \mathbf{H}(\omega) \tag{2.22}$$

or in a tensor form as:

$$\begin{pmatrix} E_x \\ E_y \end{pmatrix} = \begin{pmatrix} Z_{xx} & Z_{xy} \\ Z_{yx} & Z_{yy} \end{pmatrix} \cdot \begin{pmatrix} H_x \\ H_y \end{pmatrix} \tag{2.23}$$

The complex-valued impedance tensor $\underline{\underline{Z}}$ in equation (2.22) can be converted into a apparent resistivity ρ_a and a phase ϕ , namely:

$$\rho_{a,ij(\omega)} = \frac{1}{\mu_0 \omega} |Z_{ij}(\omega)|^2 \tag{2.24}$$

$$\phi_{ij} = tan^{-1}\left(\frac{Im\{Z_{ij}\}}{Re\{Z_{ij}\}}\right) \tag{2.25}$$

Another linear relationship of the electromagnetic fields is the relation between the vertical magnetic component H_z and the horizontal magnetic field components H_x,H_y, which is written as:

$$H_z = T_{zx}H_x + T_{zy}H_y \tag{2.26}$$

where T_{zx} and T_{zy} constitute the vertical magnetic transfer functions. They describe to which extent the horizontal magnetic components are tipped into the vertical components. T_{zx} and T_{zy} are sometimes called "tipper" (Vozoff, 1972). An important quantity derived from the vertical magnetic transfer functions is the induction vector: Using Wiese-Convention (Wiese, 1962) the amplitude and the angle of the real part of the induction vector are computed as:

$$amplitude\ of\ T_{real} = \sqrt{Re\{T_{zx}\}^2 + Re\{T_{zy}\}^2} \tag{2.27}$$

$$angle\ of\ T_{real} = tan^{-1}\left(\frac{Re\{T_{zy}\}}{Re\{T_{zx}\}}\right) \tag{2.28}$$

The amplitude and the angle of the imaginary part of the induction vector can be computed accordingly. In Wiese-convention the induction vectors tend to point away from the elongated conductors. Induction vectors are usually used to identify lateral contrasts of the conductivity in the subsurface.

2.2. Electrical anisotropy

Assume that all media are linear, homogeneous, and possess electrical properties which are independent of time, temperature, or pressure. Under these assumptions the current density $\mathbf{J}$ and the electric field $\mathbf{E}$ are linearly related through Ohm's Law, by the electrical conductivity σ (eq. A.7).

2.2.1. Electrical conductivity tensor

In homogeneous, isotropic media where current density is independent of the direction of the electric field, the electrical conductivity is a scalar value. The amount of current flow is then governed solely by the magnitudes of σ and $\mathbf{E}$, and the direction of the flow is always parallel to $\mathbf{E}$. However, in many cases, currents are allowed to flow more easily in one direction than another, e.g., consider geological formations with distinct layers of sedimentary material, electrical conductivity in direction parallel to the layers is different from that in direction perpendicular to the layers. On this scale, therefore, exists some structural anisotropy, also called as macroscopic anisotropy. It is distinguished from the intrinsic anisotropy or microscopic anisotropy, which is caused by ordered inhomogeneities and exists already on a very small scale (see Weidelt, 1999).

The anisotropy of electrical conductivity is essentially a scale effect: Even if the conductivity is isotropic on the microscale, it will become anisotropic on a larger scale if, in the averaging, preferred orientations (e.g., layering or lamination) exist. An example is given in Fig. 2.1:

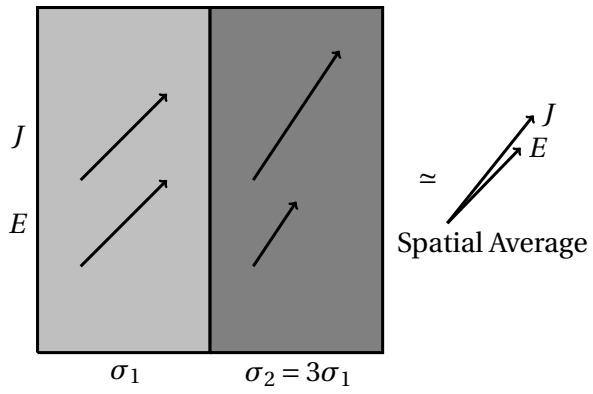

Figure 2.1.: A simple example for the origin of structural anisotropy from a spatial average of $\mathbf{E}$ (electric field) and $\mathbf{J}$ (current density) over isotropic conductors with different conductivities ($\sigma_2 = 3 \times \sigma_1$). The averaged current density is deflected toward the preferential direction of the electric field. Figure redrawn from Weidelt (1999).

In both isotropic lamina, electric field $\mathbf{E}$ and current density $\mathbf{J}$ are parallel, and the tangential electric field and the current density normal to the interface are continuous at the surface. After spatial averaging over both lamina, however, $\mathbf{E}$ and $\mathbf{J}$ are no longer aligned.

With electrical anisotropy, current density depends on the direction of the electric field, the electrical conductivity is considered to be a tensor (e.g., Pek and Verner, 1997, Weidelt, 1999, and many others). Equation (A.7) can be rewritten as:

$$\mathbf{J} = \underline{\underline{\sigma}}\mathbf{E} \tag{2.29}$$

where $\underline{\underline{\sigma}}$ is a tensor of rank 3. In right-handed Cartesian coordinates (x, y, z) with z positive downward, $\underline{\underline{\sigma}}$ has the representation

$$\underline{\underline{\sigma}} = \begin{pmatrix} \sigma_{xx} & \sigma_{xy} & \sigma_{xz} \\ \sigma_{yx} & \sigma_{yy} & \sigma_{yz} \\ \sigma_{zx} & \sigma_{zy} & \sigma_{zz} \end{pmatrix} \tag{2.30}$$

Equation (2.29) represents the general form of Ohm's Law. With 9 components of σ_{ij} $(i, j = x, y, z)$ the electrical conductivity of an anisotropic medium can be fully described.

The conductivity tensor $\underline{\underline{\sigma}}$ has the following properties:

1. Symmetry: The conductivity tensor is symmetric for purely ohmic conduction (Onsager, 1931).

2. Non-negativity: The conductivity tensor has to be positive semidefinite because the time-averaged specific energy dissipation, $(\frac{1}{2}\mathbf{E}^* \cdot \mathbf{J} = \frac{1}{2}\mathbf{E}^* \cdot \underline{\underline{\sigma}} \cdot \mathbf{E})$, is non-negative. $\mathbf{E}^*$ denotes complex conjugation.

In the air (half-space $z < 0$) all tensor elements vanish; in the conductor $z > 0$ the tensor is assumed to be positive definite. Necessary and sufficient conditions for this property are the positivity of the three major determinants. Interpretation of the off-diagonal elements of $\underline{\underline{\sigma}}$ is obvious: They describe current flow perpendicular to the direction of applied electric field. For instance, the element σ_{xy} describes current flow in the x-direction due to an applied electric field in the y-direction and it can denote a deviation of the direction of regional strike from the horizontal axes of anisotropy; Elements σ_{xz} and σ_{yz} describe current flow in the x-direction and y-direction, respectively, due to a common electric field applied in the z-direction and denote dipping anisotropy.

Fig. 2.2 shows two examples of electrical anisotropy, the azimuthal anisotropy and the dipping anisotropy. Let σ_{min} equals σ_1 and σ_{max} equals σ_2, the bulk conductivity of the alternating conductive dykes can be defied as

$$\underline{\underline{\sigma}} = \begin{pmatrix} \sigma_1 \cos^2\alpha + \sigma_2 \sin^2\alpha & (\sigma_2 - \sigma_1)\sin\alpha\cos\alpha & 0 \\ (\sigma_2 - \sigma_1)\sin\alpha\cos\alpha & \sigma_1 \sin^2\alpha + \sigma_2 \cos^2\alpha & 0 \\ 0 & 0 & \sigma_1 \end{pmatrix} \tag{2.31}$$

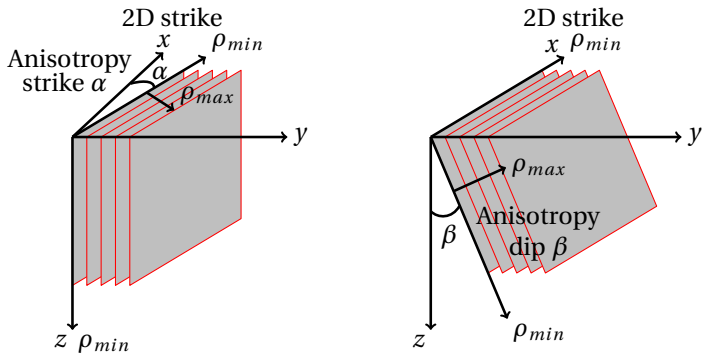

Figure 2.2.: Example representations of anisotropy in earth materials, simulated by conductive dykes with principal conductivities σ_{min} and σ_{max}. Left: azimuthal anisotropy with anisotropy strike α with respect to the 2-D structural strike. Right: dipping anisotropy. Figure modified from Heise and Pous (2001).

for azimuthal anisotropy, and

$$\underline{\underline{\sigma}} = \begin{pmatrix} \sigma_1 & 0 & 0 \\ 0 & \sigma_2 \cos^2\beta + \sigma_1 \sin^2\beta & (\sigma_1 - \sigma_2)\sin\beta\cos\beta \\ 0 & (\sigma_1 - \sigma_2)\sin\beta\cos\beta & \sigma_2 \sin^2\beta + \sigma_1 \cos^2\beta \end{pmatrix} \tag{2.32}$$

for dipping anisotropy, respectively. Outside of the dykes, the conductivity may be isotropic.

2.2.2. Euler angles

In previous section we have discussed that for a medium with electrical anisotropy, the conductivity has to be considered as a tensor, and this tensor is symmetric and positive semidefinite. From mathematical point of view a real symmetric matrix is diagonalizable by orthogonal matrices. In other words it is always possible to find a set of new coordinates (the principal axes) in which the tensor is diagonal with it's principal values

$$\underline{\underline{\sigma}}' = \begin{pmatrix} \sigma_x & 0 & 0 \\ 0 & \sigma_y & 0 \\ 0 & 0 & \sigma_z \end{pmatrix} \tag{2.33}$$

In equation (2.33) the tensor elements σ_x, σ_y and σ_z are the conductivities along the corresponding principal axes. Since the original conductivity tensor is positive semidefinite, the

principal values must be all positive. This procedure is called principal axis transformation in mathematics and it can be expressed as

$$\underline{\underline{\sigma}}' = A^{-1}\underline{\underline{\sigma}}A = A^{T}\underline{\underline{\sigma}}A \tag{2.34}$$

where $\underline{\underline{\sigma}}$ is the original conductivity tensor with it's diagonalized form $\underline{\underline{\sigma}}'$, A is an orthogonal matrix and builds the new coordinates for $\underline{\underline{\sigma}}'$, A^{-1} and A^{T} represent the inverse and transpose of A. The principal axes and principal values can be obtained by finding eigenvalues and eigenvectors of $\underline{\underline{\sigma}}$.

The orthogonal matrix A can be decomposed into three elementary Euler's spatial rotations, denoted by Euler angles α, β and γ. In other words $A = R(\alpha)R(\beta)R(\gamma)$, where $R(\alpha)$ represents the rotation matrix with respect to angle α. The euler angles can be defined as follows: First rotate an angle α about the z-axis (this causes x- and y axes move to new orientations while z remains unchanged). Then rotate an angle β about its new x-axis (it causes y and z axes move to new orientations while x-axis remains unchanged). Finally, rotate an angle γ about its new z-axis. This is so called $z - x' - z''$ convention of Euler angles. Different authors may use different sets of angles to describe these orientations, or different names for the same angles, leading to different conventions. Unless otherwise stated, the $z - x' - z''$ convention of Euler angles will be used throughout the entire thesis.

Equation (2.34) can be then rewritten as

$$\underline{\underline{\sigma}}' = R_z^T(\gamma)R_x^T(\beta)R_z^T(\alpha)\underline{\underline{\sigma}}R_z(\alpha)R_x(\beta)R_z(\gamma) \tag{2.35}$$

and dually with three principal values and three rotation angles the original conductivity tensor $\underline{\underline{\sigma}}$ is unique defined

$$\underline{\underline{\sigma}} = R_z(\alpha)R_x(\beta)R_z(\gamma)\underline{\underline{\sigma}}'R_z^T(\gamma)R_x^T(\beta)R_z^T(\alpha) \tag{2.36}$$

The elementary Euler's rotations are demonstrated in Fig. 2.3 and the corresponding rotation matrices are

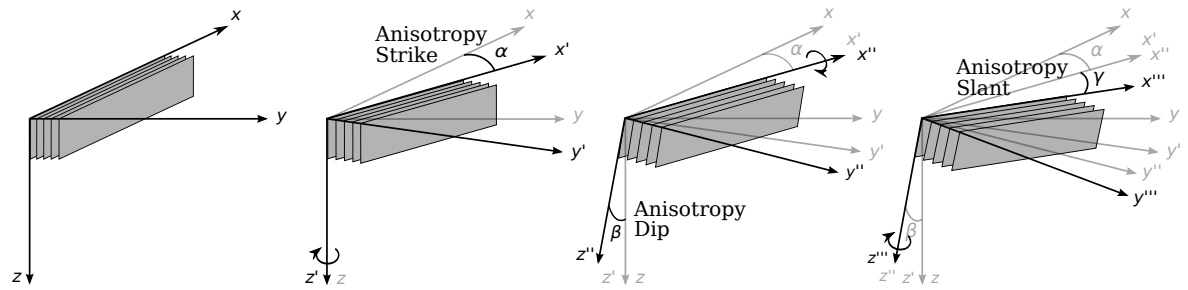

Figure 2.3.: Illustration of the $z - x' - z''$ convention of Euler's rotations: transformation of conductive dykes into general position by successively rotating three Euler angles α, β and γ about the z-, x'- and z''-axis, respectively.

$$
\begin{aligned}
R_z(\alpha) &= \begin{pmatrix} \cos\alpha & -\sin\alpha & 0 \\ \sin\alpha & \cos\alpha & 0 \\ 0 & 0 & 1 \end{pmatrix} \\
R_x(\beta) &= \begin{pmatrix} 1 & 0 & 0 \\ 0 & \cos\beta & -\sin\beta \\ 0 & \sin\beta & \cos\beta \end{pmatrix} \\
R_z(\gamma) &= \begin{pmatrix} \cos\gamma & -\sin\gamma & 0 \\ \sin\gamma & \cos\gamma & 0 \\ 0 & 0 & 1 \end{pmatrix}
\end{aligned}
\tag{2.37}
$$

The Euler's rotations transfer the conductivity tensor into it's diagonal form and vice versa. There is an intuitive reason why do we need the Euler's rotations and introduce it here. All electrical and electromagnetic methods aims to map the electric properties of the subsurface from surface measurements. Of course the electric property of a target can be fully described by using a tensor but it is difficult to image how a tensor looks like spatially. With help of the Euler's rotations an arbitrary anisotropy conductivity can be specified by three coordinate invariants (the principle values) and three angles. The invariants describe the bulk resistivity of the target and the angles, which depend on the particular representation and coordinate system chosen, depict the spatial orientation of the target in a predefined coordinate system. Although it is more difficult to decompose the rotation matrix to Euler angles and the solution is not necessarily unique, the combination of invariants and angles provides an easy way to understand the anisotropic properties of Earth's material.

Chapter 3.

MT forward problem

The MT forward modeling aims to solve the Maxwell's equations and simulate the spatial and temporal distribution of electric and magnetic fields in the subsurface for a given conductivity distribution and a range of periods (or frequencies). In this chapter I will focus on general anisotropic Earth model in two-dimensional cases. Beside detailed description of forward algorithm a model study is curried out and the difference between anisotropic and isotropic MT forward modeling will be discussed throughout the entire chapter. For completeness, the forward problem in one-dimensional for generally anisotropic Earth model is also discussed, the interested reader is referred to appendix A.3.

3.1. Two-dimensional (2D) structure with anisotropic conductivities

The effect of anisotropy in 2D structures was initially studied by Reddy and Rankin (1975), who considered just the effect of horizontal anisotropy. More recently, Osella and Martinelli (1993) calculated the magnetotelluric response of models with smooth irregular boundaries and with a special orientation of principal axes. Schmucker (1994) presented an algorithm for the computation of the electromagnetic induction in a non-uniform thin sheet above a layered half-space, which may contain one or more layers of anisotropic conductivity. General anisotropic structures in 2D are investigated by Pek and Verner (1997) and Li (2002), with arbitrary orientation of the principal axes.

Unlike the 1D forward problem, which can be solved analytically, the 2D forward problem is more complicated and only a few isotropic 2D models are analytically solvable. Hence, in

practice, the MT 2D forward problem is solved numerically for both isotropic and anisotropic cases. The solution of the governing second order partial differential equations is obtained by applying one of the following discretization methods, namely the Finite difference Method (FDM), the Finite Volume Method (FVM) or the Finite Element Method (FEM).

The FEM involves assumed functional forms for the model and fields in small regions of specified geometry. The fields are then matched where the elements abut. FEM is generally thought to be more flexible in terms of model design since the model cells are typically triangular shaped. It is particularly useful if the earth model includes topography or bathymetry. The FDM based upon the differential form of the partial differential equations to be solved. Each derivative is replaced with an approximate difference formula. The computational domain is usually divided into rectangular cells and the solution will be obtained at each nodal point. The FDM becomes difficult to use when the coefficients involved in the equation are discontinuous (e.g. in the case of heterogeneous media). In contrast, the FVM based upon an integral form of the partial differential equation to be solved (e.g. conservation of mass or energy). The partial differential equation is written in a form which can be solved for a given finite volume (e.g. the control volume or cell). The computational domain is discretized into finite volumes and then for every volume the governing equations are solved. The resulting system of equations usually involves fluxes of the conserved variable, and thus the calculation of fluxes is very important in FVM. The basic advantage of this method over FDM is that the discontinuities of the coefficients will not be any problem if the mesh is chosen such that the discontinuities of the coefficients occur on the boundaries of the control volumes. Note that the finite volume scheme is often called "finite difference scheme" or "cell centered difference scheme". Indeed, in the finite volume method, the finite difference approach can be used for the approximation of the fluxes on the boundary of the control volumes. Thus, the finite volume scheme differs from the finite difference scheme in that the finite difference approximation is used for the flux rather than for the operator itself. In this paragraph I will discuss the MT 2D anisotropic forward problem in details based on the finite volume method and the early work of Pek and Verner (1997) and Li (2002).

I adopted the induction equations for 2D structures with arbitrary anisotropy derived in appendix A.2 (equations A.42 and A.43).

$$\frac{\partial^2 E_x}{\partial y^2} + \frac{\partial^2 E_x}{\partial z^2} + i\omega\mu_0(WE_x + A\frac{\partial H_x}{\partial y} - B\frac{\partial H_x}{\partial z}) = 0 \quad (3.1)$$

$$\frac{\partial}{\partial y}\left(\frac{\sigma_{yy}}{D}\frac{\partial H_x}{\partial y}\right) + \frac{\partial}{\partial z}\left(\frac{\sigma_{zz}}{D}\frac{\partial H_x}{\partial z}\right) + \frac{\partial}{\partial y}\left(\frac{\sigma_{yz}}{D}\frac{\partial H_x}{\partial z}\right) + \cdots$$
$$+\frac{\partial}{\partial z}\left(\frac{\sigma_{yz}}{D}\frac{\partial H_x}{\partial y}\right) + i\omega\mu_0 H_x - \frac{\partial\left(AE_x\right)}{\partial y} + \frac{\partial\left(BE_x\right)}{\partial z} = 0 \quad (3.2)$$

where

$$D = \sigma_{zz}\sigma_{yy} - \sigma_{yz}\sigma_{zy}, \qquad A = (\sigma_{yx}\sigma_{zy} - \sigma_{yy}\sigma_{zx})/D$$
$$B = (\sigma_{zx}\sigma_{yz} - \sigma_{zz}\sigma_{yx})/D, \quad W = \sigma_{xx} + \sigma_{xy}B + \sigma_{xz}A$$

and σ_{ij} represents element of the conductivity tensor $\underline{\underline{\sigma}}$. Again, equations (3.1) and (3.2) express a coupled system. The pure TE- and TM-mode which can be usually obtained for isotropic case do not exist any more. The both equations have to be solved simultaneously. From now on I will call equation (3.1) the quasi E-polarisation equation and equation (3.2) the quasi H-polarization equation.

Within MT two-dimensional (2D) forward problem I am considering induction problems, where both the conductivity structure and inducing field are independent of one horizontal coordinate, say x. First of all, I define a domain V of 2D anomalous structure with boundaries Γ_l, Γ_r, Γ_t and Γ_b at the left, right, top and bottom sides of V, respectively. A cartesian coordinate system with z-axis positive downwards, x-axis to the north and y-axis to the east is used. The domain consists of two parts. The uppermost part is an air layer and which is a perfect insulator. The lower part of the model represents the solid earth with conductivity σ_2 which could also be electrical anisotropy, a conductive block with arbitrary anisotropic conductivity $\underline{\underline{\underline{\sigma_3}}}$ is embedded into the lower part of the model (Fig. 3.1,left panel).

3.1.1. Boundary conditions

Within geo-electromagnetic induction we consider fields which change sufficiently slow, so that their variation in time is negligible compare to the duration of observation. In other words, we are more interested in their spatial distribution rather than their variation in time. Hence, this kind of forward problem belongs to the so called "boundary value problem", if the mathematical nomenclature is used.

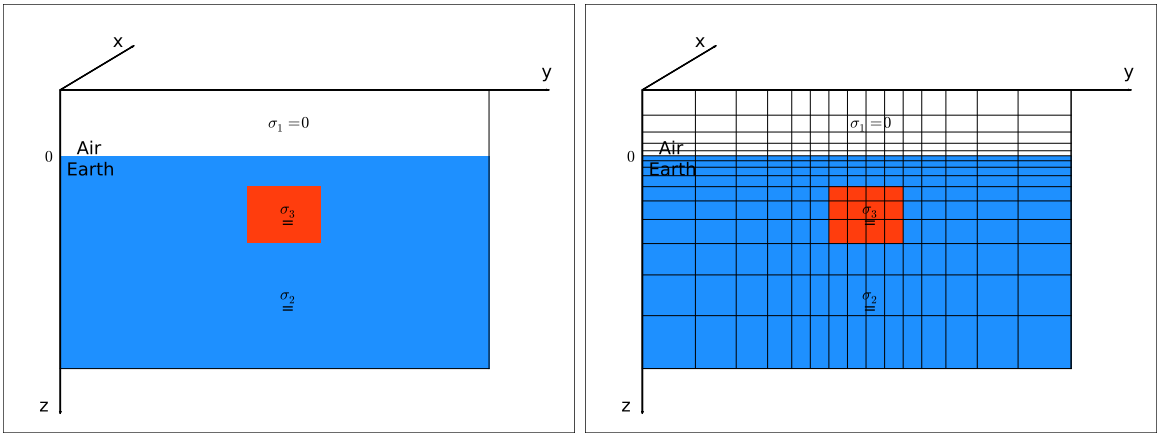

Figure 3.1.: A simple example illustrates two-dimensional anisotropic structure. The model consists of two parts which represent the air layer and the solid earth, respectively. A conductive block is embedded into the lower part of the model (left panel). A possible numerical descritization of the model domain is given at the right panel.

To complete the mathematical formulation of the problem we must supply the boundary conditions for the field components both on the inner and outer boundaries. On the outer boundaries of the model the Dirichlet boundary condition can be used. The values can be constructed from the 1D solutions for the corresponding layered structure at the left and right border of the model. The 1D forward algorithm discussed in appendix A.3 can be used for calculating the left- and right-hand boundary values. At the top and the bottom of the model the boundary values can be obtained by linear interpolation of the respective 1D values at the left- and right-hand margins of the model (Pek and Verner, 1997).

On inner boundaries, where blocks with different electrical properties make contact (include the Air/Earth interface where $z = 0$), the following rules must be hold according to the general continuity conditions:

1. The tangential components of the electric field E are continuous,
2. The normal component of current density $\mathbf{J}$ must be continuous across conductivity discontinuities and zero across $z = 0$,
3. All components (normal and tangential) of the magnetic field $\mathbf{H}$ are continuous since the vacuum magnetic permeability is assumed throughout the entire domain.

4. The first derivatives of the normal component of the electric field $\mathbf{E}$ and the magnetic field $\mathbf{H}$ are continuous.

3.1.2. Numerical approximation

To approximate the governing equations (3.1 and 3.2) numerically, the domain is projected onto a numerical grid and, within a finite grid region, subdivided into a system of electrically homogeneous, but in general anisotropic, rectangular grid cells (Fig. 3.1, right panel). The grid is in general irregular and it should both fit the geometry of the model under study and meet general rules accepted for designing numerical grids in induction modeling studies. The domain is discretized as $j = 0, 1, \cdots, m$ lines in Y direction and $k = 0, 1, \cdots, n$ lines in Z direction. Thus, the lines 0 and m in the horizontal direction correspond to the left and right boundaries Γ_l and Γ_r, lines 0 and n in the vertical direction correspond to the top and bottom boundaries Γ_t and Γ_b, respectively. The conductivity of each cell in the domain V is denoted as σ_{jk}. The solutions of equations (3.1 and 3.2) for E_x and H_x must be found at each node in the entire domain for a given conductivity distribution. At the same time the internal and external boundary conditions must be satisfied.

Let us consider a typical nodal point (j, k) located in the inner part of a rectangular, but not necessarily uniform, grid (Fig. 3.2). Its neighboring nodes are $(j, k+1); (j, k-1); (j-1, k)$ and $(j+1, k)$ which are located to the right, left, down and up from j, k respectively.

The traditional way of the finite volume method would be integrating equation (3.1) and (3.2) over the rectangular area around j, k, namely $G_{j,k}$ in Fig. (3.2), for all inner nodes of the model. This procedure is straightforward but quite tedious. A better way to achieve this is using immediately the equivalent integral form of Maxwell's equations, specified for the integration cell $A_{j,k}$. The Maxwell's equations for 2D anisotropic media are already derived in section 2.4 (eqs. A.29 to A.34). I repeat these equations only for completeness.

$$\frac{\partial E_z}{\partial y} - \frac{\partial E_y}{\partial z} = -i\omega\mu_0 H_x \tag{3.3}$$

$$\frac{\partial E_x}{\partial z} = -i\omega\mu_0 H_y \tag{3.4}$$

$$\frac{\partial E_x}{\partial y} = i\omega\mu_0 H_z \tag{3.5}$$

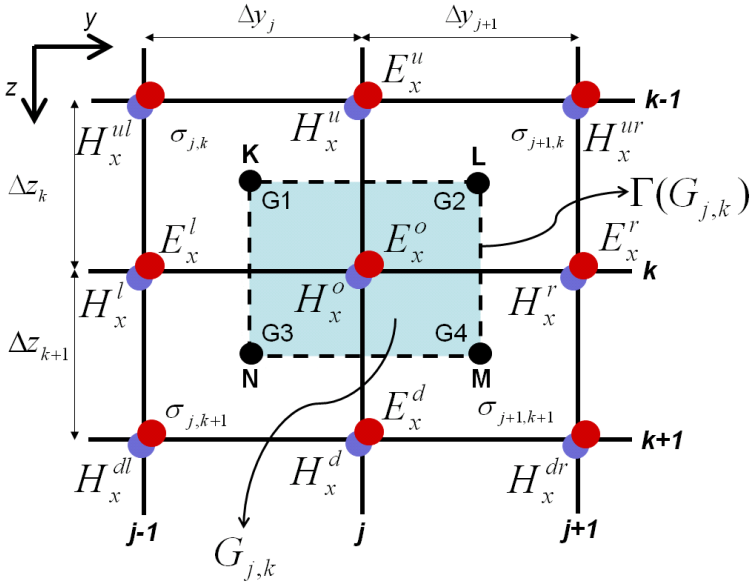

Figure 3.2.: A nine points stencil scheme used in approximating the quasi E-polarization equation (3.1) and the quasi H-polarization equation (3.2). For the quasi E-polarization equation only a five points stencil is required and in total 10 field values (5 electric and 5 magnetic) are used. In contrast, a nine points stencil is needed for the quasi H-polarization equation and in total 14 field values (5 electric and 9 magnetic) are required.

$$\frac{\partial H_z}{\partial y} - \frac{\partial H_y}{\partial z} = \sigma_{xx}E_x + \sigma_{xy}E_y + \sigma_{xz}E_z \tag{3.6}$$

$$\frac{\partial H_x}{\partial z} = \sigma_{yx}E_x + \sigma_{yy}E_y + \sigma_{yz}E_z \tag{3.7}$$

$$-\frac{\partial H_x}{\partial y} = \sigma_{zx}E_x + \sigma_{zy}E_y + \sigma_{zz}E_z \tag{3.8}$$

The corresponding integral form of the quasi E-polarization equation (3.1) is the Ampere's Law.

$$\oint_{\Gamma(G_{j,k})} \mathbf{H} \cdot dl = \int_{G_{j,k}} \underline{\sigma}\mathbf{E} \cdot dg \tag{3.9}$$

where $\Gamma(G_{j,k})$ represents the oriented boundary of the integration cell $G_{j,k}$ and dl is the element of the integration path along this boundary. dg is an areal element of the integration

area $G_{j,k}$ and $\underline{\underline{\sigma}}\mathbf{E}$ denotes the total current density along x-axis direction.

With consideration of (3.4) and (3.5), equation (3.9) can be rewritten as

$$\left(\frac{\partial E_x}{\partial z}\right)_{KL}\overline{KL} - \left(\frac{\partial E_x}{\partial y}\right)_{LM}\overline{LM} + \left(\frac{\partial E_x}{\partial z}\right)_{MN}\overline{MN} - \\ - \left(\frac{\partial E_x}{\partial y}\right)_{NK}\overline{NK} - i\omega\mu_0 S\left(G_{j,k}\right)\left(J_x\right)_{G_{j,k}} = 0 \tag{3.10}$$

where $\left(\nu\right)_{\gamma}$ represents the mean value of the function $\nu(y,z)$ across γ, which denotes a section of the boundary of the integration cell. $\overline{P_1P_2}$ is the distance between the corresponding vertices of the integration cell, $S\left(G_{j,k}\right)$ is the area of the integration cell and $\left(J_x\right)_{G_{j,k}}$ is the x-component of the total current density.

From the boundary condition follows that the first derivatives of E_x are continuous everywhere. Consequently, we can approximate derivatives normal to the line of integration in equation (3.10) using central-difference formula. For instance, let us consider the upper edge of integration cell $A_{i,j}$. The gradient of the outward normal from this edge to the top is approximated by:

$$\left(\frac{\partial E_x}{\partial z}\right)_{KL}\overline{KL} \approx \frac{E_x^u - E_x^o}{\Delta z_k}\cdot\frac{\Delta y_j + \Delta y_{j+1}}{2} \tag{3.11}$$

The other three terms can be approximated in the same way. According to (3.1) the total current density J_x can be expressed as

$$J_x = WE_x + A\frac{\partial H_x}{\partial y} + B\frac{\partial H_x}{\partial z} \tag{3.12}$$

where W, A and B are cumulative conductivities introduced in previous section. Hence the last term on the left hand side of equation (3.10) can be approximated through

$$-i\omega\mu_0 S\left(G_{j,k}\right)\left(J_x\right)_{G_{j,k}} \approx -i\omega\mu_0 \iint_{G_{j,k}}\left(WE_x + A\frac{\partial H_x}{\partial y} + B\frac{\partial H_x}{\partial z}\right)dydz \tag{3.13}$$

which implies that the approximation can be done by splitting (3.13) into 3 surface integrals. The first integral can be approximated as

$$-i\omega\mu_0 \iint_{G_{j,k}} (W E_x)\, dydz \approx -i\omega\mu_0 \overline{W}_{j,k} E_x^o \tag{3.14}$$

where

$$\overline{W}_{j,k} = \frac{1}{4}\left(\Delta y_j \Delta z_k W_{j,k} + \Delta y_{j+1}\Delta z_k W_{j+1,k} + \Delta y_j \Delta z_{k+1} W_{j,k+1} + \Delta y_{j+1}\Delta z_{k+1} W_{j+1,k+1}\right)$$

is the total conductance within the integration cell $G_{j,k}$ and $W_{j,k}$ denotes the cumulative conductivity W at the cell (j,k). The electric field component E_x^o represents the mean E_x value on the integration cell $G_{j,k}$. The second integral involves integration of the first derivatives of H_x component with respect to y, the lateral change of H_x, and the cumulative conductivity A is defined on the entire integration cell $G_{j,k}$. Hence, the second integral may again split into 4 simple integrals which integrate over subcells G_1, G_2, G_3 and G_4 (see also Fig. 3.2), respectively. For instance, the integral over subcell G_1 can be formed as

$$\begin{aligned} -i\omega\mu_0 \int_{y_j^-}^{y_j}\int_{z_k^-}^{z_k} A\frac{\partial H_x}{\partial y} dydz &= -i\omega\mu_0 A_{j,k} \int_{z_k^-}^{z_k} \left[H_x(y_j, z) - H_x(y_j^-, z)\right] dz \\ &\approx -\frac{i\omega\mu_0}{4}\Delta z_k A_{j,k}\left(H_x^o - H_x^l\right) \end{aligned} \tag{3.15}$$

where y_j^- denotes the middle point between y_{j-1} and y_j (e.g. $y_j^- = (y_j + y_{j-1})/2$) and z_k^- is the middle point between z_{k-1} and z_k (e.g. $z_k^- = (z_k + z_{k-1})/2$), respectively. $H_x(y_j, z)$ represents the mean value of H_x on the line segment (z_k^-,z_k) at y_j and can be approximated by H_x^o. $H_x(y_j^-, z)$ denotes the mean value of the same field component on the line segment (z_k^-,z_k) but at y_j^- and can be approximated as

$$H_x(y_j^-, z) \approx \frac{1}{2}\left(H_x^o + H_x^l\right)$$

Repeating the same procedure we can approximate the other three integrals over subcells and also the third term of the integrand in equation (3.13). Applying the approximation steps discussed above to all the terms in equation (3.10), an approximate difference equation for the quasi E-polarization at the (j,k)th mesh node can be obtained.

The corresponding integral form of the quasi H-polarization equation (3.2) is the Faraday's Law

$$\oint_{\partial G} \mathbf{E}\, ds = i\omega\mu_0 \int_G \mathbf{H}\, dG \tag{3.16}$$

and which can be rewritten as

$$(E_y)_{KL}\,\overline{KL} + (E_z)_{LM}\,\overline{LM} - (E_y)_{MN}\,\overline{MN} - (E_z)_{NK}\,\overline{NK} - i\omega\mu_0 S\,(G_{jk})\,(H_x)_{G_jk} = 0 \tag{3.17}$$

From (3.7) and (3.8) the field components E_y and E_z can be expressed by means of the basic components E_x and H_x:

$$E_y = \frac{\sigma_{zz}}{D}\frac{\partial H_x}{\partial z} + \frac{\sigma_{yz}}{D}\frac{\partial H_x}{\partial y} + BE_x \tag{3.18}$$

$$E_z = -\frac{\sigma_{yy}}{D}\frac{\partial H_x}{\partial y} - \frac{\sigma_{yz}}{D}\frac{\partial H_x}{\partial z} + AE_x \tag{3.19}$$

Applying (3.18) and (3.19) to equation (3.17), the resulting equation will also only contain the basic field components. For instance, let's consider the first term in (3.17). Replacing E_y with the right hand side of (3.18) implies that this term can be approximated by separating into three individual sub-terms.

$$(E_y)_{KL}\,\overline{KL} = \left(\frac{\sigma_{zz}}{D}\frac{\partial H_x}{\partial z}\right)_{KL}\overline{KL} + \left(\frac{\sigma_{yz}}{D}\frac{\partial H_x}{\partial y}\right)_{KL}\overline{KL} + (BE_x)_{KL}\,\overline{KL} \tag{3.20}$$

The first term on the right hand side of (3.20) is easily approximated by substituting the difference of nodal values for the vertical derivative

$$\left(\frac{\sigma_{zz}}{D}\frac{\partial H_x}{\partial z}\right)_{KL}\overline{KL} \approx \frac{H_x^o - H_x^u}{\Delta z_k}\cdot\left[\frac{\Delta y_j}{2}\left(\frac{\sigma_{zz}}{D}\right)_{j,k} + \frac{\Delta y_{j+1}}{2}\left(\frac{\sigma_{zz}}{D}\right)_{j+1,k}\right] \tag{3.21}$$

and this kind of approximation is already known in the traditional isotropic "H-mode" case.

The second term arises due to dipping anisotropy ($\sigma_{yz} \neq 0$) and can be written as

$$\begin{aligned}\left(\frac{\sigma_{yz}}{D}\frac{\partial H_x}{\partial y}\right)_{KL}\overline{KL} &\approx \frac{H_x(y_j, z_k^-) - H_x(y_j^-, z_k^-)}{\frac{\Delta y_j}{2}}\cdot\frac{\Delta y_j}{2}\left(\frac{\sigma_{yz}}{D}\right)_{j,k} + \\ &\quad \frac{H_x(y_j^+, z_k^-) - H_x(y_j, z_k^-)}{\frac{\Delta y_{j+1}}{2}}\cdot\frac{\Delta y_{j+1}}{2}\left(\frac{\sigma_{yz}}{D}\right)_{j+1,k} \\ &\approx \frac{1}{4}\left(\frac{\sigma_{yz}}{D}\right)_{j,k}\left[H_x^o + H_x^u - H_x^l - H_x^{ul}\right] - \\ &\quad \frac{1}{4}\left(\frac{\sigma_{yz}}{D}\right)_{j+1,k}\left[H_x^o + H_x^u - H_x^r - H_x^{ur}\right]\end{aligned} \tag{3.22}$$

where X^- and X^+ represent the minimal and maximal coordinate of the integration region on the respected axis, in this case X may be either y- or z-axis, and the following approximations are used

$$\begin{aligned} H_x(y_j, z_k^-) &\approx \frac{1}{2}\left[H_x^o + H_x^u\right] \\ H_x(y_j^-, z_k^-) &\approx \frac{1}{4}\left[H_x^o + H_x^u + H_x^l + H_x^{ul}\right] \\ H_x(y_j^+, z_k^-) &\approx \frac{1}{4}\left[H_x^o + H_x^u + H_x^r + H_x^{ur}\right] \end{aligned}$$

The third term on the right hand side of (3.20) is easily approximated by interpolating of nodal values onto cell edges:

$$\left(BE_x\right)_{KL} \overline{KL} \approx \left(B_{j,k} \cdot \frac{\Delta y_j}{2} + B_{j+1,k} \cdot \frac{\Delta y_{j+1}}{2}\right) \cdot \frac{E_x^o + E_x^u}{2} \tag{3.23}$$

Applying the approximation steps discussed above to all the terms in (3.17) and approximating the last term of (3.17) by

$$-i\omega\mu_0 S \left(G_{jk}\right)\left(H_x\right)_{G_jk} \approx -\frac{i\omega\mu_0}{4}(\Delta y_j + \Delta y_{j+1}) \cdot (\Delta z_k + \Delta z_{k+1}) H_x^o \tag{3.24}$$

we obtain the linear finite volume equation for the quasi H-polarization at the (j,k)th mesh node.

To summarize, the quasi E-polarization equation can be approximated with a 5-point FV scheme and 10 field components (5 electric and 5 magnetic field components, respectively) are involved in this formulation, while the quasi H-polarization equation requires a 9-point FV scheme and in total 14 field components (5 electric and 9 magnetic field components) are involved.

3.1.3. Solution of the equation system

Applying the procedure introduced in previous section for all the nodes inside the model we reach a linear equation system which characterizes the quasi E-polarization equation (e.g. 3.1) and the quasi H-polarization equation (e.g. 3.2) in the entire respected domain. If a grid point falls on the outer boundary of the grid region, then the field values at this node are replaced by the appropriate boundary values. The FV scheme simplifies particularly within the insulating air layer. In the air layer (3.7) and (3.8) become $\partial H_x/\partial z = 0$ and $\partial H_x/\partial y = 0$,

which implies that the H_x must be constant everywhere in the air. The quasi H-polarization equation need not be approximated at all and the quasi E-polarization equation reduces to the Laplace equation. Hence, within the air layer only the reduced quasi E-polarization equation is FV approximated by a 5-point FV scheme with only five coefficients.

Having the governing equations (3.1) and (3.2) approximated in all grid nodes, the resulting linear algebraic equations must be properly arranged into a common system for further computation. Because of the coupling of the governing equations through the first derivatives, a mode decomposition is hence no longer possible. The resulting linear equation system can be formed as

$$\mathbf{S_m e} = \mathbf{b} \tag{3.25}$$

where the vector $\mathbf{b}$ is the source vector that depends on the boundary conditions and source field polarization, $\mathbf{e}$ is the N dimensional vector representing the discretized electric and magnetic fields and $\mathbf{S_m}$ is a $N \times N$ coefficient matrix which depends on the M dimensional model parameter $\mathbf{m}$.

Since the storage of system coefficient matrix is the most memory consuming part of the forward procedure and the choice of an efficient linear solver is most affected by the geometry of the system coefficient matrix, it is totally worthwhile to clarify the pros and cons of the different arrangement strategy. There are obviously two different strategies for arranging the coefficients into an array, namely (a) separate storage of coefficients related to electric and magnetic field components (first a block of all coefficients related to electric field components and after-wards a block of coefficients related to magnetic field components); (b) storage of coefficients related to different field components in an alternating order. Furthermore, the coefficient matrix can be organized in column-wise or row-wise order. It leads to four different arrangements of the coefficient matrix.

Let us consider a small model with horizontal cell number N_y and vertical cell number N_z both equal 7. The vertical cell number N_z equals cell number in air, $N_{za} = 3$, plus cell number in solid earth, $N_{ze} = 4$. Figure 3.3 illustrates the model described above.

Based on this simple model I will show you the properties of the system coefficient matrix due to different arrangement strategies discussed above. Let's firstly consider the row-wise arrangement. Within a row-by-row manner the coefficient related to E_x and H_x components can be organized in (1) separate blocks; and (2) alternating order. In the first variant, all electric variables are ordered throughout the grid, from the left to the right within each row, and after-wards a block of magnetic variables inside the earth, ordered in the same way,

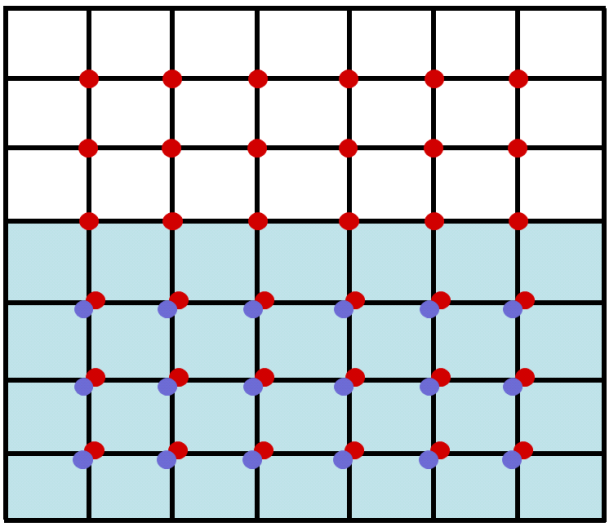

Figure 3.3.: Example model consists of a top part and a bottom part which represent the air and the solid earth, respectively. The whole model is discretized in 7x7 cells with 3x7 cells in air and 4x7 cells in the earth. The circles denote the field components to be approximated on the grid nodes. Red circles represent the E_x field components which have to be approximated on all grid nodes in the entire model and blue circles are the H_x field components which are only needed on grid nodes inside the earth.

is joined to the electric sub-array. In the second variant, within the air, electric variables are ordered in succession from the left to the right of the row, and then, inside the earth, electric and magnetic components are stacked up alternately for each row. Each of these arrangements of the variables leads to a specific form of the matrix of the system of linear algebraic equations for the approximate field values. The first variant gives a four-block matrix which contains the principal mode coefficients in the diagonal blocks, and the coupling coefficients in the anti-diagonal blocks (Fig. (3.4 left). It is obviously, that for isotropic structure, the anti-diagonal blocks will vanish and the two field modes, E_x and H_x, can be easily split into two independent matrices. The second variant mixes the principal mode coefficients and those arising due to inter-mode coupling together within each row of the matrix, but leads to a more compact, band-limited matrix (Fig. (3.4 right).

The second strategy of arrangement is the column-by-column organization of the system coefficient matrix. There are also two possibilities within this strategy, which are: the coef-

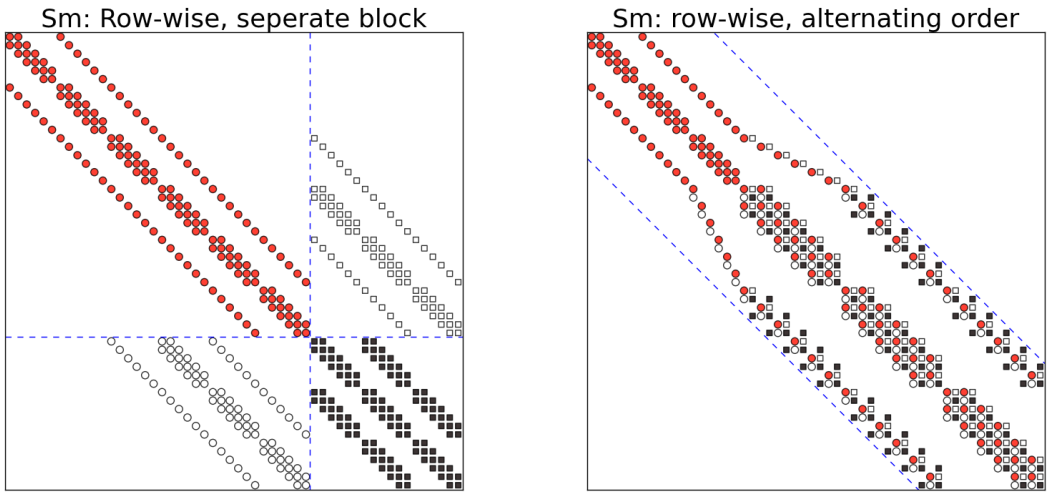

Figure 3.4.: Row-wise arrangement of the coefficients throughout the grid. Left panel: coefficients related to E_x and H_x are organized in separated blocks. Right panel: the coefficients are organized mixed in an alternating order. Circles and squares represent the electric and the magnetic components, respectively. Empty symbols in the matrix patterns are for coefficients which arise only due to anisotropy.

ficients related to E_x and H_x are organized in (3) separate blocks and (4) alternating order. In the third variant, all electric variables are ordered throughout the grid, from the top to the bottom within each column, and after-wards a block of magnetic variables inside the earth, ordered in the same way, is joined to the electric sub-array (Fig. (3.5 left). In the forth variant, within a row, electric variables are ordered in succession from the top to the earth's surface, and then, inside the earth, electric and magnetic components are stacked up alternately until the bottom of the column is reached. Then the next column is taken and processed in the same way, until the whole mesh is employed (Fig. (3.5 right). Similar to the discussion in the previous paragraph the alternating arrangement provides a compact and band-limited matrix while the separate arrangement draws a four-blocks matrix with clear separation of principal coefficient and those arising due to anisotropy. Discussion about the last two variants of arrangement can also be found in Pek and Verner (1997).

It can easily be shown that, after multiplying all the coefficients of the quasi H-polarization equations by a constant factor $i\omega\mu_0$, the system coefficient matrix $\mathbf{S_m}$ is then also symmetric, no matter which strategy of arrangement is used. Hence, the alternating arrangement of

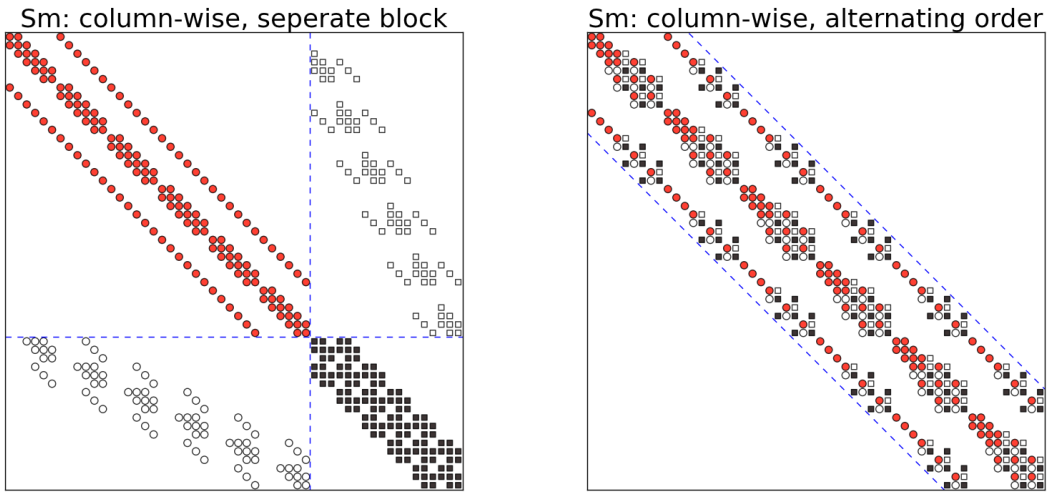

Figure 3.5.: Column-wise arrangement of the coefficients throughout the grid. Left panel: coefficients related to E_x and H_x are organized in separated blocks. Right panel: the coefficients are organized mixed in an alternating order. Circles and squares represent the electric and the magnetic components, respectively. Empty symbols in the matrix patterns are for coefficients which arise only due to anisotropy.

coefficients related to E_x and H_x components is most adequate for storage of the system coefficient matrix $\mathbf{S_m}$. Based on this arrangement the resulting matrix $\mathbf{S_m}$ is compact, band-limited and symmetric. One more thing should take into consideration is the difference of row-by-row and column-by-column arrangement. According to figure 3.4 (right) and figure 3.5 (right) we know that the both methods are equally good, the resulting matrices are both compact and band-limited. The half band-width of those two matrices can be expressed as N_y^2+1 and $2N_{ze}+N_{za}+1$ for row-by-row and column-by-column arrangement, respectively, if N_y is the number of horizontal grid steps, N_{ze} and N_{za} are the numbers of vertical grid steps within the conducting earth and in the air layer. It is clear that the band-width of the resulting matrix depends on the dimension of model, if $N_y^2 > 2N_{ze}+N_{za}$ holds for a specific model the column-by-column arrangement should be used because it yields a coefficient matrix with narrowest band, otherwise the row-by-row arrangement should be used.

The linear equation system (eq. 3.25) can be then solved using either direct methods like LU factorization, Cholesky factorization and Gaussian elimination, or iterative metods like the Gauss-Seidel method, the conjugate gradient method (CG) and the quasi-minimum residual

(QMR) method. Pek and Verner (1997) suggested a modified algorithm of gaussian elimination to solve the given equation system. Using this algorithm only the upper half-band of the matrix need to be stored in memory. Let N_{stor} be the complex numbers which have to be placed in memory and it can be easily obtained:

$$N_{stor} = \underbrace{(N_y - 1)(2N_{ze} + N_{za} - 2)}_{\text{number of equations}} \underbrace{(2N_{ze} + N_{za} + 1)}_{\text{half band-width}}$$

Figure (3.3) illustrates the strategy of storage using the modified algorithm of gaussian elimination.

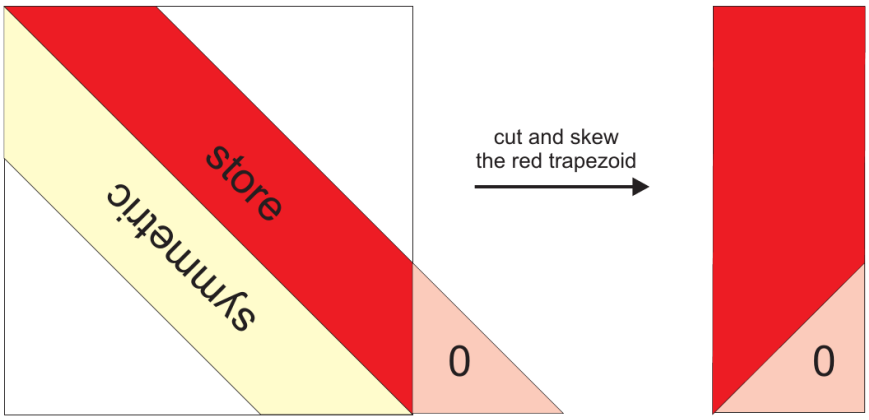

Figure 3.6.: Illustration of how the system coefficient matrix is stored using modified algorithm of gaussian elimination. Left: system coefficient Matrix S_m, only the red trapezoidal domain has to be stored. Right: the red trapezoidal subdomain of matrix S_m skewed into a rectangle for better manipulation.

3.1.4. Magnetotelluric functions on the earth's surface

Solving the linear equation system (3.25) provides us with approximated values of the field components E_x and H_x at all grid nodes. The goal of the forward problem is to evaluate all components of the magnetotelluric fields at the "receivers" located at specific position on the earth-air interface. From these, various magnetotelluric response functions and parameters can be computed as practice-oriented modeling outputs. The E_x and H_x field components

are already known as primary fields at all grid nodes. Once the "receivers" location do not coincide with the grid nodes, the E_x and H_x field components at the "receiver" location can be obtained through numeric interpolation of the corresponding field components known at the surrounding grid nodes.

In order to obtain the secondary field components (E_y, E_z, H_y and H_z) at the "receiver" location, one should first determine the secondary field components at the grid nodes surrounding the receiver location based on known primary fields. The Maxwell's equations (3.4) and (3.5) provide a possibility for computing the field components H_y and H_z. The other two field components, namely the E_y and E_z, can be obtained through equations (3.18) and (3.19). To summarize, the desired components of the secondary fields can be computed by numerical approximating of the first order partial derivatives of the primary fields, namely $\partial E_x/\partial y$, $\partial E_x/\partial z$, $\partial H_x/\partial y$ and $\partial H_x/\partial z$ contained in the formulae mentioned above. Once the desired components of secondary fields are obtained on the nodes surrounding the receiver location, we can approximate the field values at the receiver location through numerical interpolation. Within this work I use bi-linear interpolation to approximate the field value at the receiver location, which means that the interpolation process is independent of the discretized conductivities. The H_y and H_z are calculated through equations (3.4) and (3.5) which are also independent of the discretized conductivities. In contrast, the calculation of E_y and E_z are defined by equations (3.18) and (3.19). It is obvious that the accumulative conductivities are involved in the calculation.

The magnetotelluric transfer functions on the earth's surface are evaluated using the field components computed for two independent polarizations of the primary electromagnetic field. Let us assume two perpendicular polarizations of the normalized magnetic field, say $H_{x1} = -1$, $H_{y1} = 0$ and $H_{x2} = 0$, $H_{y2} = 1$. For each polarization the both induction equations defined by equations (3.1) and (3.2) have to be solved simultaneously and we obtain two different primary fields E_x and H_x defined on all nodes inside the model domain (H_x is constant inside the air). Based on the known primary fields all related secondary field components can be derived. This implies that for 2D anisotropic case the electric and magnetic fields for the two polarizations can be denoted as E_{x1}, E_{y1}, H_{x1}, H_{y1} and E_{x2}, E_{y2}, H_{x2}, H_{y2}. Hence, the impedance tensor is defined in a general form

$$\underline{\underline{\mathbf{Z}}} = \begin{pmatrix} Z_{xx} & Z_{xy} \\ Z_{yx} & Z_{yy} \end{pmatrix} = \begin{pmatrix} E_{x1} & E_{x2} \\ E_{y1} & E_{y2} \end{pmatrix} \cdot \begin{pmatrix} H_{x1} & H_{x2} \\ H_{y1} & H_{y2} \end{pmatrix}^{-1} \tag{3.26}$$

or in a matrix vector notation

$$\mathbf{E} = \underline{\underline{\mathbf{Z}}}\mathbf{H} \tag{3.27}$$

and the elements of impedance tensor can be expressed as

$$Z_{xx} = \frac{E_{x1}H_{y2} - E_{x2}H_{y1}}{H_{x1}H_{y2} - H_{x2}H_{y1}} \tag{3.28}$$

$$Z_{xy} = \frac{E_{x2}H_{x1} - E_{x1}H_{x2}}{H_{x1}H_{y2} - H_{x2}H_{y1}} \tag{3.29}$$

$$Z_{yx} = \frac{E_{y1}H_{y2} - E_{y2}H_{y1}}{H_{x1}H_{y2} - H_{x2}H_{y1}} \tag{3.30}$$

$$Z_{yy} = \frac{E_{y2}H_{x1} - E_{y1}H_{x2}}{H_{x1}H_{y2} - H_{x2}H_{y1}} \tag{3.31}$$

Equations (3.26 - 3.31) define the general form of magnetotelluric impedance tensor. From this definition simplified form can be derived by applying dimensional constraint accordingly.

Within this work only two-dimensional induction problems are considered. It means that both the conductivity structure and inducing field are independent of one horizontal coordinate direction, say the x coordinate direction. This assumption ensures that $\partial/\partial x = 0$ holds in the entire model domain. For the first polarization with $H_{x1} = -1$ and $H_{y1} = 0$, the governing equations are (3.3), (3.7) and (3.8). Clearly, field components H_x, E_x, E_y, E_z are involved into these equations, E_y and E_z are induced by time varying H_x field, whereas a E_x is also required because of the electrical anisotropy and hence, a clear mode decomposition as it in 2D isotropic case is impossible for the current situation. According to equations (3.4) and (3.5), two extra field components H_y and H_z can be derived from an existing E_x. In total, for the first polarization, four secondary field components, namely E_y E_z H_y and H_z, can be derived by existence of two primary field components, H_x and E_x. In contrast, for the second polarization with $H_{x2} = 0$ and $H_{y2} = 1$, the governing equations are (3.4), (3.5) and (3.6). One can easily observe that only H_z, E_x, E_y and E_z can be derived by existence of primary field component H_y. Ignore the z-component of electrical and magnetic field and only consider its horizontal components, equation (3.26) is reduced to

$$\underline{\underline{\mathbf{Z}}} = \begin{pmatrix} Z_{xx} & Z_{xy} \\ Z_{yx} & Z_{yy} \end{pmatrix} = \begin{pmatrix} E_{x1} & E_{x2} \\ E_{y1} & E_{y2} \end{pmatrix} \cdot \begin{pmatrix} H_{x1} & 0 \\ H_{y1} & H_{y2} \end{pmatrix}^{-1} \tag{3.32}$$

with

$$Z_{xx} = \frac{E_{x1}H_{y2} - E_{x2}H_{y1}}{H_{x1}H_{y2}} \tag{3.33}$$

$$Z_{xy} = \frac{E_{x2}}{H_{y2}} \tag{3.34}$$

$$Z_{yx} = \frac{E_{y1}H_{y2} - E_{y2}H_{y1}}{H_{x1}H_{y2}} \tag{3.35}$$

$$Z_{yy} = \frac{E_{y2}}{H_{y2}} \tag{3.36}$$

Equations (3.32 - 3.36) define the impedance tensor for general 2D structure with anisotropic conductivity, which is a full and non-diagonalizable tensor. Other magnetotelluric functions, such as apparent resistivity and phase, can be easily computed based on known impedance tensor.

If the 2D structure is considered to be isotropic, the Maxwell's equations can be split into two distinct modes as described in section A.2.2 on page 137. Only three field components are involved in each polarization, hence, equation (3.26) can be further reduced to

$$\underline{\underline{\mathbf{Z}}} = \begin{pmatrix} Z_{xx} & Z_{xy} \\ Z_{yx} & Z_{yy} \end{pmatrix} = \begin{pmatrix} 0 & E_{x2} \\ E_{y1} & 0 \end{pmatrix} \cdot \begin{pmatrix} H_{x1} & 0 \\ 0 & H_{y2} \end{pmatrix}^{-1} \tag{3.37}$$

with

$$Z_{xx} = 0 \tag{3.38}$$

$$Z_{xy} = \frac{E_{x2}}{H_{y2}} \tag{3.39}$$

$$Z_{yx} = \frac{E_{y1}}{H_{x1}} \tag{3.40}$$

$$Z_{yy} = 0 \tag{3.41}$$

which define the impedance tensor for 2D isotropic structure.

3.2. Synthetic 2D model study

3.2.1. Forward response of an anisotropic 2D model

In this section, I use a simple synthetic model to demonstrate the effects of electrical anisotropy which aims to understand its fundamental properties. The model is shown in

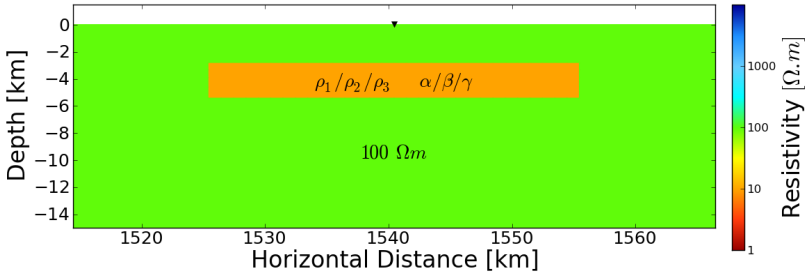

Figure 3.7.: Simple test model consists of a conductive rectangular block embedded into an isotropic homogeneous half-space with resistivity of $\rho_1 = 100\,\Omega\mathrm{m}$. The block is chosen to be anisotropic. The effects of anisotropy are studied by varying the principal resistivity and rotation angles and comparing the forward responses calculated from the model generated therefrom. The black triangular denotes a MT site located above the conductive rectangular block.

figure 3.7. It consists of a conductive rectangular block embedded into an isotropic homogeneous half-space with resistivity of $\rho_1 = 100\,\Omega\mathrm{m}$. The conductive block is chosen to be anisotropic with initial principal resistivity values of $\rho_1/\rho_2/\rho_3 = 10/50/10\,\Omega\mathrm{m}$ and rotation angles of $\alpha/\beta/\gamma = 0°$. In the following, the principal resistivity values and the rotation angles of the conductive square block are varied in a wide range. The forward responses of the model generated therefrom are calculated in order to study the effects of different anisotropy types.

In the first attempt, I vary the principal resistivity values $\rho_{1,2,3}$ one at a time from $10\,\Omega\mathrm{m}$ to $100\,\Omega\mathrm{m}$ with a step length of 20 (except the last step, which is only 10 instead of 20). The rotation angles remain unchanged, namely $\alpha/\beta/\gamma = 0°$. A single MT site, located right above the conductive block (the black triangular in fig. 3.7), is used to demonstrate the forward response. The xy- and yx-components of apparent resistivity and phase of the individual variation are displayed in figure 3.8, 3.9 and 3.10. For how the apparent resistivity and phase are calculated, the reader is referred to eqs. (2.24) and (2.25) on page 8.

If the pricipal resistivity value defined in x-direction, ρ_1, is varying, the xy-component of both the apparent resistivity and the phase change their tracks accordingly while the yx-component remains unchanged (fig. 3.8). In contrast to that, an opposite situation can be observed if the principal resistivity value defined in y-direction, ρ_2, is varying. The yx-component of both the apparent resistivity and the phase reconstruct their curvature according to the changes of ρ_2 while the xy-component remains unchanged (fig. 3.9). If ρ_1 and ρ_2 are fixed and only

ρ_3, the principal resistivity value defined in z-direction, is varying, this kind of change will not be perceived by both of components (fig. 3.10). Therefore, we may deduce that within a 2D anisotropic structure the xy-component of MT apparent resistivity and phase is only sensitive to the resistivity variation in the x coordinate direction, while the yx-component is only sensitive to the resistivity variation in y-coordinate direction. In addition to this, a resistivity variation in z-coordinate direction will not be reflected into both component of the apparent resistivity and the phase (fig. 3.10). The last phenomenon is caused by the nature of magnetotelluric induction. Within the magnetotelluric induction the incident electromagnetic wave is considered as plane wave and diffuse into the Earth's subsurface, therefore, the horizontal resolution of the MT method is comparably higher than its vertical resolution.

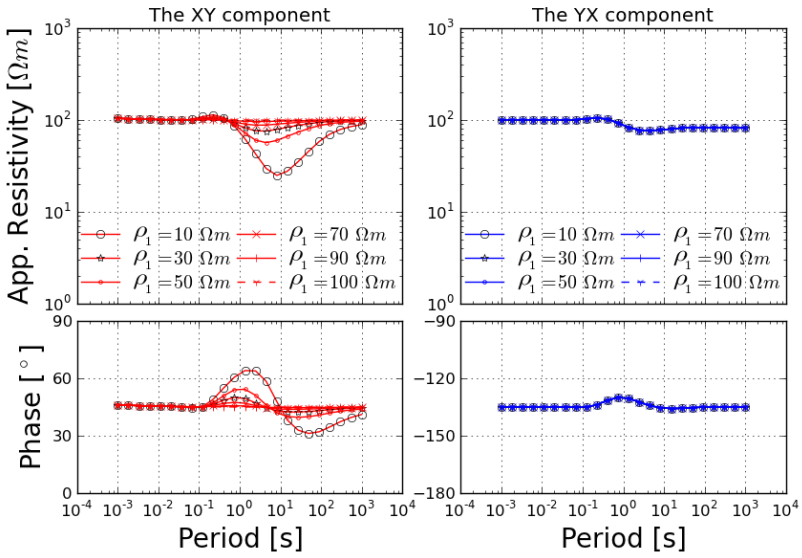

Figure 3.8.: xy- and yx-components of apparent resistivities and phases of a MT site located above the conductive block (see fig. 3.7). The block is defined with $\rho_2/\rho_3 = 50/10\,\Omega\mathrm{m}$ and $\alpha/\beta/\gamma = 0°$, while ρ_1 varies from $10\,\Omega\mathrm{m}$ to $100\,\Omega\mathrm{m}$ with a step length of 20 (the last step only with 10). The xy-component is sensitive to the resistivity variation in x-direction while the yx-component remains unchanged.

In the second attempt, the principal resistivity values are fixed with $\rho_1/\rho_2/\rho_3 = 10/50/10\,\Omega\mathrm{m}$ and we change the rotation angles α, β and γ one at a time from $0°$ to $180°$ with a step length of $30°$ while the other two angles are fixed with $0°$. The forward responses are represented by xy- and yx-component of apparent resistivity and phase at a single MT site located above the conductive block (see fig. 3.7). The xy- and yx-components of apparent resistivity and

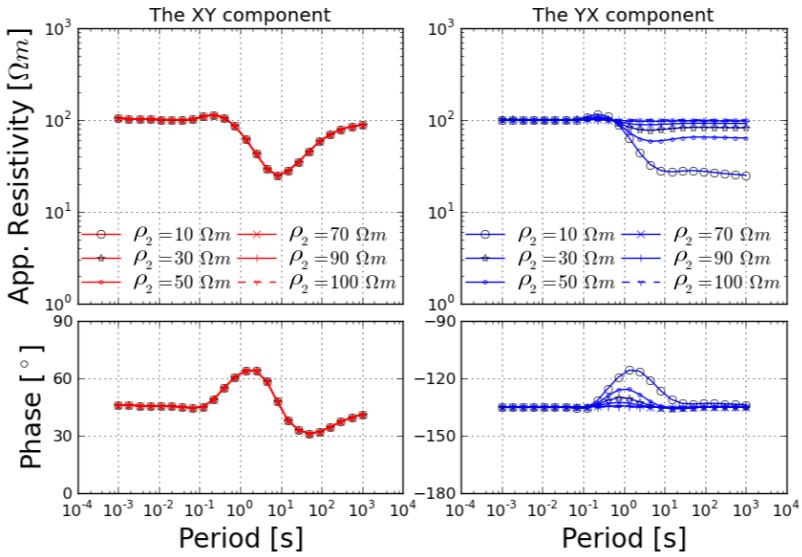

Figure 3.9.: xy- and yx-components of apparent resistivities and phases of a MT site located above the conductive block (see fig. 3.7). The block is defined with $\rho_1/\rho_3 = 10/10\,\Omega\mathrm{m}$ and $\alpha/\beta/\gamma = 0°$, while ρ_2 varies from $10\,\Omega\mathrm{m}$ to $100\,\Omega\mathrm{m}$ with a step length of 20 (the last step only with 10). The yx-component is sensitive to the resistivity variation in y-direction while the xx-component remains unchanged.

phase of the individual variation are displayed in figure 3.11, 3.12 and 3.13.

If the first rotation angle α is varying while the principal resistivities and other rotation angles are fixed, its effects are accordingly reflected into both the xy- and yx-component of apparent resistivity and phase (fig. 3.11). The same phenomena can be observed if we vary γ instead of α and fix the other parameters (fig. 3.13). This is because the z-x'-z'' convention of Euler's rotations is used to transform between the full occupied conductivity tensor and its representative with principal resistivity values and rotation angles. The rotation angles α and γ are defined to be rotations about the axes z and z'', where z'' is the new z-axis if a rotation about the x-axis (denoted by angle β) is involved. Hence, their effects have to be the same if only individual rotation are considered instead of a series of consecutive rotations. This kind of anisotropy is called azimuthal anisotropy, also known as horizontal anisotropy. For the detail about different anisotropy types and the Euler's rotations, the reader is referred to section (2.2). varying the second rotation angle β and keeping the other parameters unchanged will cause the so called dipping anisotropy. For this type of anisotropy, the yx-component of apparent resistivity and phase is able to reflect the changes

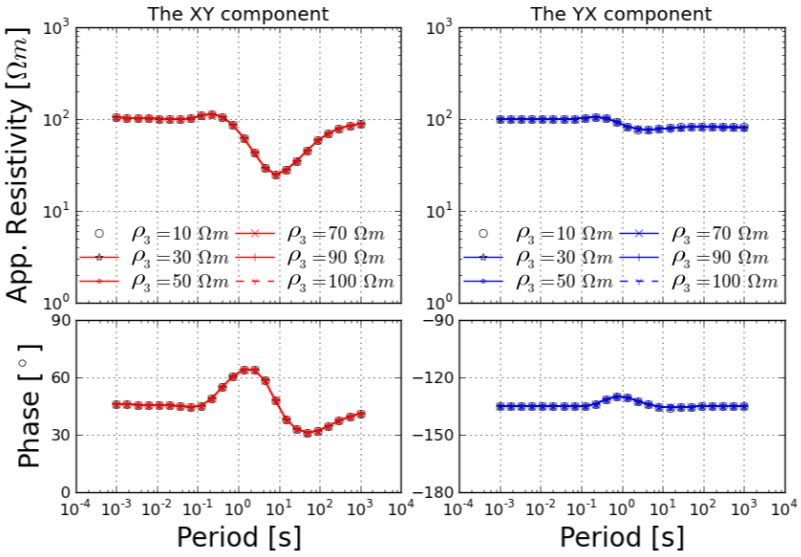

Figure 3.10.: xy- and yx-components of apparent resistivities and phases of a MT site located above the conductive block (see fig. 3.7). The block is defined with $\rho_1/\rho_2 = 10/50\,\Omega\mathrm{m}$ and $\alpha/\beta/\gamma = 0°$, while ρ_3 varies from $10\,\Omega\mathrm{m}$ to $100\,\Omega\mathrm{m}$ with a step length of 20 (the last step only with 10). Both xy- and yx-components are insensitive to the resistivity variation in z-direction.

of β while the xy-component remains the same during all the variations (fig. 3.12). One can summarize that the both xy- and yx-components of MT apparent resistivity and phase are sensitive to the azimuthal anisotropy but only the yx-component is sensitive to the dipping anisotropy. Furthermore, a symmetry can be observed from these tests. For instance, no matter it is azimuthal or dipping anisotropy, a rotation of $30°$ will provide the same responses as a rotation of $150°$ about the same axis. This is because if a rotation angle ϕ is measured about a rotation axis a, then an angle of $-\phi$ about axis $-a$ will produce the same rotation matrix. Since the electrical resistivity is non-negative, the symmetry between ϕ and $-\phi$ is equivalent to the symmetry between ϕ and $180° - \phi$. In other words, it is not able to distinguish an anisotropy rotated ϕ degrees to the reference axis from other anisotropy with the same principal resistivity values but rotated $180 - \phi$ degrees to the same axis.

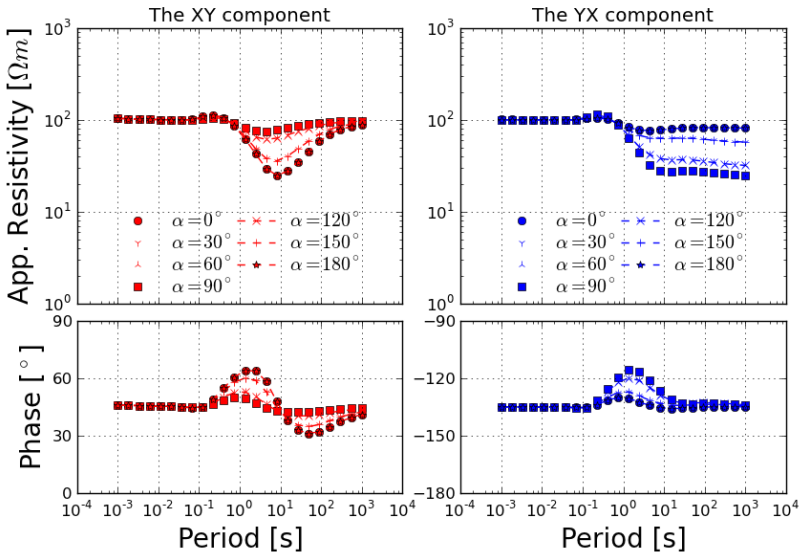

Figure 3.11.: xy- and yx-components of apparent resistivities and phases of a MT site located above the conductive block (see fig. 3.7). The block is defined with $\rho_1/\rho_2/\rho_3 = 10/50/10\,\Omega\mathrm{m}$ and $\beta/\gamma = 0°$, while α varies from $0°$ to $180°$ with a step length of $30°$. As we can observe, both xy- and yx-components are sensitive to horizontal anisotropy.

3.2.2. MT impedance phase out of quadrant

The impedance phase describes the phase shift between the components of the electrical field and magnetic field (see equation 2.25). As a result of the principle of causality of the interaction between electric and magnetic fields induced in the Earth, the phases should lie in the first or third quadrant $[0°, 90°]$ and $[-90°, -180°]$ (or $[180°, 270°]$, like some author would prefer to use). This implies that the imaginary and real impedance have the same sign. However, impedance phase out of expected quadrant are sometimes observed in magnetotelluric surveys. Because they are little understood and can not be modeled by standard 1D and 2D methods, they are usually excluded from inversion procedures. Recently, several attempts have been made to explain and model the large phase anomalies. For instance, Egbert (1990) shows that the principle of causality can be violated by certain physically realizable 3D conductivities. With a model of sharp channelling body he demonstrated that the large phase could caused by strong current channelling and reproduced large phase anomalies observed at some of the EMSLAB data set (EMSLAB-Group, 1988). Livelybrooks et al. (1996) explained a large phase anomaly found in a survey across the Trillabelle ore body with 3D induction within the body coupled with current channelling through neighbouring faults.

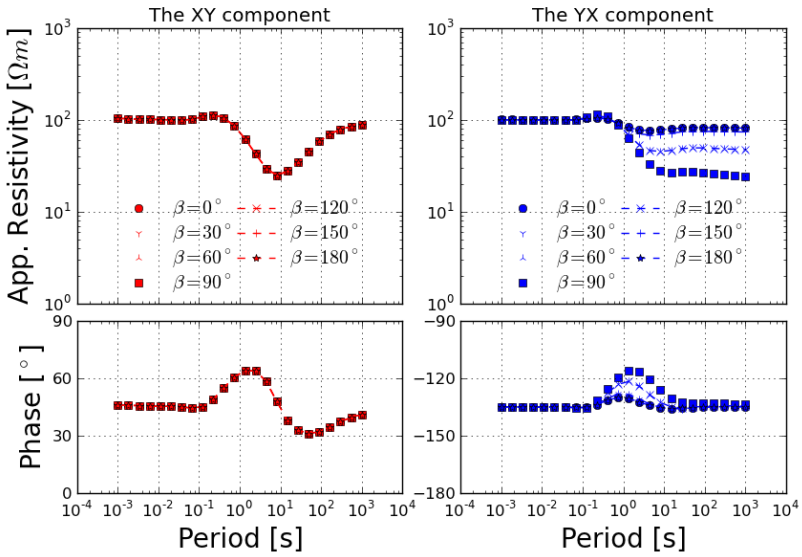

Figure 3.12.: xy- and yx-components of apparent resistivities and phases of a MT site located above the conductive block (see fig. 3.7). The block is defined with $\rho_1/\rho_2/\rho_3 = 10/50/10\,\Omega\mathrm{m}$ and $\alpha/\gamma = 0°$, while β varies from $0°$ to $180°$ with a step length of $30°$. Only the yx-component is sensitive to dipping anisotropy.

Lezaeta (2001) explained large phase anomalies observed in the Andes at the Precordillera and the coast with models of near-surface elongated 3D conductors being electromagnetically coupled with a conductive ocean and conductive mantle, producing strong current channelling and magnetic distortions. Weckmann (2002) modelled large phase anomalies in a survey in Namibia with a conductive local ring-structure and Pous et al. (2002) attempted to model more regional large phase anomalies found in Tenerife island using 3D, highly conductive, channel structures. Ichihara and Mogi (2009) modelled large phase anomalies using a 3D L-shaped conductor model.

Pek and Verner (1997) have suggested that a combination of two azimuthal anisotropies with anisotropy strikes perpendicular to each other could produce phases out of quadrant. Based on this suggestion, Heise and Pous (2003) modified the model suggested by Pek and Verner (1997) and reproduced large phase anomalies observed in SW Iberia. In this section, I will follow the same idea and try to reconstruct the phenomenon of phase out of quadrant through the use of anisotropic modeling based on a few simple 2D synthetic models

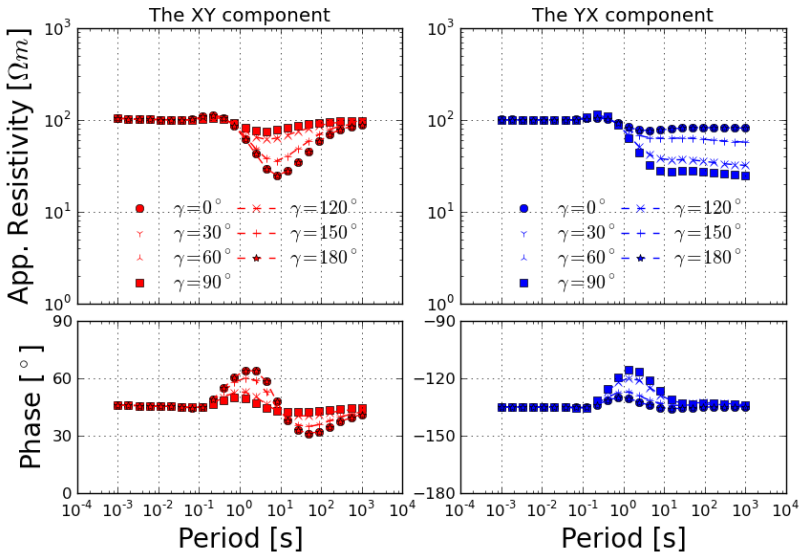

Figure 3.13.: xy- and yx-components of apparent resistivities and phases of a MT site located above the conductive block (see fig. 3.7). The block is defined with $\rho_1/\rho_2/\rho_3 = 10/50/10\,\Omega\mathrm{m}$ and $\alpha/\beta = 0°$, while γ varies from $0°$ to $180°$ with a step length of $30°$. Both xy- and yx-components are sensitive to the variation in rotation angle γ and the response are coincident with those for horizontal anisotropy.

Lateral extension

I study at first a combination of two different anisotropic blocks. The initial model (fig. 3.14, left) consists of a $300\,\mathrm{m}$ isotropic surface layer with a resistivity of $30\,\Omega\mathrm{m}$ and an anisotropic block starting at a depth of $300\,\mathrm{m}$ embedded in a medium of $100\,\Omega\mathrm{m}$. The principal resistivities of the block are $\rho_1/\rho_2/\rho_3 = 50/0.5/50\,\Omega\mathrm{m}$ and the anisotropy strike α_S is $120°$. The block is underlain by an isotropic layer with a resistivity of $15\,\Omega\mathrm{m}$. Beneath the isotropic layer a second anisotropic block with $\rho_1/\rho_2/\rho_3 = 30/0.3/30\,\Omega\mathrm{m}$ and $\alpha_S = 30°$ (perpendicular to α_S of the first block) is embedded in an isotropic half-space with $100\,\Omega\mathrm{m}$. The second, deeper anisotropic block has a lateral extension of $15\,\mathrm{km}$ in the first (fig. 3.14, left upper panel), and $80\,\mathrm{km}$ in the second (fig. 3.14, left lower panel) model, respectively.

The forward responses are displayed in figure 3.14 (right) as apparent resistivities and phases in xy and yx component, respectively. Comparing the responses of both models we see that the phases of yx component (Φ_{yx}) for the second model (fig. 3.14, left lower panel) at sites

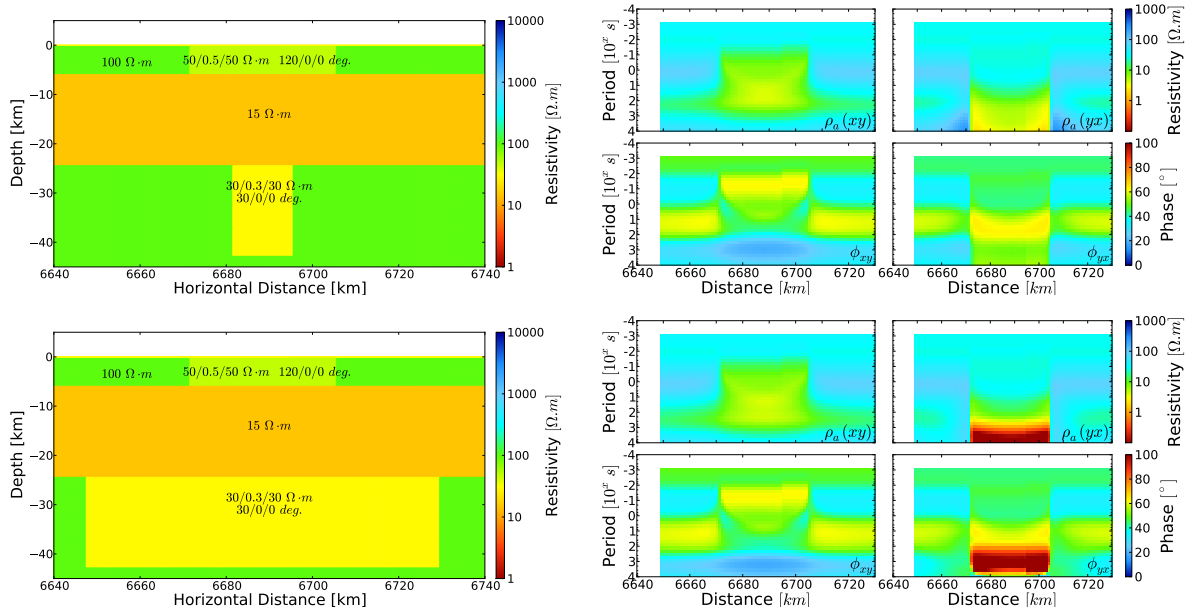

Figure 3.14.: Models (left) and their forward responses (right). The models differ only in lateral extension of anisotropy block. The lateral extension of the second block is about $15\,\mathrm{km}$ in the first model (left upper panel) and $80\,\mathrm{km}$ (left lower panel) in the second model. The major difference in the responses appears in the yx component. Phases over $90°$ occur if the lateral extension of the deeper anisotropy block is greater than it of the shallower anisotropy block.

above the first anisotropy block leave the quadrant at a period of $\approx 100\,s$ (fig. 3.14, right lower panel), while they are smaller than $90°$ (fig. 3.14, right upper panel) for the first model (fig. 3.14, left upper panel) with the narrower deep anisotropic block.

Depth

In a second step, I used the same anisotropy parameters as described above. The initial model consists of a $300\,\mathrm{m}$ isotropic surface layer and a isotropic half-space with resistivity of $100\,\Omega\mathrm{m}$. Two anisotropy blocks are embedded in the half-space. The first block started at depth of $300\,\mathrm{m}$ and shaped as a trapezoid. In this attempt I vary the depth of the second block. In the first model (fig. 3.15, left upper panel) the second block started at a depth of $1.8\,\mathrm{km}$ and in the second model (fig. 3.15, left lower panel) started at a depth of $6.8\,\mathrm{km}$.

In the forward responses (fig. 3.15, right) we see that the phases Φ_{yx} for the second model

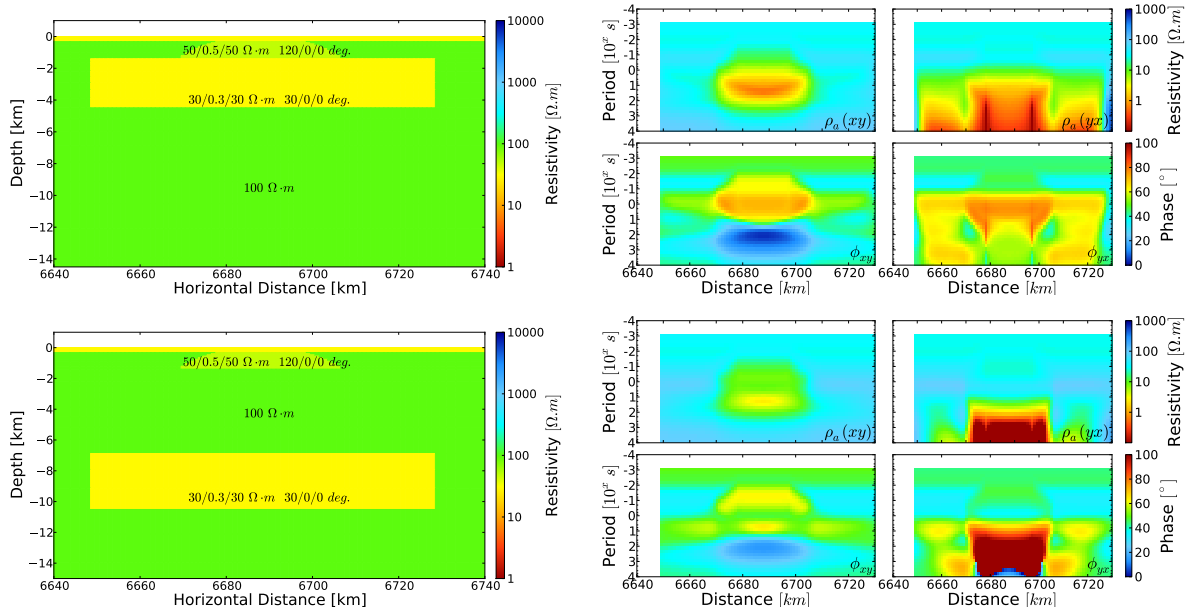

Figure 3.15.: Models (left) and their forward responses (right). The models differ by depth of the second anisotropy block. In the first model (left upper panel) the second block starts in a depth of $1.8\,\mathrm{km}$ and in the second model (left lower panel) the block starts in a depth of $6.8\,\mathrm{km}$. The phases of yx component for the model with the deeper anisotropic block become larger than $90°$ at periods $> 10\,\mathrm{s}$ at sites above the first block. For the model with the shallower block all phases are smaller than $90°$.

become larger than $90°$ at periods $> 10\,\mathrm{s}$ at sites above the first block, while those for the first model are all smaller than $90°$. In this attempt the second anisotropy block has always sufficiently greater lateral extension than the first anisotropy block, but the phase anomalies can only be observed by model with anisotropy block in adequate depth. Besides the lateral extension of the anisotropy block, also the depth is one of those key conditions under which phase anomalies appear.

Rotation angle

In a third test I use a similar model as described above for step two. The model contains a $300\,\mathrm{m}$ isotropic surface layer and an isotropic half-space with resistivity of $100\,\Omega\mathrm{m}$. Two anisotropic blocks are embedded in the half-space. The first block starts directly beneath the surface layer and the second block in a depth of $6\,\mathrm{km}$. They have the principal resistivities

$\rho_1/\rho_2/\rho_3 = 50/0.5/50\,\Omega\mathrm{m}$ and $\rho_1/\rho_2/\rho_3 = 30/0.3/30\,\Omega\mathrm{m}$, respectively. In this attempt I vary the anisotropy strike angle α_{S1} and α_{S2} for both blocks.

The forward response for the model with $\alpha_{S1} = \alpha_{S2} = 0^\circ$ is displayed in the right upper panel of figure 3.16. The phases of the yx component approach 90° for long periods. For $\alpha_{S1} = 60^\circ$ and $\alpha_{S2} = 120^\circ$ (fig. 3.16, left lower panel) the yx component phases become larger than 90° for periods $> 10\,\mathrm{s}$, while they stay below 90° for $\alpha_{S1} = 90^\circ$ and $\alpha_{S2} = 120^\circ$ (fig. 3.16, right lower panel). Comparing the three examples, we see that model with different combination of strike angle in both shallow and deep blocks produce forward responses with pronounced difference. This can be observed not only in yx component ($\rho_a(yx)$ and Φ_{yx}) but also in xy component ($\rho_a(xy)$ and Φ_{xy}). A possible explanation is that a change of strike angle forces the current flow to change its preferred direction from the shallow to the deep block. According to this fact one may conclude that the anisotropy strike angle influences forward responses significantly and phase greater than 90° will appear if the strike angle of both blocks differ by an adequate amount.

Conclusions

Phases greater than 90° can only be modeled by a combination of a deep and a shallow anisotropic block. I varied several model parameters to study the changes in forward responses. For the models used here one can conclude that phases out of the first quadrant occur when: (i) the anisotropy ratio (ρ_{max}/ρ_{min}) is high (for both blocks); (ii) the deep anisotropic block has a much larger lateral extension than the shallow block; (iii) the deep anisotropic block is located in greater depth; (iv) the angles of anisotropy of both blocks differ by a considerable amount. In our models the difference should be at least 45° so that the preferred direction of current flow changes significantly from the shallow to the deep block.

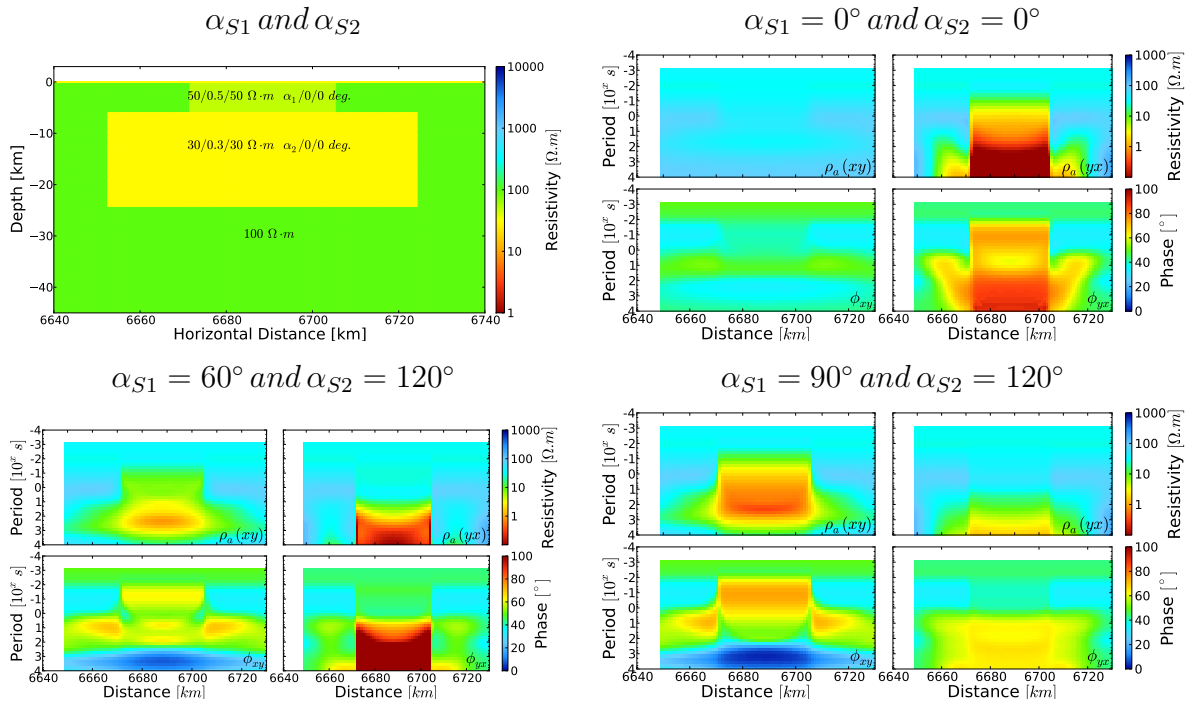

Figure 3.16.: Model (left upper panel) and its forward responses with different anisotropy strike angles. The model contains the same surface layer, background medium and resistivities for both anisotropic blocks as the models in fig. 3.15. The strike angles α_{S1} and α_{S2} for the shallow and the deep block are varied (left upper panel). The forward responses are displayed as apparent resistivities and phases in xy and yx component.

Chapter 4.

MT inverse problem

In geophysics a concept of the Earth has to be found based on a limited number of measurements. It represents, in most cases, an inverse problem. Solutions are found by the iterative minimization of the misfit between the data and the model's response (also known as forward response or predicted data). In section 4.1 the reader is introduced to the methodology of non-linear minimization. In particular, gradient techniques and Newton type methods are described. Many multi-dimensional inverse problems are known to be non-unique to solve and numerically unstable, depicted by the term ill-posed. Hence, the inverse problem has to be regularized by appropriate techniques. One successful way is to introduce a penalty functional, which is weighted by regularization parameter. In every iteration step, a linear sub-problem representing a large-scale system of equations has to be solved. To accomplish this, equation solver on the basis of conjugate gradient methods can be adapted to the specific formulation. Section 4.2 describes the basic concept of 2D MT inversion with consider of the electrical anisotropy. The computation of the sensitivity matrix for 2D anisotropic case differs from which for isotropic 2D and 3D case and is the key step towards a 2D anisotropic inversion. The implementation of the inversion scheme according to the concept of Egbert and Kelbert (2012) is explained. In the last section a few synthetic models are used to test the functionality of the implemented inversion procedure. The tests are focused on three main points, namely the choice of regularization parameters, resolution ability and efficiency.

4.1. Inversion methods

4.1.1. Inversion methodology

The central objective of inversion is to provide a mathematical framework to transform measured data from the data space to the model space in order to estimate model parameters. Assume a set of N measurements affected by the physical property m of the subsurface. The set of all data is represented by the data vector $\mathbf{d} = (d_1, d_2, \cdots, d_N)^T$, where the superscript T denotes the transpose of vector or matrix. The N-dimensional data vector resides in the data space. As we know, all measured data are contaminated with an error vector $\mathbf{e}$. We are then interested in finding a spatial parameter distribution $m(r)$ that explains our data d to a certain degree. The model m we are seeking contains M model parameters and can be presented as $\mathbf{m} = (m_1, m_2, \cdots, m_M)^T$. The model vector resides in the model space. The projection from model space to data space is achieved by the forward modeling operator $\mathbf{f}$, which is function of $\mathbf{m}$. The operator $\mathbf{f}(\mathbf{m})$ generates the predicted data or forward response. For linear problems there exists a linear relation between $\mathbf{m}$ and $\mathbf{f}$, which can be expressed by a matrix-vector multiplication $\mathbf{f}(\mathbf{m}) = \mathbf{F} \cdot \mathbf{m}$. Examples for linear relations in geophysics are gravimetry, magnetics, or vertical seismic profiling. For non-linear problems the forward operation depends on the model $\mathbf{m}$ itself, which holds for all methods that are based on Maxwell's equations. The model parameter vector $\mathbf{m}$ and the data vector $\mathbf{d}$ are related to each other through:

$$\mathbf{f}(\mathbf{m}) = \mathbf{d} + \mathbf{e}$$

The inversion process attempts to find a model that reproduces the measured data with their error. Beginning from a starting model $\mathbf{m}_0$ (also known as initial guess model), an iterative process is applied to update the model until data fit or convergence is achieved. In each iteration step k a new model is calculated by adding a model update $\Delta\mathbf{m}_k$

$$\mathbf{m}_{k+1} = \mathbf{m}_k + \Delta\mathbf{m}_k \tag{4.1}$$

A Taylor approximation of first order yields

$$\begin{aligned} \mathbf{f}(\mathbf{m}_k + \Delta\mathbf{m}_k) &= \mathbf{f}(\mathbf{m}_k) + \frac{\partial \mathbf{f}(\mathbf{m}_k)}{\partial \mathbf{m}} \Delta\mathbf{m}(\mathbf{m}_k) + \cdots \\ &\approx \mathbf{f}(\mathbf{m}_k) + \mathbf{J}\Delta\mathbf{m}_k \end{aligned} \tag{4.2}$$

where the partial derivative of the model response with respect to the model parameters is called Jacobian or sensitivity matrix $\mathbf{J} \in \mathbb{R}^{N \times M}$ with the elements

$$J_{ij}(\mathbf{m}_k) = \frac{\partial f_i(\mathbf{m}_k)}{\partial m_j} \tag{4.3}$$

Setting the response of the new model $\mathbf{f}(\mathbf{m} + \Delta\mathbf{m})$ equal to the data $\mathbf{d}$ we obtain the non-quadratic equation

$$\mathbf{J}\Delta\mathbf{m} = \mathbf{d} - \mathbf{f}(\mathbf{m}) \tag{4.4}$$

which has to be solved in some sense to minimize the residual vector $\mathbf{d} - \mathbf{f}(\mathbf{m})$. Usually, for each data point d_i an error e_i is known or can be estimated, which is used for weighting the residual. Using an L_p-norm of the weighted residual, a data functional Φ_d to be minimized is defined by

$$\Phi_d(\mathbf{m}) = \sum_{i=1}^{N} \left| \frac{d_i - f_i(\mathbf{m})}{e_i} \right|^p = \|\mathbf{D}(\mathbf{d} - \mathrm{f}(\mathbf{m}))\|_p^p \tag{4.5}$$

with $\mathbf{D} = diag(1/e_i)$ is a diagonal $N \times N$ matrix.

Generally, different values for p can be used (Farquharson and Oldenburg, 1998) corresponding to the expected noise characteristics. The L_1-norm is particularly advantageous, if the noise has a long-tailed distribution. Since it is less sensitive to outliers in the data, a L_1 minimization procedure is often called "robust inversion" (Claerbout and Muir, 1973).

In the following, we assume the noise to be Gaussian corresponding to the use of the L_2-norm measure. The mean value of the data functional $\chi^2 = \Phi_d/N$ is often considered for linking to the statistical nature. A value of $\chi^2 = 1$ implies the data being fitted within their errors. Thus, the functional norm can be written as

$$\Phi_d = [\mathbf{D}(\mathbf{d} - \mathbf{f}(\mathbf{m}))]^T [\mathbf{D}(\mathbf{d} - \mathbf{f}(\mathbf{m}))] = (\mathbf{d} - \mathbf{f}(\mathbf{m}))^T \mathbf{D}^T \mathbf{D}(\mathbf{d} - \mathbf{f}(\mathbf{m})) \tag{4.6}$$

As we will see later, the functional to be minimized can be expanded by other terms yielding a combined Φ, which is the so called penalty functional or objective functional. At this stage we first have $\Phi = \Phi_d$.

Newton type method

It is obvious that one must seek the minimum of penalty functional Φ. we start with a second order Taylor series for the functional Φ of an updated model $\mathbf{m} + \Delta\mathbf{m}$

$$\Phi(\mathbf{m} + \Delta\mathbf{m}) \approx \Phi(\mathbf{m}) + (\nabla_m \Phi(\mathbf{m}))^T \Delta\mathbf{m} + \frac{1}{2}\Delta\mathbf{m}^T(\nabla_m^2 \Phi(\mathbf{m}))^T \Delta\mathbf{m} \tag{4.7}$$

where the first derivative ∇_m denotes the gradient operator and can be expressed as

$$\nabla_m = \left(\frac{\partial}{\partial m_1}, \frac{\partial}{\partial m_2}, \cdots, \frac{\partial}{\partial m_M}\right)^T$$

and the second derivative $\nabla_m^2 \Phi$ is the Hessian matrix with the elements

$$(\nabla_m^2 \Phi)_{ij} = \left(\nabla_m \nabla_m^T \Phi\right)_{ij} = \frac{\partial^2 \Phi}{\partial m_i \partial m_j} = H_{ij}$$

The second order approximation of $\Phi(\mathbf{m} + \Delta\mathbf{m})$ is minimized by setting its first partial derivative with respect to $\Delta\mathbf{m}$ to zero, which results in

$$\nabla_m \Phi(\mathbf{m}) + \nabla_m^2 \Phi(\mathbf{m}) \Delta\mathbf{m} = 0$$

Hence, the model update $\Delta\mathbf{m}_k$ for each iteration can be obtained by solving the equation

$$(\nabla_m^2 \Phi) \Delta\mathbf{m}_k = -\nabla_m \Phi \tag{4.8}$$

Equation (4.8) represents a linear sub-problem to be solved in every iteration step. For the functional Φ_d as defined by (4.6) holds

$$\begin{aligned} \mathbf{H}_{d,k} &= \nabla_m \nabla_m^T \Phi_d = \nabla_m (\mathbf{J}^T \mathbf{D}^T \mathbf{D}(\mathbf{f}(\mathbf{m}_k) - \mathbf{d})) \\ &= \mathbf{J}^T \mathbf{D}^T \mathbf{D} \mathbf{J} + (\nabla_m \mathbf{J}^T) \mathbf{D}^T \mathbf{D}(\mathbf{f}(\mathbf{m}_k) - \mathbf{d}) \end{aligned} \tag{4.9}$$

for iteration k. The second term at the right hand side is generally difficult to compute. It can be neglected, if the problem is not strongly non-linear (e.g. $\nabla_m^T \mathbf{J}^T$ is small). The gradient $\mathbf{g}_{d,k}$ of the functional Φ_d can be easily computed from the sensitivity matrix using the chain rule

$$\mathbf{g}_{d,k} = \nabla_m \Phi_d(\mathbf{m}_k) = \mathbf{J}^T \mathbf{D}^T \mathbf{D}(\mathbf{f}(\mathbf{m}_k) - \mathbf{d}) \tag{4.10}$$

The linear subproblem (4.8) can be rewritten as

$$\begin{aligned} \mathbf{J}^T\mathbf{D}^T\mathbf{D}\mathbf{J}\Delta\mathbf{m}_k &= -\mathbf{J}^T\mathbf{D}^T\mathbf{D}(\mathbf{f}(\mathbf{m}_k)-\mathbf{d}) \\ \text{or} \quad \mathbf{H}\Delta\mathbf{m} &= -\mathbf{g} \end{aligned} \tag{4.11}$$

which represents the so called normal equation, also known as the unconstrained least square equation.

The method using the Hessian approximation $\mathbf{H}_{d,k} = \mathbf{J}^T\mathbf{D}^T\mathbf{D}\mathbf{J}$ is called Gauss-Newton method. Besides the easier computation it has the advantage that the Hessian approximation is positive semi-definite, which guarantees the Gauss-Newton step to be a descent direction. Due to the second order of the Taylor approximation the Gauss-Newton method, one of the Newton type methods, has quadratic convergence. Thus, the number of iterations will be small, if the starting model is not far away from the minimum. If there are several local minima, the solution is uniquely defined by the starting model. The quest for a global minimum may be achieved by starting from a set of different starting models $\mathbf{m}_0$. The crucial point of Gauss-Newton method is to recalculate the approximated Hessian matrix in every iteration, which can be very time consuming.

Gradient based methods

Another way to minimize the functional defined by (4.6) is using of gradient based minimization methods. Since the gradient of a function denotes the steepest ascent direction, it is easily to see, that the minimum of a function will be found if we follow the opposite direction of the gradient, which is known as the direction of the steepest descent. Thus, to minimize Φ, the model update for each iteration can be considered as a proportion of the negative gradient of Φ, namely $-\mathbf{g}$ according to (4.10). A step length τ, the proportional coefficient, of the descent step has to be estimated such that $\Phi(\mathbf{m}_k - \tau\mathbf{g}_k)$ for iteration k is minimized. A procedure, which tries to search for an optimum solution along the line defined by varying τ is referred to as line search. Repeating the process described above several times we will obtain a solution which is close enough to the desired minimum. This is the method of Steepest Descent. Within this method the forward response and the functional's gradient have to be calculated for each iteration. The latter can be achieved by the explicit use of the Jacobian matrix or by additional forward calculations. The convergence rate for this method is very slow for ill-posed problems. This results in many forward calculations, which are generally very time-consuming. Hence, this method is very simple to implement, but rarely of practical use.

A more sophisticated technique of non-linear minimization is the conjugate gradient method (NLCG). The basic idea of this method is to find a set of conjugate directions and to compute accompanying weights in a manner that every search direction is used only once. As a result, convergence is generally fast compared to the Steepest Descent Method. NLCG has been successfully used for the inversion of magnetotelluric (e.g. Rodi and Mackie (2001) for 2D case and Newman and Alumbaugh (2000) for 3D case). In contrast to Gauss-Newton method and the method of Steepest Descent, NLCG is more efficient and requires the lowest computer memory for the following reasons. Firstly, as a gradient based method there is no need to compute the approximated Hessian matrix. Secondly, the convergence rate of NLCG is slower then Gauss-Newton method but faster than the Steepest Descent method. Finally, within NLCG the gradient $\mathbf{g}$ can be obtained without forming the sensitivity matrix $\mathbf{J}$ explicitly (Egbert, 2006). They make the NLCG method a realistic option to solve large scale inversion problems. The reader is referred to Nocedal and Wright (1999) for more detailed discussion about the minimization techniques described above.

4.1.2. Regularization

In inversion problems we usually have more free model parameters than data. It implies that there will exist a lot of models fitting the same data set equally well. In many cases the model obtained through the above described minimization scheme contains both well resolved and poorly resolved model parameters. In other words, minimize equation (4.6) alone would probably lead to highly oscillating models with huge parameter contrasts. Therefore, it becomes necessary to eliminate the ambiguity of the problem. Such techniques are denoted with the term regularization.

There are two types of regularization mainly used for geophysical inverse problem. The first type involves approximate solutions to the basis equation or the corresponding normal equations. For instance, Krylov subspace methods have this characteristics, that smooth model components converge faster than non-smooth model parts (Hansen, 1992). In each iteration the Krylov subspace methods provide a approximated solution and project the original solution space into a subspace. Thus, they belong to indirect regularization. In contrast, this type of regularization can also be applied directly to control the model in an explicit way. An example is the applying of procedure like Singular Value Decomposition (SVD) for removing the singularity of the left hand side matrix in the normal equation (4.10). This type of regularization is beyond the scope of this of this work, the interested reader is referred to (Günther, 2004).

The second type of regularization attempts to constrain the model space with various geological and other geophysical information exist which would allow constructing a proper starting model. Applying constraints on the normal equations implies that the model must have certain characteristics. Possible constraints are:

1. The model update vector $\Delta\mathbf{m}$ must have a small norm, namely

$$\Phi_m = \|\Delta\mathbf{m}\|^2 \tag{4.12}$$

   This condition also ensures that the Taylor expansion is always valid for small values of $\Delta\mathbf{m}$.

2. The model is constraint so that the difference between two adjacent model parameters will be at its minimum. This can be achieved by using a matrix $\mathbf{R}$, which is a discrete representation of a gradient or higher order derivative operator.

$$\Phi_m = \|\mathbf{Rm}\|^2 \tag{4.13}$$

3. The model must consider a priori information in the form of model $\mathbf{m}_{apri}$

$$\Phi_m = \|\mathbf{m} - \mathbf{m}_{apri}\|^2 \tag{4.14}$$

   This condition ensures that the final model will be close to the a prior model.

where Φ_m represents the model penalty functional arising from model constraint.

The goal of inverse problem becomes minimizing the data penalty functional Φ_d and the model penalty functional Φ_m simultaneously. In this case, we can write a new penalty functional which considers the original minimization problem (4.6) and one of the previous constraints.

$$\Phi(\mathbf{m}) = \Phi_d(\mathbf{m}) + \lambda\Phi_m(\mathbf{m}) \tag{4.15}$$

where λ is the so called regularization or trade-off parameter. A suitable value of λ ensures that neither $\Phi_d(\mathbf{m})$ nor $\Phi_m(\mathbf{m})$ will preponderate in the penalty function $\Phi(\mathbf{m})$. Thus, an optimized value of λ must be sought. The relationship between $\Phi_d(\mathbf{m})$ and $\Phi_m(\mathbf{m})$ for various values of λ takes the form of an L-curve if we plot $\Phi_d(\mathbf{m})$ against $\Phi_m(\mathbf{m})$ in a log-log plot. Mathematically, this relationship between these two penalty functions can be described as follows: $\lambda \to 0$ implies that the data penalty functional is mainly minimized and the model penalty functional is barely considered; in contrast, $\lambda \to \infty$ provides the opposite situation. This indicates, the original minimization problem turns to minimization and optimization with regard to the regularization parameter (Meqbel, 2009).

4.1.3. The normal equation and its solution

Follow (4.15) the inverse problem can be solved in the sense of the Tikhonov regularization (Tikhonov and Arsenin, 1977), taking a regularized solution to be a model minimizing a penalty function, Φ, defined by

$$\Phi(\mathbf{m}) = (\mathbf{d} - \mathbf{f}(\mathbf{m}))^T \mathbf{C}_d^{-1} (\mathbf{d} - \mathbf{f}(\mathbf{m})) + \lambda (\mathbf{m} - \mathbf{m}_0)^T \mathbf{C}_m^{-1} (\mathbf{m} - \mathbf{m}_0) \tag{4.16}$$

where $\mathbf{C}_d^{-1} = \mathbf{D}^T\mathbf{D}$ and $\mathbf{C}_d$ is the data covariance matrix as used by Tarantola (1978) for the case of uncorrelated errors with standard deviations, $\mathbf{f}(\mathbf{m})$ defines the forward mapping, $\mathbf{m}_0$ is a prior or first guess model, λ is a regularization or trade-off parameter, $\mathbf{C}_m$ defines the model covariance or regularization term and $\mathbf{C}_m^{-1} = \mathbf{R}^T\mathbf{R}$, where $\mathbf{R}$ is a discrete representation of a gradient or higher order derivative operator.

Gauss-Newton iteration

Analogous to section 4.1.1 on page 46, the new penalty function (4.16) can be minimized through

$$(\nabla_m^2 \Phi(\mathbf{m})) \Delta\mathbf{m}_k = -\nabla_m \Phi(\mathbf{m}) \tag{4.17}$$

where $\nabla_m^2 \Phi(\mathbf{m})$ and $\nabla_m \Phi(\mathbf{m})$ represent the M-dimensional gradient vector $\mathbf{g}$ and $M \times M$ symmetric Hessian matrix $\mathbf{H}$, respectively.

Given equations (4.16-4.17), $\mathbf{g}(\mathbf{m})$ and $\mathbf{H}(\mathbf{m})$ can be computed as

$$\mathbf{g}(\mathbf{m}) = -2\mathbf{J}^T \mathbf{C}_d^{-1} (\mathbf{d} - \mathbf{f}(\mathbf{m})) + 2\lambda \mathbf{C}_m^{-1} \mathbf{m} \tag{4.18}$$

$$\mathbf{H}(\mathbf{m}) = 2\mathbf{J}^T \mathbf{C}_d^{-1} \mathbf{J} + 2\lambda \mathbf{C}_m^{-1} \tag{4.19}$$

if the second derivative of $\mathbf{f}(\mathbf{m})$ is significantly small and hence negligible.

Essentially, the Gauss-Newton iteration can be described as recursive minimization of $\Phi(\mathbf{m})$. To achieve this the normal equation (4.11) has to be solved within each iteration. If $\mathbf{r}$ describes the misfit between measured and predicted data, e.g. $\mathbf{r} = (\mathbf{d} - \mathbf{f}(\mathbf{m}))$, the normal equation and the model update $\Delta\mathbf{m} = \mathbf{m}_{k+1} - \mathbf{m}_k$ at the kth iteration can be formulated as

$$(\mathbf{J}^T \mathbf{C}_d^{-1} \mathbf{J} + \lambda \mathbf{C}_m^{-1}) \Delta\mathbf{m} = \mathbf{J}^T \mathbf{C}_d^{-1} \mathbf{r} - \lambda \mathbf{C}_m^{-1} \mathbf{m} \tag{4.20}$$

$$\text{and hence} \quad \Delta\mathbf{m} = (\mathbf{J}^T \mathbf{C}_d^{-1} \mathbf{J} + \lambda \mathbf{C}_m^{-1})^{-1} (\mathbf{J}^T \mathbf{C}_d^{-1} \mathbf{r} - \lambda \mathbf{C}_m^{-1} \mathbf{m}) \tag{4.21}$$

Levenberg-Marquardt iteration

One useful modification of the Gauss-Newton method is proposed by Levenberg (1944) and Marquardt (1963). Instead of equation (4.11) the normal equation is modified to the form:

$$(\mathbf{H}_k + \epsilon_k \mathbf{I})\Delta\mathbf{m}_k = -\mathbf{g}_k \tag{4.22}$$

where $\mathbf{I}$ is the identity matrix and ϵ_k is a positive damping parameter at kth iteration. This modification has the effect that the model update is damped at each iteration. The additional term $\epsilon\mathbf{I}$ restricts the length of the model update $\Delta\mathbf{m}_k$ to a certain length depending on the choice of ϵ_k, which is allowed to vary with iteration step. The goal of this task is to prevent the solution of the normal equation from divergence caused by the non-quadratic behavior of penalty functional Φ or poor conditioning of the approximated Hessian matrix $\mathbf{H}_k$. Since the functional to be minimized includes its own damping in the form of the stabilizing (last term in equation (4.16)), a large amount of Levenberg-Marquardt damping is not needed in our problem. Hence, the damping parameter ϵ is only needed to be quite small after the first few iteration steps (Rodi and Mackie, 2001). Hence, the modified normal equation can be written as

$$(\mathbf{J}^T\mathbf{C}_d^{-1}\mathbf{J} + \lambda\mathbf{C}_m^{-1} + \epsilon\mathbf{I})\Delta\mathbf{m} = \mathbf{J}^T\mathbf{C}_d^{-1}\mathbf{r} - \lambda\mathbf{C}_m^{-1}\mathbf{m} \tag{4.23}$$

and hence the model update can be obtained through

$$\Delta\mathbf{m} = (\mathbf{J}^T\mathbf{C}_d^{-1}\mathbf{J} + \lambda\mathbf{C}_m^{-1} + \epsilon\mathbf{I})^{-1}(\mathbf{J}^T\mathbf{C}_d^{-1}\mathbf{r} - \lambda\mathbf{C}_m^{-1}\mathbf{m}) \tag{4.24}$$

Solution of the normal equation

The normal equation presented above, i.e. equation (4.23), can be rewritten in a general matrix vector notation as:

$$\mathbf{A}\mathbf{x} = \mathbf{b} \tag{4.25}$$

where,

$$\mathbf{A} = \mathbf{H} + \epsilon\mathbf{I} = \mathbf{J}^T\mathbf{C}_d^{-1}\mathbf{J} + \lambda\mathbf{C}_m^{-1} + \epsilon\mathbf{I}, \quad \mathbf{b} = \mathbf{J}^T\mathbf{C}_d^{-1}\mathbf{r} - \lambda\mathbf{C}_m^{-1}\mathbf{m}, \quad \mathbf{x} = \Delta\mathbf{m} \tag{4.26}$$

Solving the normal equation is equivalent to solve a linear equation system with system coefficient matrix $\mathbf{A}$, right-hand side vector $\mathbf{b}$ and unknown vector $\mathbf{x}$. You will probably

familiar with this type of problem, because we have already faced the same challenge in the previous chapter (see section 3.1.3 on page 23).

The current linear equation system (eq. 4.25) differs from the one in previous chapter (eq. 3.25) in two ways. Firstly, the dimension of both equation system are different. While the dimension of the linear equation system for the forward problem is $(N_y-1)\times(2N_{ze}+N_{za}-2)$, if N_y is the number of horizontal grid steps, N_{ze} and N_{za} are the numbers of vertical grid steps within the conducting Earth and in the air layer, the dimension of the linear equation system for the inverse problem coincide with the number of model parameter, e.g. $M = N_y \times N_{ze}$. As we will see later, the number of model parameter will become $M = N_y \times N_{ze} \times 6$, if electrical anisotropy is considered in the model domain. But one thing is clear, that they all differ from the dimension of the linear equation system for the forward problem. Secondly, the system coefficient matrix $\mathbf{S}_m$ in equation (3.25) for the forward problem is a sparse, complex valued and symmetric banded matrix. It makes that either only non-zero valued entries or a half band of the matrix need to be stored. In contrast, the current system coefficient matrix **A** is also symmetric but in general a real valued, positive definite dense matrix.

The linear equation system (4.25) can be solved using either direct methods or iterative methods. Examples for the direct solves are the Cholesky and LU decompositions. The Cholesky method decomposes the matrix **A** in a triangular matrix **U**; and the LU decomposition decomposes **A** in two triangular matrices **L** and **U**. The resulting triangular matrices satisfy the following condition,

$$\mathbf{A} = \mathbf{U}^T\mathbf{U} \quad \text{and} \quad \mathbf{A} = \mathbf{LU}$$

By forward substitution,

$$\mathbf{U}^T\mathbf{y} = \mathbf{b} \quad \text{and} \quad \mathbf{Uy} = \mathbf{b}$$

and backward substitution,

$$\mathbf{Ux} = \mathbf{y} \quad \text{and} \quad \mathbf{Lx} = \mathbf{y}$$

a solution for vector **x** can be found (Meqbel, 2009). Direct methods are straightforward and easy to implement, but the system coefficient matrix has to be explicit formed and stored for each iteration. This is the most memory consuming part for the inverse problem if a direct method is used. The required memory will increase significantly for a finer discretization of model domain.

An example for iterative methods is the conjugate gradient method (CG). This technique was developed by Hestenes and Stiefel (1952). The underlying principle is to find a set of orthogonal, strictly speaking a set of **A**-orthogonal or conjugate, directions and to compute accompanying weights in a manner that every search direction is used only once. To solve the equation system (4.25), CG generates a sequence of approximated solutions by iterative minimization of the quadratic form:

$$\Phi(\mathbf{x}) = \frac{1}{2}\mathbf{x}^T\mathbf{A}\mathbf{x} - \mathbf{b}^T\mathbf{x} \tag{4.27}$$

along a sequence of conjugate search directions $\mathbf{d}$. Starting from $\mathbf{d} = \mathbf{b} - \mathbf{A}\mathbf{x}$ at $\mathbf{x} = 0$, the next search direction is obtained using:

$$\mathbf{d}_{k+1} = \mathbf{r}_k + \beta_{k+1}\mathbf{d}_k \tag{4.28}$$

where $\mathbf{r}_k$ is the gradient of eq. (4.27) at the solution $\mathbf{x}_k$ and given by:

$$\mathbf{r}_k = \frac{\partial}{\partial \mathbf{x}_k}(\frac{1}{2}\mathbf{x}_k^T\mathbf{A}\mathbf{x}_k - \mathbf{b}^T\mathbf{x}_k) = \mathbf{A}\mathbf{x}_k - \mathbf{b} \tag{4.29}$$

The scalar β_{k+1} in equation (4.28) ensures that the search direction $\mathbf{d}_{k+1}$ is conjugate, or **A**-orthogonal, to all previous search directions and can be calculated as:

$$\beta_{k+1} = \frac{\mathbf{r}_{k+1}^T\mathbf{r}_{k+1}}{\mathbf{r}_k^T\mathbf{r}_k} \tag{4.30}$$

The solution $\mathbf{x}_{k+1}$ which ensures that $\Phi(\mathbf{x})$ approaches its minimum is obtained by:

$$\mathbf{x}_{k+1} = \mathbf{x}_k + \alpha_k\mathbf{d}_k \tag{4.31}$$

where the scalar step size α_k is given by:

$$\alpha_k = \frac{\mathbf{r}_k^T\mathbf{r}_k}{\mathbf{d}_k^T\mathbf{A}\mathbf{d}_k} \tag{4.32}$$

A complete CG procedure is adopted from Shewchuk (n.d.) and presented in Algorithm 1, more details can be found in Golub and Van Loan (1996) and more others. In the CG scheme the main computation tasks are the matrix vector multiplications. Rodi and Mackie (2001) showed that this multiplication can be accomplished at the cost of two pseudo forward modeling computations.

The Conjugate Gradients method works well on matrices that are either well conditioned or have just a few distinct eigenvalues. Unfortunately, the system matrix $\mathbf{A}$ that we encountered in MT inversion problem is usually ill-conditioned and hence the use of the CG method could fail. Many studies have shown that it is necessary to use preconditioned CG method instead of plain CG method. The idea behind the use of a preconditioner is to compact the eigenvalue spread of the original system matrix because the smaller the eigenvalue spread, the more efficient the CG procedure (Hestenes and Stiefel, 1952).

Suppose that matrix $\mathbf{M}$ is symmetric, positive-definite and approximates $\mathbf{A}$, but is easy to invert. We can solve $\mathbf{Ax} = \mathbf{b}$ indirectly by solving

$$\mathbf{M}^{-1}\mathbf{Ax} = \mathbf{M}^{-1}\mathbf{b} \tag{4.33}$$

If the condition number of $\mathbf{M}^{-1}\mathbf{A}$ is smaller than it of $\mathbf{A}$, or if the eigenvalues of $\mathbf{M}^{-1}\mathbf{A}$ are better clustered than those of $\mathbf{A}$, we can iteratively solve equation (4.33) more quickly than the original problem. The matrix $\mathbf{M}$ is then called as a preconditioner. The best preconditioners are those which are most closely related to the actual system matrix $\mathbf{A}$ but are easy to invert. For example, if we used the actual system matrix as a preconditioner, the CG algorithm would reach the solution in just one step. This is because that particular preconditioner reduces the eigenvalue spread of the original system matrix to just one eigenvalue. This is clearly an exaggerated example because if we could inverse the actual system matrix, there would be no need to use CG any more. But this example demonstrates the idea behind the use of a preconditioner.

The effectiveness of a preconditioner $\mathbf{M}$ is determined by the condition number of $\mathbf{M}^{-1}\mathbf{A}$. So the problem remains of finding a preconditioner that approximates $\mathbf{A}$ well enough to improve convergence rate. With a good preconditioner, rapid convergence can often be obtained after only a few iterations. A pseudo code of preconditioned CG is also adopted from Shewchuk (n.d.) and presented in Algorithm 2.

4.2. Inversion of MT data with anisotropic conductivities

4.2.1. Concept of 2D anisotropic inversion

In this subsection, the essential elements for accomplishing of 2D anisotropic inversion are introduced. First of all, I will define the data vector **d** and the inversion parameter or model parameter **m**. Since the sensitivity matrix **J** is the most important quantity needed by all inversion or minimization algorithm (no matter it has to be explicit formed or not), the calculation of the **J** matrix is described in details. Finally, an appropriate penalty functional for anisotropic inversion problem and its minimization are also explained.

Data and inversion parameter

The data vector is the observed data **d** or predicted data $\mathbf{f}(\mathbf{m})$. It can be the apparent resistivity and phase, the impedance tensor, the rotation invariants of impedance tensor or the phase tensor. Within this thesis when I talk about data, it means uniquely the impedance tensor $\underline{\underline{\mathbf{Z}}}$. The data vector **d** can be expressed as

$$\mathbf{d} = (Z_{xx}, Z_{xy}, Z_{yx}, Z_{yy}) \tag{4.34}$$

for each receiver and each period.

The inversion parameter is the conductivity distribution in an anisotropic medium. It can be described by a symmetric positive definite 3×3 tensor. The tensor can be represented by three positive principal conductivities and three rotation angles by using of the Euler's rotations (see section 2.2.2). This representation is more descriptive than the fully occupied conductivity tensor. Once it is defined we know immediately how the electrical property is defined in a given Cartesian Coordinate System. Hence, the tensor representation with three principal conductivities and three rotation angels is used as the final inversion parameter. Additionally, the logarithms of all conductivities are used. It is useful for several reasons. First, it removes any bias associated with using conductivity as model parameters. Furthermore, it guarantees the positiveness of the model parameters (i.e. no negative conductivities are allowed). Finally, logarithmic parametrization allows for larger changes in the model parameters as the inversion is iterated. For the electrical problem, where the conductivity can vary by several orders of

magnitude in the Earth, this reduces the total number of iterations needed to reach an acceptable solution.

According to equation (2.36) an arbitrary symmetric and positive definite tensor $\underline{\underline{\sigma}}$ can be diagonalized and hence represented as three principal values (σ_1, σ_2, σ_3) and three rotation angels (α, β, γ). The final inversion parameter can be expressed as

$$\mathbf{m} = (\cdots, \underbrace{\ln \sigma_1^j, \ln \sigma_2^j, \ln \sigma_3^j, \alpha^j, \beta^j, \gamma^j}_{\text{for cell } j, \text{ where } j \in [1,\cdots,M]}, \cdots) \tag{4.35}$$

Global penalty functional

With a penalty functional we try to find a solution which can fit the data and also meet our expectation or existed information. An example of how the penalty functional can be stated is described in section 4.1 (see eq. 4.15). However, the balance between the data misfit and the model constraint could be destroyed because of the presence of anisotropic structure. For anisotropic case the number of model parameters will be six times more than it for the isotropic case with same discretization and number of the data. It gives the inversion more degrees of freedom which could lead that the inversion converges very slow or even do not converge at all. Hence, a penalizing of anisotropy is useful both to eliminate some of the ambiguity associated with inversion and to help the algorithm fall into a better local minimum. This can be done by introducing an additional term to the penalty functional, which attempts to make the three principal conductivities equal. The basic idea of this penalizing is quite simply and intuitive. If an isotropic model is adequate to explain the data, there is no need to introduce anisotropy at all. The anisotropy penalty functional for the entire model domain G is defined according to Pain et al. (2003),

$$\Phi_a(\mathbf{m}) = \int_G (\ln \sigma_1, \ln \sigma_2, \ln \sigma_3) \mathbf{K} \begin{pmatrix} \ln \sigma_1 \\ \ln \sigma_2 \\ \ln \sigma_3 \end{pmatrix} dG \tag{4.36}$$

The positive semi-definite matrix $\mathbf{K}$ has the form of a discretized Laplacian and its purpose is to make the principal conductivities equal. A typical form of $\mathbf{K}$ would therefore be

$$\mathbf{K} = \begin{pmatrix} 2 & -1 & -1 \\ -1 & 2 & -1 \\ -1 & -1 & 2 \end{pmatrix} \tag{4.37}$$

or more generally

$$\mathbf{K} = \begin{pmatrix} a_{12} + a_{13} & -a_{12} & -a_{13} \\ -a_{12} & a_{12} + a_{23} & -a_{23} \\ -a_{13} & -a_{23} & a_{13} + a_{23} \end{pmatrix} \tag{4.38}$$

where the three positive scalars in this matrix can be arbitrarily chosen so that the anisotropy is aligned with known physics.

Reorganize the matrix **K** in a proper order it can be applied to the full model parameter space according to equation (4.35). Equation (4.36) can hence be rewritten as:

$$\Phi_a(\mathbf{m}) = \mathbf{m}^T \mathbf{K} \mathbf{m} \tag{4.39}$$

For technical details about the reorganization the reader is referred to section A.5. Therefore, the penalty functional to be minimized is defined as

$$\Phi(\mathbf{m}) = \Phi_d(\mathbf{m}) + \lambda_s \Phi_m(\mathbf{m}) + \lambda_a \Phi_a(\mathbf{m}) \tag{4.40}$$

where the first and the second terms at the right hand side are the data misfit and the model constraint as described in section 4.1, λ_s and λ_a are regularization parameters of the model structure (also known as model roughness penalty parameter) and anisotropy penalty parameter, respectively.

Least-squares inversion

Given equation (4.40), the model update can be obtained by using the Levenberg-Marquardt method with step length damping

$$\Delta \mathbf{m} = (\mathbf{J}^T \mathbf{C}_d^{-1} \mathbf{J} + \lambda_s \mathbf{C}_m^{-1} + \lambda_a \mathbf{K} + \epsilon \mathbf{I})^{-1} (\mathbf{J}^T \mathbf{C}_d^{-1} \mathbf{r} - \lambda_s \mathbf{C}_m^{-1} \mathbf{m} - \lambda_a \mathbf{K} \mathbf{m}) \tag{4.41}$$

where **J**, $\mathbf{C}_d$, $\mathbf{C}_m$, **K** and **I** are the $N \times M$ sensitivity matrix, the $N \times N$ data covariance matrix , the $M \times M$ model covariance matrix, the $M \times M$ matrix for anisotropic constraint and the $M \times M$ identity matrix, respectively; **r** and **m** are the data residual vector and the model parameter vector; λ_s and ϵ are the trade-off parameter for model structure and the Levenberg-Marquardt step damping parameter; λ_a can be either a scalar value or a spatial function. The selection of λ_a depends on our expectation or how well the presence of Anisotropy is known.

4.2.2. Sensitivity matrix computation

The explicit expression of the **J** is required to formulate the model update (see equation 4.41). In this section I will discuss how the sensitivity matrix is calculated.

As the name suggests, the sensitivity matrix **J** describes how sensitive the predicted data are towards small changes in the model parameters. It is defined as the first derivative of predicted data $\mathbf{f}(\mathbf{m})$ with respect to model parameter **m**. Consider a set of predicted data with N elements which is calculated based on a 2D model discretized with M grid cells, the matrix **J** is of dimension $N \times M$ and can be expressed as

$$\mathbf{J} = \begin{pmatrix} \frac{\partial f_1(m)}{\partial m_1} & \frac{\partial f_1(m)}{\partial m_2} & \cdots & \frac{\partial f_1(m)}{\partial m_M} \\ \frac{\partial f_2(m)}{\partial m_1} & \ddots & & \vdots \\ \vdots & & \ddots & \vdots \\ \frac{\partial f_N(m)}{\partial m_1} & \cdots & \cdots & \frac{\partial f_N(m)}{\partial m_M} \end{pmatrix} \tag{4.42}$$

The definition of the sensitivity matrix suggests that the computation of each element of **J** can be done in a straightforward manner: simply perturbing each model parameter by $\Delta\mathbf{m}$, solving the forward modeling problem for $\mathbf{m} + \Delta\mathbf{m}$ and approximating the first derivative with a forward difference.

$$\frac{\partial f_1(m_k)}{\partial m_k} = \frac{f_l(m_k + \Delta m) - f_l(m_k)}{\Delta m} \quad l = 1, \cdots, N \quad \text{and} \quad k = 1, \cdots, M \tag{4.43}$$

This approach implies that the same step must be repeated for all model parameters, which means the forward problem has to be solved M times to get all elements of **J**. This is for multidimensional problem with a fine discretization a tedious and very time-consuming task. Rodi (1976) and later Rodi and Mackie (2001) suggested an efficient method to compute all elements of **J** with only solving the forward problem N times. This method is based on the reciprocity principle, which states that the model response of a receiver at location j depending on a transmitter located at the location i is the same as that of a transmitter located at the location j and a receiver at i.

Recently, Egbert and Kelbert (2012) presented a general approach to derive generic expression for computing the elements of the sensitivity matrix in 2D and 3D. I will summarize the basic idea of this approach as following. First, the forward modeling operator can be considered as a function depending on the model parameters and the primary field components, which is the solution of the forward problem and also depending on the model parameters.

$$\mathbf{f}(\mathbf{m}) = \psi(\mathbf{e}(\mathbf{m}), \mathbf{m}) \tag{4.44}$$

Equation (4.44) states the fact that the model responses are derived from the forward solution (the EM primary fields) **e**. The function ψ can be considered as a function that extracts (via interpolation and other mathematical basic functions) the corresponding values of electric and magnetic fields at the observation location to evaluate the model responses. The definition of **J** can be rewritten as

$$\mathbf{J} = \frac{\partial \mathbf{f}(\mathbf{m})}{\partial \mathbf{m}} = \frac{\partial \psi(\mathbf{e}(\mathbf{m}), \mathbf{m})}{\partial \mathbf{m}} = \frac{\partial \psi}{\partial \mathbf{e}} \frac{\partial \mathbf{e}}{\partial \mathbf{m}} + \frac{\partial \psi}{\partial \mathbf{m}} \tag{4.45}$$

Using matrix notation to equation (4.45) yields

$$\mathbf{J} = \mathbf{L}\mathbf{F} + \mathbf{Q} \tag{4.46}$$

where

$$\mathbf{L} = \frac{\partial \psi}{\partial \mathbf{e}}, \quad \mathbf{F} = \frac{\partial \mathbf{e}}{\mathbf{m}}, \quad \mathbf{Q} = \frac{\partial \psi}{\partial \mathbf{m}}$$

The matrix **L** represents the linearized data functional, through which the perturbation in data, caused by the perturbation in the EM primary fields (the forward solution), is computed. The matrix **Q** represents the dependency of function ψ on the model parameter **m** if the primary fields are treated as constant and hence independent of **m**. Matrices **L** and **Q** are in general sparse, because they only depend on a few nodes surrounding the corresponding MT station, and for some case **Q** can be zero. Hence, these two matrices can be efficiently computed. In contrast, computing the elements of **F** is the most challenging task involved in equation (4.46).

To derive a general expression for **F**, first differentiating equation (3.25) with respect to the model parameters **m** yields

$$\frac{\partial (\mathbf{S}_m \mathbf{e})}{\partial \mathbf{m}} = \frac{\partial \mathbf{b}}{\partial \mathbf{m}} \tag{4.47}$$

Assume that **b** is constant, independent of **m**, although some subtle issues related to this point may arise with specific solution approaches (see Egbert and Kelbert (2012) and also Newman and Boggs (2004)). Then, letting **e** be the solution of (3.25) at **m**, and noting that forward solution **e** varies as model parameter **m** is varied, we obtain

$$\frac{\partial (\mathbf{S}_m \mathbf{e})}{\partial \mathbf{m}} = \left[\frac{\partial \mathbf{S}_m}{\partial \mathbf{m}} \mathbf{e} + \mathbf{S}_m \frac{\partial \mathbf{e}}{\partial \mathbf{m}} \right] = \frac{\partial \mathbf{b}}{\partial \mathbf{m}} = 0 \tag{4.48}$$

and

$$\mathbf{S}_m \left(\frac{\partial \mathbf{e}}{\partial \mathbf{m}} \right) = -\frac{\partial \mathbf{S}_m}{\partial \mathbf{m}} \mathbf{e} \quad \Rightarrow \quad \mathbf{S}_m \mathbf{F} = \mathbf{P} \tag{4.49}$$

Hence, **F** can be expressed as

$$\mathbf{F} = \mathbf{S}_m^{-1}\mathbf{P} \quad \text{where} \quad \mathbf{P} = -\frac{\partial \mathbf{S}_m}{\partial \mathbf{m}}\mathbf{e} \tag{4.50}$$

The operator **P** depends on details of both the numerical model implementation and the model parameter. It represents a mapping of forward solution defined on the grid nodes onto the grid cells where the discretized model parameters are defined. Finally, we obtain an expression for the numerical sensitivity matrix for general EM problems

$$\mathbf{J} = \mathbf{L}\mathbf{S}_m^{-1}\mathbf{P} + \mathbf{Q} \tag{4.51}$$

In order to derive the sensitivity matrix, we need the predicted data (e.g. the impedance tensor), where two orthogonal source polarizations are required. Following the discussion in section 3.1.4 and Mackie and Madden (1993a) and Newman and Alumbaugh (2000), the electric and magnetic fields for the two polarizations can be denoted by E_{x1}, E_{y1}, H_{x1}, H_{y1} and E_{x2}, E_{y2}, H_{x2}, H_{y2}, which are collected through the impedance tensor $\underline{\underline{\mathbf{Z}}}$ with

$$\mathbf{E} = \underline{\underline{\mathbf{Z}}}\mathbf{H} \tag{4.52}$$

and in its explicit matrix notation

$$\underline{\underline{\mathbf{Z}}} = \begin{pmatrix} Z_{xx} & Z_{xy} \\ Z_{yx} & Z_{yy} \end{pmatrix} = \begin{pmatrix} E_{x1} & E_{x2} \\ E_{y1} & E_{y2} \end{pmatrix} \cdot \begin{pmatrix} H_{x1} & H_{x2} \\ H_{y1} & H_{y2} \end{pmatrix}^{-1} \tag{4.53}$$

It is obvious, the i-th row of sensitivity matrix **J** can be obtained through

$$\mathbf{J}_i = \frac{\partial \mathbf{f}_i(\mathbf{m})}{\partial \mathbf{m}} = \frac{\partial \psi(\mathbf{e}_i(\mathbf{m}), \mathbf{m})}{\partial \mathbf{m}} = \frac{\partial Z_{p,q}}{\partial \mathbf{m}} \tag{4.54}$$

where $Z_{p,q}$ denotes an arbitrary element of impedance tensor $\underline{\underline{\mathbf{Z}}}$. Repeating this for all periods and all MT receivers we obtain the full **J** matrix. The problem becomes how to calculate the first derivative of $Z_{p,q}$ with respect to model parameter **m**.

The particular expression of impedance tensor elements is introduced in section 3.1.4. In the following, I will use the yx-component of the impedance tensor as an example to explain how its first derivative is calculated. First, I adopt the general expression of Z_{xy} from equation (3.30):

$$Z_{yx} = \frac{E_{y1}H_{y2} - E_{y2}H_{y1}}{H_{x1}H_{y2} - H_{x2}H_{y1}}$$

Taking first derivative of Z_{yx} with respect to $\mathbf{m}$ yields

$$\begin{aligned}\frac{\partial Z_{yx}}{\partial \mathbf{m}} &= \frac{1}{\det \mathbf{H}}\left(E_{y1}\frac{\partial H_{y2}}{\partial \mathbf{m}} + H_{y2}\frac{\partial E_{y1}}{\partial \mathbf{m}} - E_{y2}\frac{\partial H_{y1}}{\partial \mathbf{m}} - H_{y1}\frac{\partial E_{y2}}{\partial \mathbf{m}}\right) - \cdots \\ &\quad - \frac{E_{y1}H_{y2} - E_{y2}H_{y1}}{\det \mathbf{H}^2}\left(H_{x1}\frac{\partial H_{y2}}{\partial \mathbf{m}} + H_{y2}\frac{\partial H_{x1}}{\partial \mathbf{m}} - \cdots \right. \\ &\quad \left. - H_{x2}\frac{\partial H_{y1}}{\partial \mathbf{m}} - H_{y1}\frac{\partial H_{x2}}{\partial \mathbf{m}}\right) \end{aligned} \tag{4.55}$$

where $\det \mathbf{H} = H_{x1}H_{y2} - H_{x2}H_{y1}$.

One can easily observe that the right hand side of equation (4.55) depends on all four components of the magnetic field and two y-components of electric field. Furthermore, the calculation of $\partial Z_{yx}/\partial \mathbf{m}$ involves partial derivatives of the electric and magnetic fields. These derivatives can be related to the forward solutions, e.g.

$$\frac{\partial H_{xj}}{\partial m_k} = \frac{\partial}{\partial m_k}\left({}^{h}g_x^T \mathbf{e}_j\right) \tag{4.56}$$

$$\frac{\partial H_{yj}}{\partial m_k} = \frac{\partial}{\partial m_k}\left({}^{h}g_y^T \mathbf{e}_j\right) \tag{4.57}$$

$$\frac{\partial E_{yj}}{\partial m_k} = \frac{\partial}{\partial m_k}\left({}^{e}g_y^T \mathbf{e}_j\right) \tag{4.58}$$

where $j \in (1, 2)$ denotes the two different polarisations, m_k is the k-th element of model parameter $\mathbf{m}$, $\mathbf{e}_j$ is the primary fields (the forward solution, see eq. 2.30) of the j-th polarisation. ${}^{h}g_x^T$ represents an operator through which the x-component of the magnetic field at receiver location is derived based on known primary fields and analogously, ${}^{e}g_y^T$ is the operator through which the y-component of the electrical field at receiver location is derived based on known primary fields, the superscript in these expression denotes the matrix transpose. This kind of operator is usually a combination of two processes, if it is related to secondary field components like H_y, H_z, E_y and E_z. The first process is the derivation of secondary field components on the mesh grid from known primary field components and the second process is the interpolation of the obtained secondary field components from the first process to receiver location. If this operator is related to primary field components E_x and H_x, the first process is not needed and only the second process remains. As already discussed in section 3.1.4, the interpolation process is independent of discretized conductivities (the model parameters), since the bi-linear interpolation technique is used in this work. The derivation of H_y and H_z rely on equation (3.4) and (3.5) which are also independent of the model parameters. In contrast, the derivation of E_y and E_z are defined by equations (3.18)

and (3.19) and the accumulative conductivities are involved in the calculation, which means that within current example only the operator ${}^{e}g_{yj}^{T}$ depends on model parameter $\mathbf{m}$.

According to equations (4.45), (4.46) and (4.50), equations (4.56) to (4.58) can be rewritten as

$$\frac{\partial H_{xj}}{\partial m_k} = -{}^{h}g_x^T \mathbf{S}_m^{-1} \frac{\partial \mathbf{S}_m}{\partial m_k} \mathbf{e}_j \tag{4.59}$$

$$\frac{\partial H_{yj}}{\partial m_k} = -{}^{h}g_y^T \mathbf{S}_m^{-1} \frac{\partial \mathbf{S}_m}{\partial m_k} \mathbf{e}_j \tag{4.60}$$

$$\frac{\partial E_{yj}}{\partial m_k} = \left(\frac{\partial}{\partial m_k} \left({}^{e}g_y^T \right) - {}^{e}g_y^T \mathbf{S}_m^{-1} \frac{\partial \mathbf{S}_m}{\partial m_k} \right) \mathbf{e}_j \tag{4.61}$$

Using the above results, terms involving the electric and magnetic field partial derivatives can be substituted in equation (4.59). After some algebra, a general expression for the sensitivity elements related to the yx-component of the impedance tensor is obtained

$$\begin{aligned} \frac{\partial Z_{yx}}{\partial \mathbf{m}} = & \left[\frac{H_{y1}}{\det \mathbf{H}} {}^{e}g_y^T + \left(\frac{H_{x1}R}{\det \mathbf{H}^2} - \frac{E_{y1}}{\det \mathbf{H}} \right) {}^{h}g_y^T - \frac{H_{y1}R}{\det \mathbf{H}^2} {}^{h}g_x^T \right] \mathbf{S}_m^{-1} \frac{\partial \mathbf{S}_m}{\partial \mathbf{m}} \mathbf{e}_1 \\ & + \left[-\frac{H_{y2}}{\det \mathbf{H}} {}^{e}g_y^T + \left(\frac{E_{y2}}{\det \mathbf{H}} - \frac{H_{x2}R}{\det \mathbf{H}^2} \right) {}^{h}g_y^T + \frac{H_{y2}R}{\det \mathbf{H}^2} {}^{h}g_x^T \right] \mathbf{S}_m^{-1} \frac{\partial \mathbf{S}_m}{\partial \mathbf{m}} \mathbf{e}_2 \\ & - \frac{H_{y1}}{\det \mathbf{H}} \frac{\partial}{\partial \mathbf{m}} ({}^{e}g_y^T) \mathbf{e}_1 + \frac{H_{y2}}{\det \mathbf{H}} \frac{\partial}{\partial \mathbf{m}} ({}^{e}g_y^T) \mathbf{e}_2 \end{aligned} \tag{4.62}$$

where $R = E_{y1}H_{y2} - E_{y2}H_{y1}$ and $\det \mathbf{H} = H_{x1}H_{y2} - H_{x2}H_{y1}$. $\mathbf{e}_1$ and $\mathbf{e}_2$ are the forward solutions related to two orthogonal source polarizations.

Following equations (4.50) and (4.51), we can summarize equation (4.62) to a more generic form

$$\frac{\partial Z_{yx}}{\partial \mathbf{m}} = (\mathbf{L}_1 \mathbf{S}_m^{-1} \mathbf{P}_1 + \mathbf{Q}_1) + (\mathbf{L}_2 \mathbf{S}_m^{-1} \mathbf{P}_2 + \mathbf{Q}_2) \tag{4.63}$$

where

$$\begin{aligned} \mathbf{L}_1 &= \frac{H_{y1}}{\det \mathbf{H}} {}^{e}g_y^T + \left(\frac{H_{x1}R}{\det \mathbf{H}^2} - \frac{E_{y1}}{\det \mathbf{H}} \right) {}^{h}g_y^T - \frac{H_{y1}R}{\det \mathbf{H}^2} {}^{h}g_x^T \\ \mathbf{P}_1 &= \frac{\partial \mathbf{S}_m}{\partial \mathbf{m}} \mathbf{e}_1 \quad \text{and} \quad \mathbf{Q}_1 = -\frac{H_{y1}}{\det \mathbf{H}} \frac{\partial}{\partial \mathbf{m}} ({}^{e}g_y^T) \mathbf{e}_1 \\ \mathbf{L}_2 &= -\frac{H_{y2}}{\det \mathbf{H}} {}^{e}g_y^T + \left(\frac{E_{y2}}{\det \mathbf{H}} - \frac{H_{x2}R}{\det \mathbf{H}^2} \right) {}^{h}g_y^T + \frac{H_{y2}R}{\det \mathbf{H}^2} {}^{h}g_x^T \\ \mathbf{P}_2 &= \frac{\partial \mathbf{S}_m}{\partial \mathbf{m}} \mathbf{e}_2 \quad \text{and} \quad \mathbf{Q}_2 = \frac{H_{y2}}{\det \mathbf{H}} \frac{\partial}{\partial \mathbf{m}} ({}^{e}g_y^T) \mathbf{e}_2 \end{aligned}$$

hold for the current example.

Equation (4.63) holds generally for all the sensitivity computation related to impedance tensor elements. The expression of **L**, **P** and **Q** may different for other impedance tensor element. For instance, the first derivative of Z_{xy} with respect to model parameter **m**. Since E_y and E_z are not involved in the calculation of Z_{xy}, **Q** will become zero. The expression of **L** will also vary accordingly and only the expression of **P** will remain unchanged. For 2D anisotropic case, as already discussed in section 3.1.4, the H_{x2} component will vanish. Thus, the expression of **L**, **P** and **Q** will be further simplified.

4.3. Two-dimensional inversion studies

After the previously introduced inversion strategy is implemented into a set of computer code, it is necessary to check its capabilities and show its limitations. In this section I present results from synthetically generated two-dimensional inversion problems. A common test model is used for different inversion purposes. The model consists of a two-dimensional single conductive and rectangular body embedded in a $100\,\Omega\mathrm{m}$ homogeneous, isotropic background. The entire Earth model has dimensions of 260×100 km and the model parametrization for inversion divides the Earth model into a grid of blocks numbering 30 in the horizontal y-direction and 20 in the vertical z-direction, implying a total mesh grid cells of 600 (left panel of Fig. 4.1). Within an anisotropic inversion algorithm 6 parameters are considered for every single mesh grid cell, therefore, in total 3600 model parameters are considered for each inversion test. The anomalous body has dimensions of $2 \times 12\,\mathrm{km}$ and its top is $800\,\mathrm{m}$ below the Earth's surface (right panel of Fig. 4.1).

Obviously, such a big model as displayed in left panel of figure 4.1 is not appropriate for demonstration of the inversion results, since the interested area is considerably smaller than the entire model domain. But, if only an enlarged drawing of the interested area is displayed, like the view in the right panel of figure 4.1, the changes in model space outside this selected area will be invisible. Of course, those kind of changes outside of the interested area are not our main focus, but for test purpose, it is worth to know how the model update varies in the entire model domain. Thus, a proper way to demonstrate the results is needed, so that the changes of model parameter in the entire model domain should fairly distinguishable. One way to achieve this is ignoring the real information about horizontal distance and depth, and displaying the model with uniform grid cells (fig. 4.2).

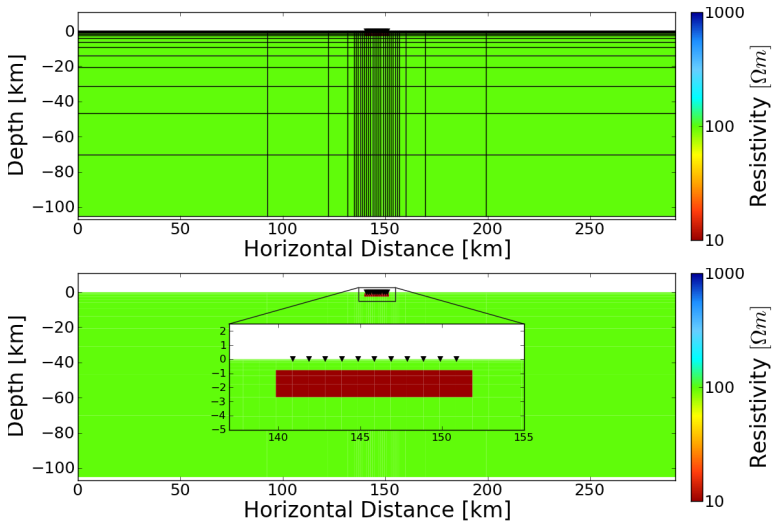

Figure 4.1.: The simple test model consists of a conductive and rectangular block, where its electrical property varies for the following tests, embedded in a homogeneous isotropic half-space with resistivity of $\rho_1 = 100\,\Omega\mathrm{m}$. The model is discretized using rectangular mesh grid (upper panel). The black triangles denote MT sites located above the conductive square block (see the enlarged part in the lower panel).

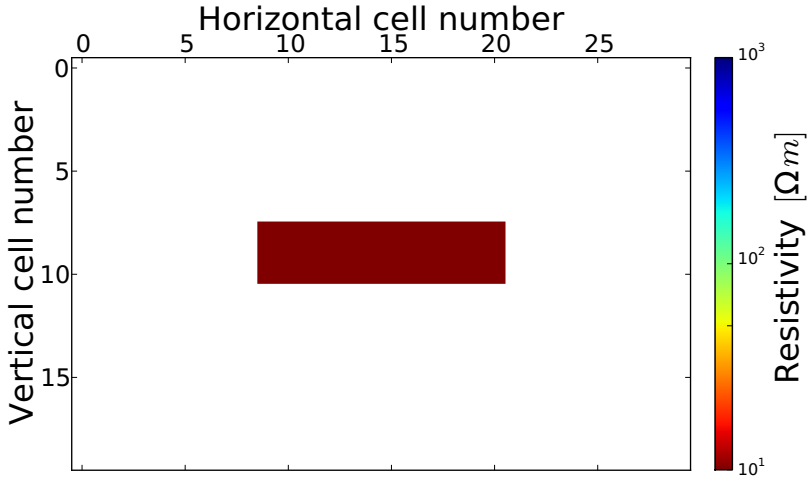

Figure 4.2.: The same model as displayed in figure 4.1. The real information about horizontal distance and depth are ignored and the model is displayed with uniform rectangular grid.

In order to demonstrate the reconstructed material properties in the model is whether electrical anisotropic or not, one would need to display at least the three principal resistivity values separately. However, it is not enough to show the degrees of anisotropy in the studied model. Furthermore, distinguishing difference between color coded plots could be a tough task, if the color code extends in a wide range. One way to accomplish this is to display a section of percentage anisotropy. For this purpose I define the percentage anisotropy as the ratio of the current anisotropy to the maximal allowed anisotropy. As we already known from previous sections, with a given resistivity tensor the current anisotropy can be defined as

$$\text{current anisotropy} = (\rho_1, \rho_2, \rho_3) \begin{pmatrix} 2 & -1 & -1 \\ -1 & 2 & -1 \\ -1 & -1 & 2 \end{pmatrix} \begin{pmatrix} \rho_1 \\ \rho_2 \\ \rho_3 \end{pmatrix} \tag{4.64}$$

and similarly, the maximal anisotropy is defined as

$$\text{maximal anisotropy} = (\rho_{max}, \rho_{min}, \rho_{min}) \begin{pmatrix} 2 & -1 & -1 \\ -1 & 2 & -1 \\ -1 & -1 & 2 \end{pmatrix} \begin{pmatrix} \rho_{max} \\ \rho_{min} \\ \rho_{min} \end{pmatrix} \tag{4.65}$$

where ρ_{max} is the maximal value of the given resistivity tensor, e.g. $\rho_{max} = max(\rho_1, \rho_2, \rho_3)$ and ρ_{min} is defined as the minimal allowed resistivity of the Earth materials. Here I choose ρ_{min} to be $0.3\,\Omega\mathrm{m}$, e.g. a value close to the resistivity of sea water. Hence, the percentage anisotropy is

$$\text{percentage anisotropy} = \frac{\text{current anisotropy}}{\text{maximal anisotropy}} \tag{4.66}$$

For all the following inversion tests, the starting model was a uniform half-space with resistivity of $100\,\Omega\mathrm{m}$. The stopping criteria is chosen as either the root mean square misfit (RMS) falls below 1.05 or 25 iterations are finished. The RMS misfit is defined as

$$\text{RMS} = \sqrt{\frac{\sum_{i=1}^{N_d} \left| \frac{d_i - f_i(\mathbf{m})}{e_i} \right|^2}{N_d}} \tag{4.67}$$

4.3.1. Influence of structural and anisotropy penalty parameters on inversion model

Since two penalty parameters are used in the penalty functional , e.g. equation (4.40) to balance between data misfit, model roughness and the electrical anisotropy, one should first

examine their influences on inversion algorithm. In general, the model roughness penalty parameter λ_s and the anisotropy penalty parameter λ_a are both scalar values and act as scaling factors, for instance, When λ_s is large, the model roughness term is emphasized and which leads to a smoother model and if λ_a is large, the term of anisotropy constraint is emphasized and which will lead to a model with less anisotropy. In general, it is to expect that the data fit improves as the magnitudes of λ_s and λ_a are decreased, the model roughness constraint and the anisotropy constraint become relatively less important in the penalty functional. However, using values that are too small will result in over-fitting of the data and one may obtain much more equivalent models which are fit the data equally well but far away from our expectation or known information. The purpose of applying those constraints is attempting to turn the otherwise ill-posed problem into an over-determined system of equations that can be solved in a least-squares sense, the nature of the model roughness penalty determines the appearance of the resolved model and the nature of the anisotropy penalty ensures that the material properties will stay isotropic, if the data can be fit in that way, which corresponds the sense of "simple" model. There are numerous ways to estimate appropriate levels of penalty parameters. Most of these methods require knowledge of data error and usually assume uncorrelated Gaussian data-error statistics (Hansen, 1998). In practice, the optimal penalty parameters can only be obtained by doing careful examination of a suite of solutions calculated using a range of penalty levels (Pratt and Chapman (1992); and Pain et al. (2003)).

In a first test the conductive rectangular body is defined anisotropic with resistivity of $\rho_x, \rho_y, \rho_z = 50, 10, 50\,\Omega\mathrm{m}$ and the rotation angles are all zero, which implies that the principal axes of anisotropy coincide with the coordinate axes of the measurement. The background of this anomalous conductive body is a homogeneous, isotropic half-space with resistivity of $100\,\Omega\mathrm{m}$. The xy- and yx-components of the impedance tensor at eleven sites and ten frequencies generated from this model are used for inversion as "observed" data, which yields a total number of 440 real-valued data. The frequencies range from 0.01 to 1000 Hz and are evenly spaced on a logarithmic scale.

To examine the influences of penalty parameters on inversion, I vary the model roughness penalty parameter λ_s and the anisotropy penalty parameter λ_a in a very wide range from 10^9 to 10^{-9}, with a decreasing factor of 0.1 for each step if the parameters are between 10^3 and 10^{-3}, and with decreasing factor or 0.01 for each step if the parameters are belong to interval $[10^9, 10^3]$ and interval $[10^{-3}, 10^{-9}]$. It leads to a total number of 169 different inversion runs. For each inversion run the penalty level (e.g. the value of λ_a and λ_s) are fixed. All tests are performed with a maximum allowed number of iterations of 25 and the start

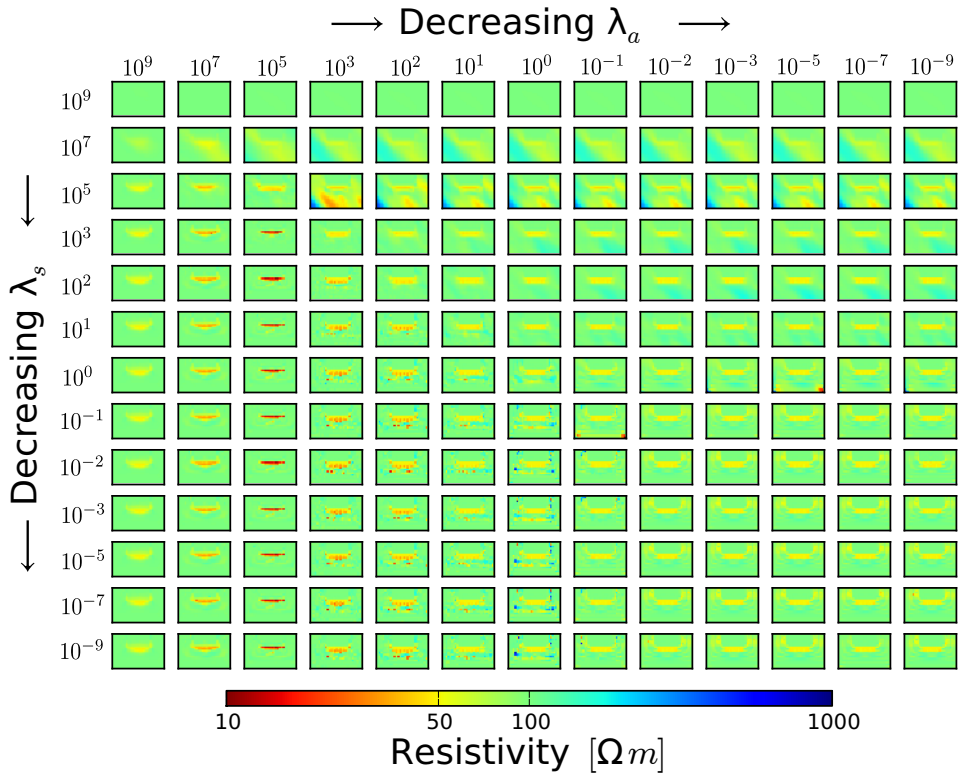

Figure 4.3.: Inversion results for the first test model. The ρ_x component of 169 inversion runs are displayed as image arrays and each rectangular represents the result of a single inversion run with fixed regularization parameters. While regularization parameter λ_s decreases (from top to bottom), the resulting model is getting raugher and raugher. Similarly, while regularization parameter λ_a decreases (from left to right), the resolved anomaly is approching its real value.

guess (the initial model) is a homogeneous isotropic half-space with resistivity of $100\,\Omega\mathrm{m}$. The maximal number of CG iteration inside each inversion iteration is set to 50 and the CG iteration will also terminated if the norm of the residual falls below 1.0×10^{-5}. The Levenberg-Marquardt damping factor is set to 0.001 times the current value of the objective function, e.g. $\epsilon_l = 0.001\Phi(\mathbf{m}_l)$.

The inversion results are shown in figures 4.3 to 4.7. Each figure displays one particular inversion results for all 169 inversion runs, inversion result obtained using fixed penalty level of $\lambda_s = 10^9$ and $\lambda_a = 10^9$ is displayed at the upper left panel and the one using fixed penalty level of $\lambda_s = 10^{-9}$ and $\lambda_a = 10^{-9}$ is displayed at the lower right panel of each figure. The

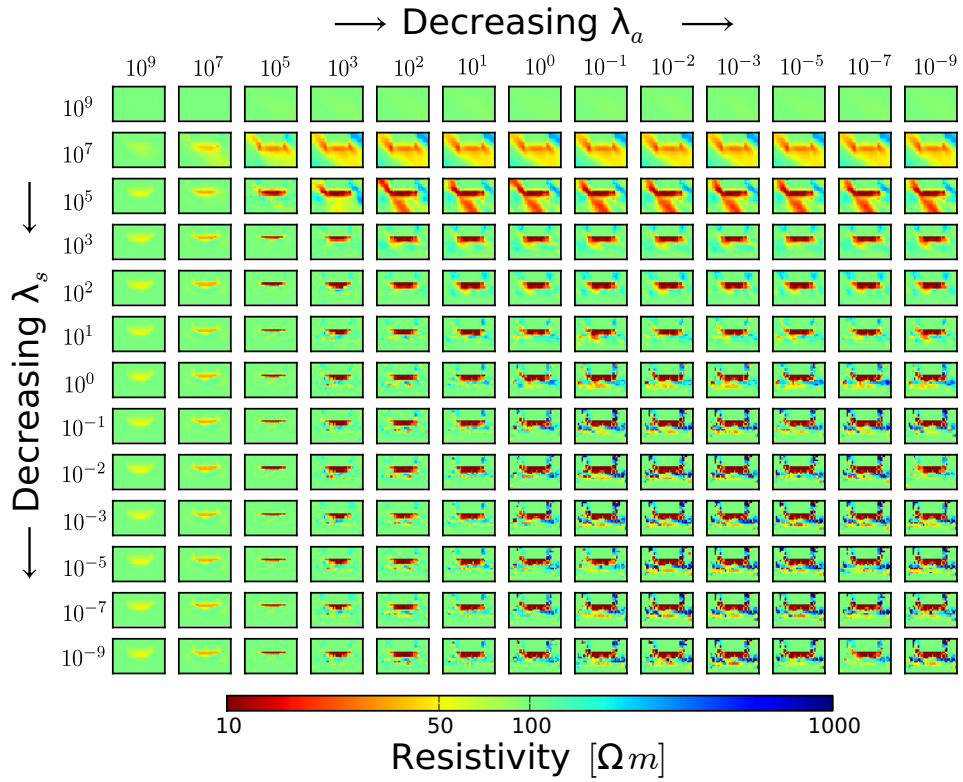

Figure 4.4.: Inversion results for the first test model. The ρ_y component of 169 inversion runs are displayed as image arrays and each rectangular represents the result of a single inversion run with fixed regularization parameters. While regularization parameter λ_s decreases (from top to bottom), the resulting model is getting raugher and raugher. Similarly, while regularization parameter λ_a decreases (from left to right), the resolved anomaly is approching its real value.

resolved principal resistivity values ρ_x, ρ_y and ρ_z are displayed in figures 4.3, 4.4 and 4.5, respectively. Figure 4.6 summarizes the percentage anisotropy according to equations (4.64) to (4.67) and figure 4.7 displays the over-all Root Mean Square (RMS) error.

Compare figures 4.3, 4.4 and 4.5, the inversion models clearly show the effectiveness of using appropriate penalty levels. Models resulting from large roughness penalties stay smooth (top row of images in the three figures) and models resulting from large anisotropy penalties stay isotropic (the first three columns of images in the figures, and more clear in figure 4.6). As the roughness penalty decreases (from the top row to the bottom row), the expected structure is successively developed. For this particular test, the inversion models will stay isotropic, if λ_s

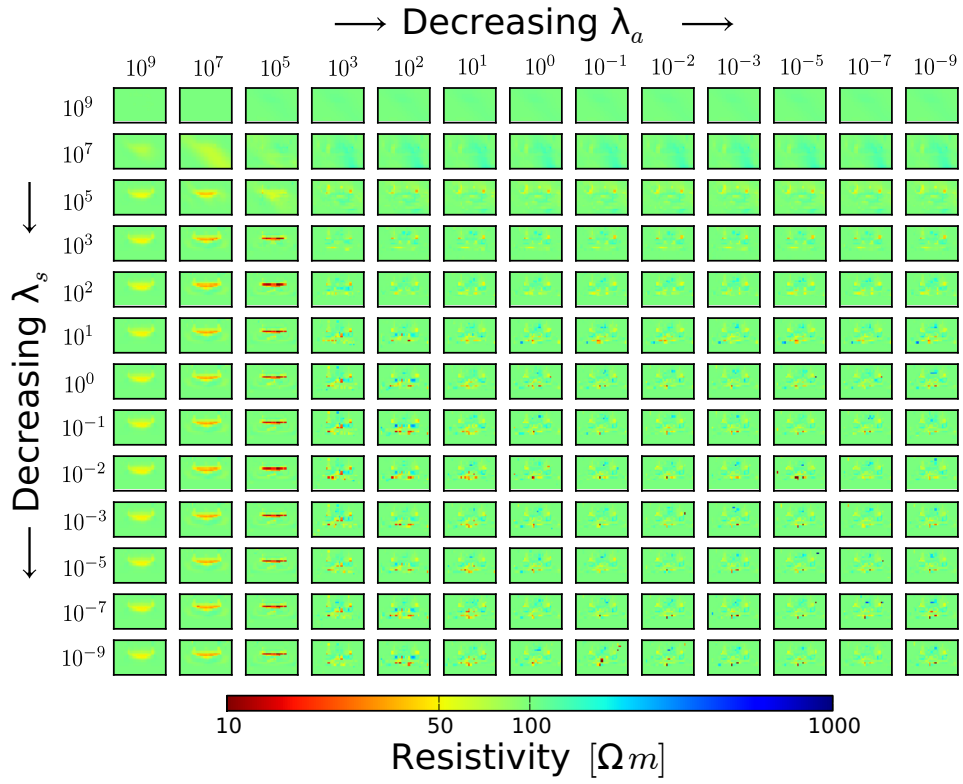

Figure 4.5.: Inversion results for the first test model. The ρ_z component of 169 inversion runs are displayed as image arrays and each rectangular represents the result of a single inversion run with fixed regularization parameters. While regularization parameter λ_a is higher than 10^5, the resulting model exhibits a great similarity with the true model. Otherwise, no cognizable anomaly is resolved in ρ_z component for known reasons explained in 3.2.1.

is below 10^5 and λ_a is bigger than 10^3 (see figure 4.6). In a range of $\lambda_s > 10^3$, no cognizable structure can be created due to very large roughness penalty parameter. If λ_s and λ_a are both smaller than 10^3, the anisotropic anomalous body is successively resolved. However, artificial structure will be also created if λ_s and λ_a are both smaller than 10, which indicates a possible transition to over-fitting. This phenomenon can be observed even more clear through figure 4.6. As we may observe, in the range of λ_s and λ_a smaller than 10^3 and ignoring artificial structure caused by very small penalty levels, the ρ_x and ρ_y components are well resolved and resistivity values approximated to the known true value of $50\,\Omega\mathrm{m}$ and $10\,\Omega\mathrm{m}$ can be obtained from almost all the inversion runs. The shape of the anomalous conductive body is also fully resolved in the both components. In contrast, no cognizable conductive anomaly is resolved in the ρ_z component. This is actually not a surprise. As already discussed in section

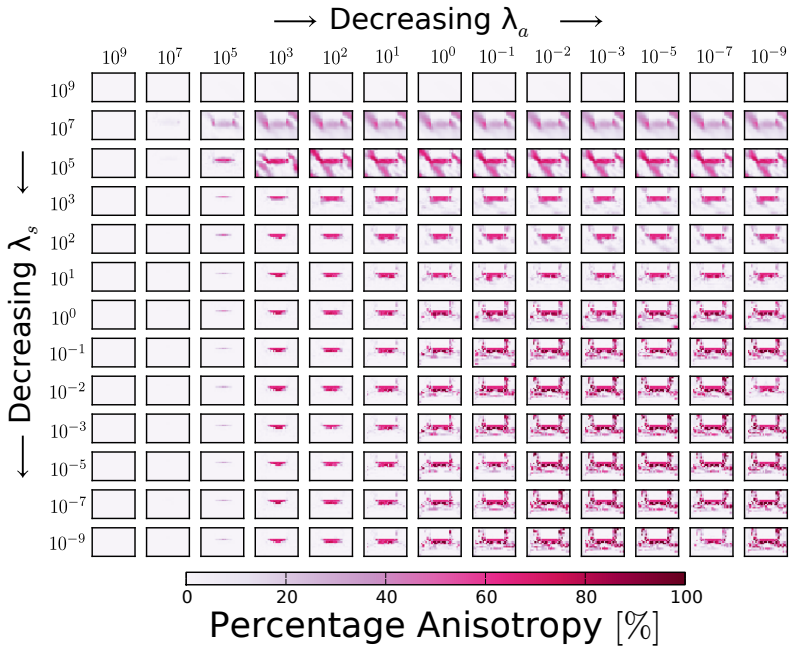

Figure 4.6.: Inversion results for the first test model. The percentage anisotropy for 169 inversion runs is displayed as image arrays and each rectangular represents the result of a single inversion run with fixed regularization parameters. If regularization parameter λ_a is high, the resolved models are isotropic. While λ_a decreases, the resolved model exhibits more and more anisotropic.

3.2, the MT responses (impedance tensor, apparent resistivities and phases) are insensitive to the resistivity variation in vertical direction. If only the vertical resistivity varies, identical responses can be observed at the surface receives (fig. 3.10), no matter how significant the variation is. In other words, a perturbation of the resistivity in vertical direction will not cause any perturbation in surface measurement, e.g. the corresponding part of sensitivity matrix will be very small. As subsequence of that, it is then obvious that this particular part of model update obtained from each inversion iteration will be also insignificant. Therefore, we may deduce that the vertical variation of resistivity is unresolvable in the MT 2D inverse problem. The resolved principal resistivities and percentage anisotropy give us a intuitive view of how well the anomalous body is resolved and how the material property transits from isotropic to anisotropic. Besides that, the root mean square (RMS) error gives insight of how well the inversion converges and the "observed" data is approximated by predicted data. In figure 4.7 the RMS error for all the 169 inversion runs is displayed. As expected, small penalty level produces better data fitting. In this particular case, the best data fitting

appears if the roughness penalty parameter λ_s is less than 10^5 and the anisotropy penalty parameter λ_a is less than 10^2. But one should keep in mind that the best data fitting does not always means the best inversion model, as already discussed, possible over-fitting can be caused by very small penalty parameters.

4.3.2. Relaxation of penalty parameters

The inversion of MT data is non-linear and therefore an iterative approach is needed. In this implementation I use a series of Levenberg-Marquardt iterations and at each iteration appropriate penalty parameters need to be chosen. In the previous examples (figure 4.3 to 4.7) constant levels of penalty parameters of both model roughness and anisotropy were used. Though good inversion results can be obtained using fixed penalty levels, but there are also two deficiencies which make the use of fixed penalty levels quite unpractical. Firstly, a large amount of tests are required in order to find out the "best" penalty level for a particular inversion. Secondly, the regularization terms could become dominant since the data misfit will decrease from iteration to iteration. Fixed penalty levels imply that the inversion is treated as two successive processes, in the first process the data misfit is dominant and

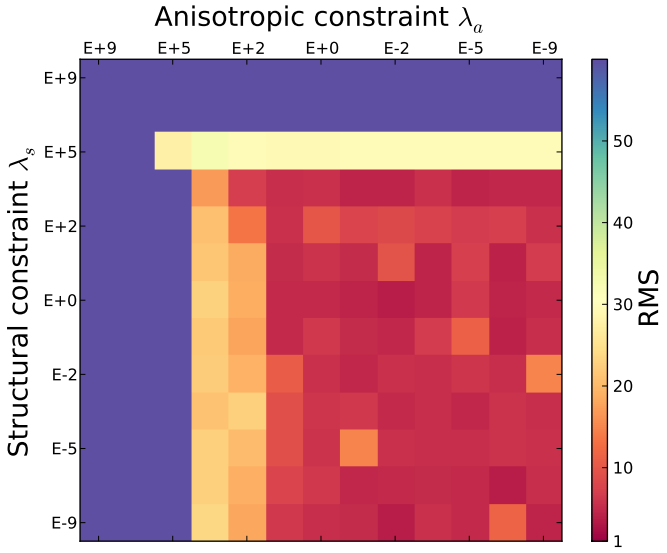

Figure 4.7.: Inversion results for the first test model. The over-all RMS error for 169 inversion runs is displayed. When λ_s and λ_a are both high, the inversion ends up with a considerably high RMS level. Lower RMS can only be reached, when λ_s and λ_a are both low.

structure is mainly developed in this stage, the second process starts after a few iterations when the data misfit is small compare to the roughness penalty and the anisotropy penalty, in other words, the data misfit becomes insignificant and what the inversion does is a kind of fine tuning of the appearance of the resolved model.

Some Authors suggest that the use of a relaxation or "cooling" approach for selecting of regularization parameters is more appropriated compare to the use of fixed penalty level (Pain et al. (2003) and Newman and Hoversten (2000)). The basic idea is to start with a relatively large value of λ and then reduce λ from iteration to iteration. This process of reducing λ continues until an acceptable data misfit is achieved. Experience shows that this approach stabilizes the inversion process at the outset by guarding against arbitrarily rough models that are nonphysical (Newman and Hoversten, 2000). In this section I examine the use of relaxation of the penalty parameters after each iteration and compare the resulting inversion models with those obtained by using of fixed penalty levels. The motivation for relaxation of penalty parameters is twofold. Firstly, it is anticipated that by using large penalty parameters in initial iterations, the large-scale structures and anisotropy information will be recovered. At later iterations, when the penalty parameters become smaller, small-scale features will be created. Secondly, it is difficult to specify "optimum" (by whatever definition) penalty levels without knowledge of the amount of structure and anisotropy contained in the model. Thus it is anticipated that by relaxing the penalty levels after each iteration from a large initial value, "optimum" penalty levels are encountered somewhere along the way and the inversion process can then be terminated (Pain et al., 2003).

Three inversion runs are carried out and the initial penalty parameters are chosen to be 1.0×10^7, 1.0×10^5 and 1.0, respectively. Other inversion settings remain unchanged as described in previous subsection . The inversion runs are carried out with 100 maximal allowed CG iterations for each inversion iteration and a maximal allowed number of inversion iteration of 25. The initial model is a homogeneous isotropic half-space with resistivity of $100\,\Omega\mathrm{m}$ and the results are displayed in figures 4.8, 4.9 and 4.10, respectively. Each figure consists of three panels, in the upper panel the resolved principal resistivities ρ_x, ρ_y and ρ_z are displayed as image arrays against the inversion iterations, in the middle panel the percentage anisotropy is shown for all the 25 inversion iterations and in the lower panel the root mean square (RMS) error is displayed for all inversion iterations. The results show that all the three inversion runs are able to resolve the anomalous structure in the model and the resolved principal resistivities (except the z-component for known reason, see previous subsection) approximate the real resistivity value of $50\,\Omega\mathrm{m}$ in x-direction and $10\,\Omega\mathrm{m}$ in y-direction. The anomalous structure shows distinct anisotropy both in the view of principal

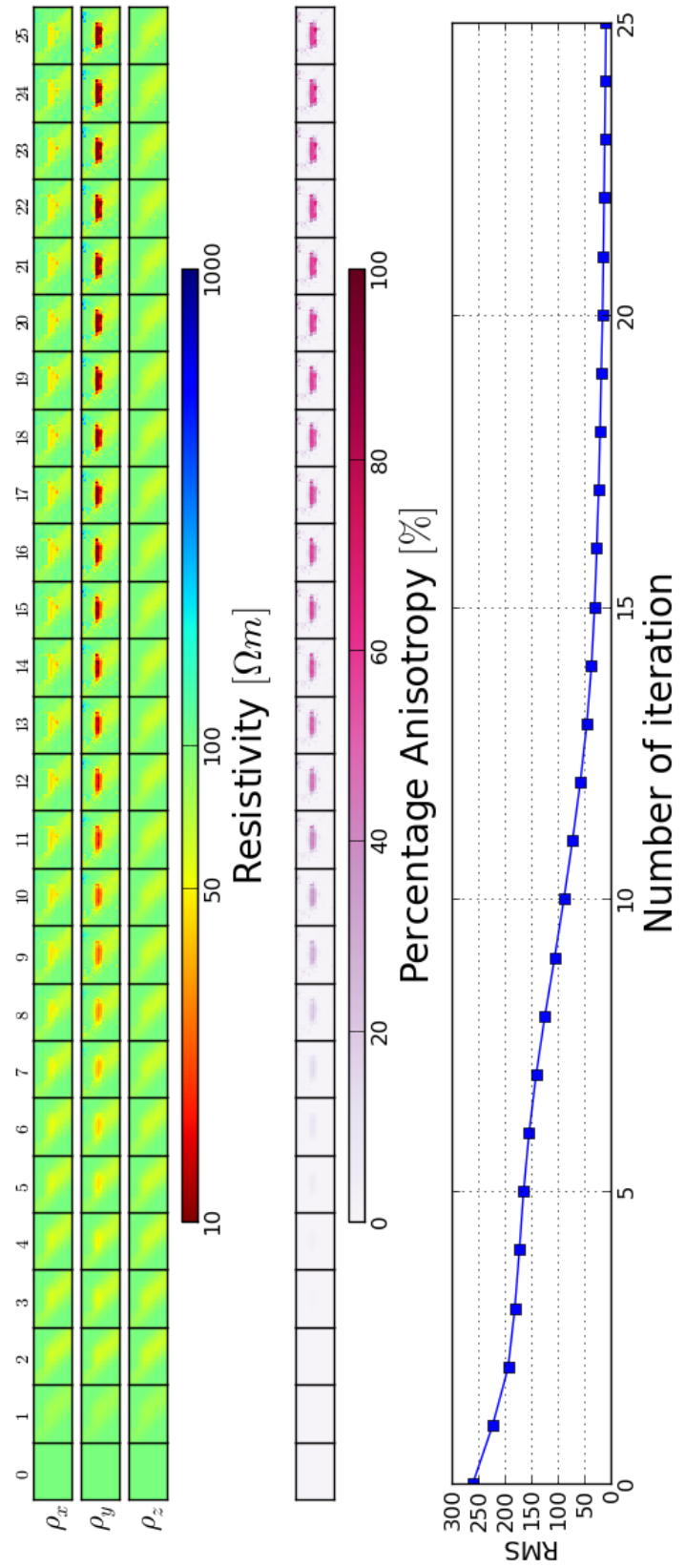

Figure 4.8.: Inversion test for demonstration of the relaxation approach. The initial penalty level of λ_s and λ_a are set both to 1.0×10^7, the maximal number of CG iteration is set to 100. In rows one to three the resolved principal resistivities $\rho_{x,y,z}$ are plotted as image arrays against the number of inversion iteration. In row four, percentage anisotropy (derived from $\rho_{x,y,z}$) is displayed. In row five, the RMS error is plotted as a function of the number of inversion iteration.

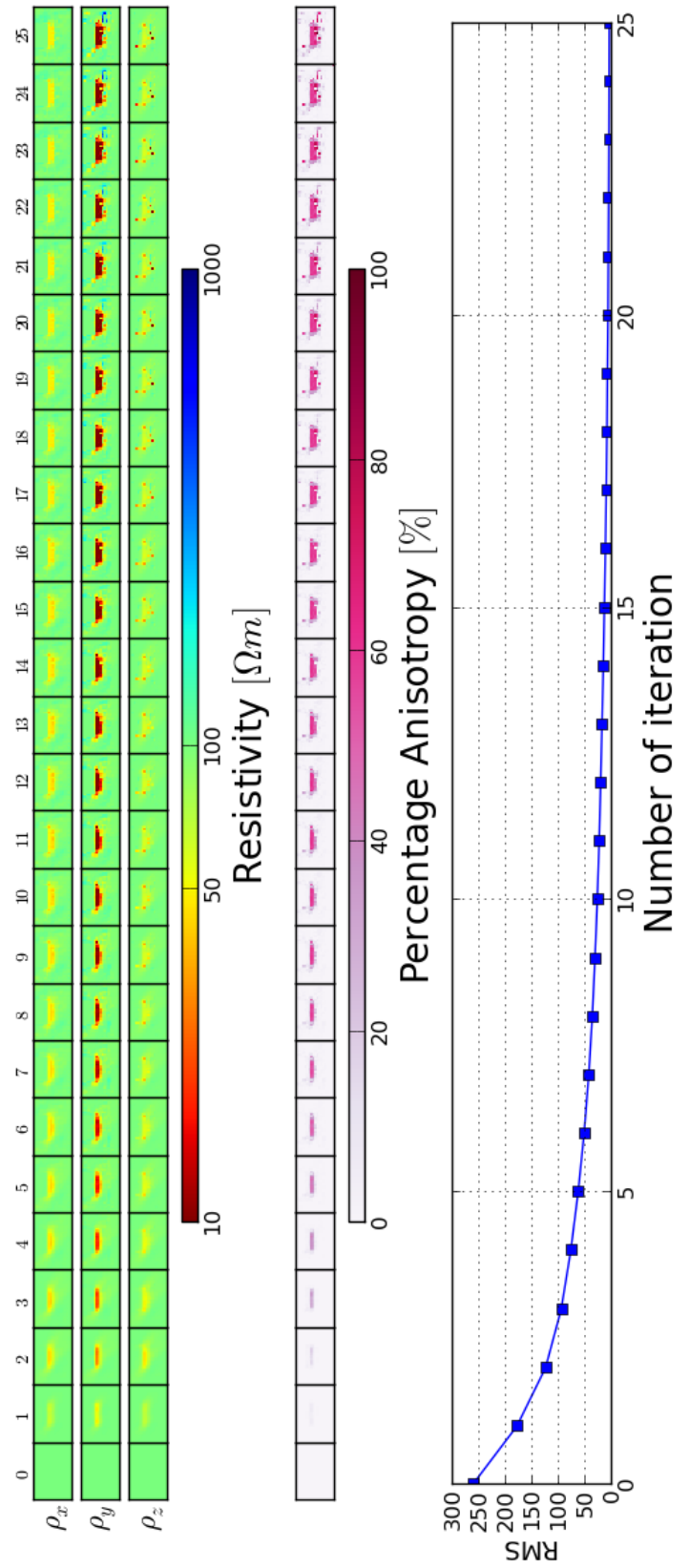

Figure 4.9.: Inversion test for demonstration of the relaxation approach. The initial penalty level of λ_s and λ_a are set both to 1.0×10^5, the maximal number of CG iteration is set to 100. In rows one to three the resolved principal resistivities $\rho_{x,y,z}$ are plotted as image arrays against the number of inversion iteration. In row four, percentage anisotropy (derived from $\rho_{x,y,z}$) is displayed. In row five, the RMS error is plotted as a function of the number of inversion iteration.

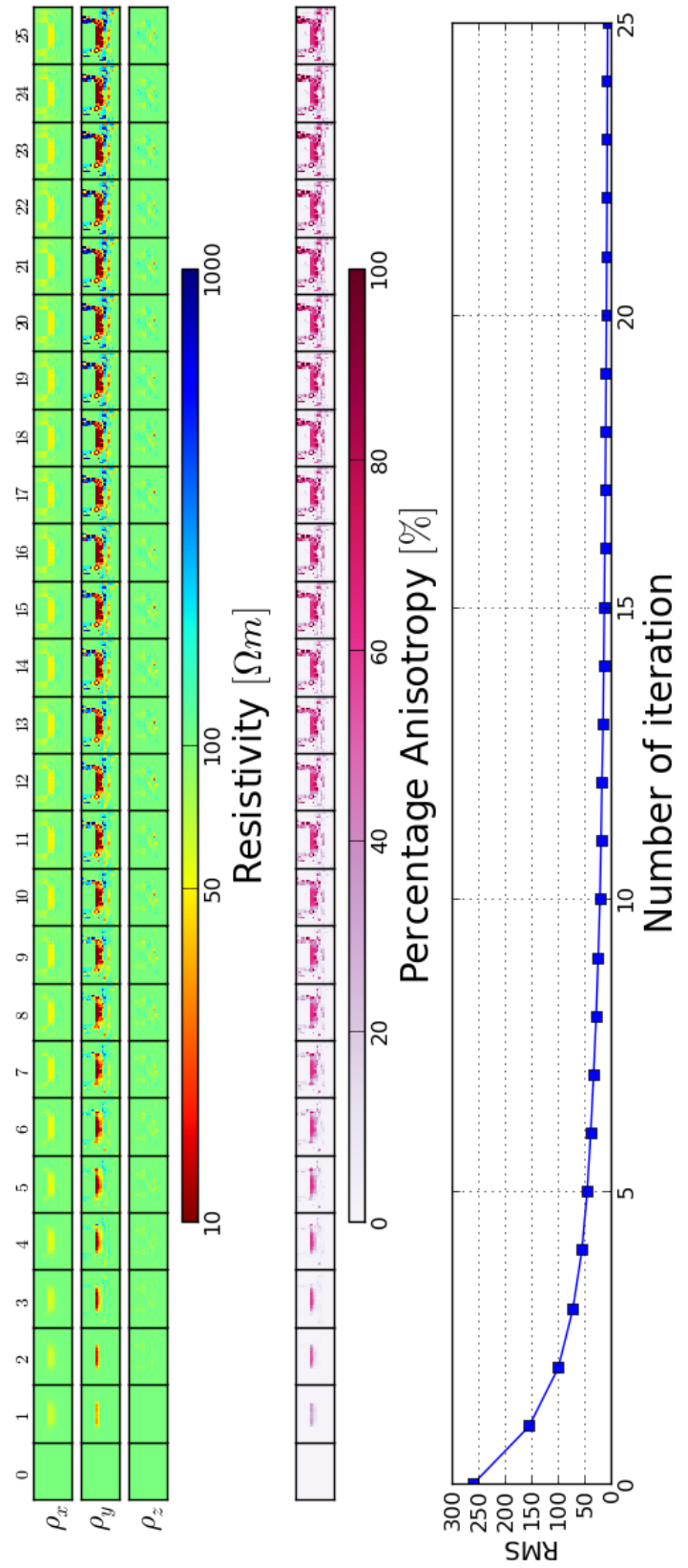

Figure 4.10.: Inversion test for demonstration of the relaxation approach. The initial penalty level of λ_s and λ_a are set both to 1.0, the maximal number of CG iteration is set to 100. In rows one to three the resolved principal resistivities $\rho_{x,y,z}$ are plotted as image arrays against the number of inversion iteration. In row four, percentage anisotropy (derived from $\rho_{x,y,z}$) is displayed. In row five, the RMS error is plotted as a function of the number of inversion iteration.

resistivities and in the percentage anisotropy. Compare the results differences can be observed and I may conclude as following. Firstly, the use of large initial penalty parameters results smooth inversion model. The inversion models, obtained by using 1.0×10^7 and 1.0×10^5 as initial value for both of the penalty parameters (figures 4.8 and 4.9), respectively, are in general smoother than those obtained by using 1.0 as initial penalty parameters (figure 4.10). Secondly, inappropriate initial value of the penalty parameters will cause the creation of artificial structure. The initial value of 1.0×10^7 is obviously too large. Due to strong constraint on model roughness the created structure becomes fuzzy even in the early stage where large-scale structure should be created, which results very smooth model but the bounds of the anomaly becomes unclear (figure 4.8). In contrast, the initial value of 1.0 is too small. The data misfit is dominant in contrast to the model constraints for the whole process, because the data misfit and the model constraints decreases from iteration to iteration. This implies that no control on model appearance is applied and only the data misfit is minimized. Hence, the model update is rough and artificial structure appears after a few iterations (figure 4.10). Thirdly, the inversion converges significantly slow if the applied initial values of the penalty parameters are too large. The inversion run with initial penalty parameters of 1.0×10^7 shows a very slow convergence and the RMS error ends up by 8.9 after 25 inversion iteration (figure 4.8), while the other two inversion runs converge relatively quick and the RMS errors are considerably small after only 15 inversion iterations. Finally and also the most exciting discovery is that starting with relatively large initial penalty parameters will be able to resolve the resistivity anomaly even in vertical direction. The resistivity defined on z-direction is resolved by inversion runs using 1.0×10^7 and 1.0×10^5 as initial value for both of the penalty parameters (figures 4.8 and 4.9) but not by those with small initial value, for example 1.0 (figures 4.10).

4.3.3. Anisotropic strike angle

In the previous subsections I have shown that the implemented inversion procedure is capable to resolve anisotropic resistivities which are defined on the horizontal plane and coincided with the coordinate axis directions. In the paragraph, I will examine the capability of the newly implemented method for dealing with anisotropic features, whose principal resistivities in horizontal plane are oblique to the coordinate axis directions, e.g. horizontal rotation angles (the strike angle, see figure 2.3) have to be taken into account.

The "true" model is similar to the model introduced at the beginning of section 4.3 on page 64. The conductive anomaly (the conductive block) is defined as anisotropic with principal

resistivities $\rho_x, \rho_y, \rho_z = 50, 10, 50\,\Omega\mathrm{m}$, the strike angle $\alpha = 45^\circ$ and the dip- and the slant angles equal zero. Its forward response with a random error of $3-6\%$ of the data, e.g. $3-6\%$ of corresponding elements of the impedance tensor, is used as "measured" data for inversion test. Within this test the following settings are used: the initial penalty parameters for both the model roughness constraint and the anisotropy constraint are chosen to be 1.0×10^5, each inversion iteration (the outer loop) is executed with a maximal allowed number of 100 CG iterations (the inner loop), otherwise the CG iteration will also terminated if the residual falls down to predefined tolerance level of 1.0×10^{-5}. In total there are 25 inversion iteration allowed and the inversion will be also terminated if the RMS error falls down to the predefined tolerance of 1.05. A homogeneous isotropic half-space with resistivity of $100\,\Omega\mathrm{m}$ is used as initial guess (start model).

The results are displayed in figure 4.11. In the first three rows the resolved principal resistivities $\rho_{x,y,z}$ are plotted as image for each inversion iteration. In rows four to six, the resolved rotation angles α, β and γ are displayed as image arrays. In row seven the percentage anisotropy (derived from $\rho_{x,y,z}$) is displayed for each inversion iteration. In row eight, the RMS error is plotted against the number of inversion iteration. In general, the implemented method is able to resolve the anomalous structure (the conductive block) in the model. However, the resolved principal resistivities in horizontal plane, e.g. ρ_x and ρ_y, approximate to a value of $30\,\Omega\mathrm{m}$, which differ to the expected "true" value of $50\,\Omega\mathrm{m}$ and $10\,\Omega\mathrm{m}$ (see 4.11 row one to three). The ρ_z component is not resolved for known reason, see section 4.3.1. In the resolved rotation angles, as expected, the dip angle β is zero, the strike angle α is resolved greater than zero but way too small compared to the predefined value of 45° and the same value is also observed by the slant angle γ even only the strike angle is predefined. This phenomenon reveals the inability of the newly implemented inversion method for resolving horizontal resistivities which are oblique to the horizontal coordinate axes. For the current test, the proposed inversion method resolves an effective resistivity value of approximately $30\,\Omega m$ defined in the horizontal coordinate axes direction for both horizontal resistivities, instead of the predefined "true" value which are oblique to the horizontal coordinate axes. The effective resistivity can be obtained by rotating the predefined anisotropic anomaly with property of $\rho_x, \rho_y, \rho_z = 50, 10, 50\,\Omega\mathrm{m}$ and $\alpha, \beta, \gamma = 45^\circ, 0^\circ, 0^\circ$ by -45° around z-axis, e.g. the horizontal oblique resistivities are rotated back to the coordinate axes directions, and taking the diagonal elements of the resulting matrix, which is equivalent to projection of the oblique resistivities back to the coordinate axes (see equation 4.68 and also section 2.2).

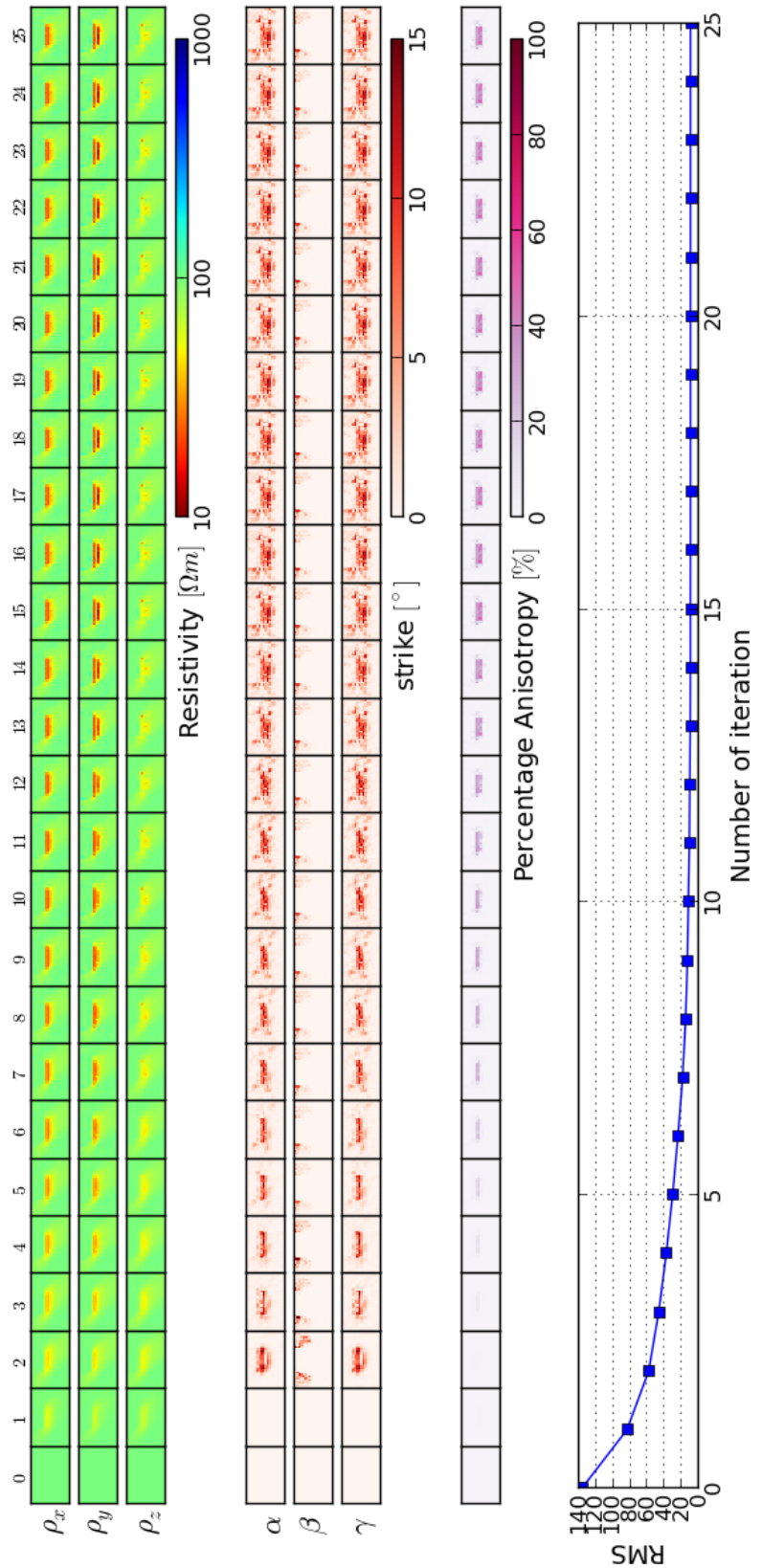

Figure 4.11.: Inversion of synthetic model for resolving the strike angle. The relaxation approach is used and the initial penalty level of λ_s and λ_a are set both to 1.0×10^5, the maximal allowed number of CG iteration is set to 100. In rows one to three the resolved principal resistivities $\rho_{x,y,z}$ are plotted as image arrays against the number of inversion iteration. In rows four to six, the resolved rotation angles α, β and γ are displayed with same manner. In row seven, percentage anisotropy (derived from $\rho_{x,y,z}$) are displayed. In row eight, the RMS error is plotted as a function of the number of inversion iteration.

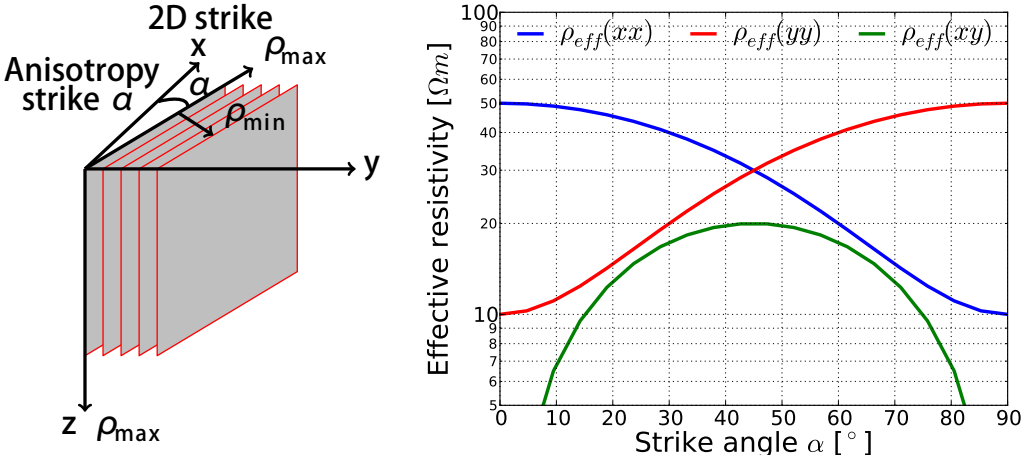

Figure 4.12.: The sketch demonstrates horizontal anisotropy (left panel) and its relation between the effective resistivity and the principal resistivities (right panel) and a mathematical explanation for that can be found in equation 4.68.

$$\rho_{diag.} = \begin{pmatrix} \sigma_{max} & 0 & 0 \\ 0 & \sigma_{min} & 0 \\ 0 & 0 & \sigma_{max} \end{pmatrix} \quad \text{and} \quad \begin{pmatrix} \alpha \\ 0 \\ 0 \end{pmatrix} \xrightarrow{\text{rotate by } -\alpha}$$
$$\rho_{eff.} = \begin{pmatrix} \rho_{max}\cos^2\alpha + \rho_{min}\sin^2\alpha & (\rho_{min} - \rho_{max})\sin\alpha\cos\alpha & 0 \\ (\rho_{min} - \rho_{max})\sin\alpha\cos\alpha & \rho_{max}\sin^2\alpha + \rho_{min}\cos^2\alpha & 0 \\ 0 & 0 & \rho_{min} \end{pmatrix} \tag{4.68}$$

Figure 4.12 demonstrates the horizontal anisotropy (left figure) and the relation between the principal resistivities and the effective resistivity. The resolved strike angle α is hence way too small compared to the predefined "true" value. Because the z-x'-z'' convention of Euler's rotations is used to transform between the full occupied conductivity tensor and its representative with principal resistivity values and rotation angles, the same effect by the strike angle is also observed by the slant angle which is a known effect and already demonstrated by forward model studies in section 3.2 (Fig: 3.11 and 3.11). The percentage anisotropy is also generally small because the resolved effective resistivities are close to each other.

4.3.4. Three block model

The next experiment with synthetic data uses a more complicated model. The model consists of three rectangular bodies A, B and C embedded in a $100\,\Omega\mathrm{m}$ background D. The anomalous body A has dimensions (in $l \times h$) of 5×14 km and its top is 5 km below the Earth's surface, which owns electrically anisotropic properties with $\rho_x, \rho_y, \rho_z = 50, 5, 50\,\Omega\mathrm{m}$ and $\alpha, \beta, \gamma = 30°, 0°, 0°$; the body B is adjacent to A, it has dimensions of 4×9 km and its top is 10 km below the Earth's surface, which is also anisotropic with $\rho_x, \rho_y, \rho_z = 300, 30, 300\,\Omega\mathrm{m}$ and $\alpha, \beta, \gamma = 120°, 0°, 0°$, so the principal directions of the body A and B are perpendicular to each other; the body C has dimensions of 6×11 km and its top is 2.5 km below the Earth's surface, it is isotropic with resistivity of $1000\,\Omega\mathrm{m}$ (see figure 4.13). The test uses synthetic data for both the E- and H-polarizations at nine MT sites and 15 frequencies, which yields a total of 540 real-valued data. The frequencies range from 0.001 to 100 Hz and are evenly spaced on a logarithmic scale. The model parameterization for inversion divides the Earth into a grid of blocks numbering 30 in the horizontal y-direction and 20 in the vertical z-direction, implying a total of 3600 model parameters with consideration of electrical anisotropy. The initial penalty parameters (λ_s and λ_a) are both chosen as 10, which will be relaxed by a factor of two after each successful inversion iteration (in this context, a successful inversion iteration means that the current RMS error is smaller than the one of the previous inversion iteration). The maximal allowed number of CG iterations (the inner loop) was chosen as 100 and the tolerance level of residual was set as 1.0×10^{-5}, which means that the CG iteration will be terminated if the maximal allowed iteration number is reached or the residual falls down to the tolerance level. The maximal allowed number of inversion iteration (the outer loop) was chosen as 25 and the tolerance level of RMS error was set as 1.05, which implies that the inversion will be terminated if the maximal number of inversion iteration is reached or the RMS error falls down to 1.05. The starting model was a uniform halfspace with $\rho = 100\,\Omega\mathrm{m}$.

Figure 4.14 displays the inversion models containing different component of the horizontal principal resistivities, e.g. the ρ_x component in the upper panel and the ρ_y component in the lower panel, respectively. The images are truncated spatially to display the best resolved parameters; deeper features and those laterally away from the station array are not shown. Figure 4.15 shows a wrap-up for all the 25 inversion iteration. In the upmost panel, rows one to three, the resolved model generated by each component of the principal resistivities are displayed as image array against the number of the inversion iteration. In the second panel, rows four to six, the resolved rotation angles are displayed in a same manner. In the

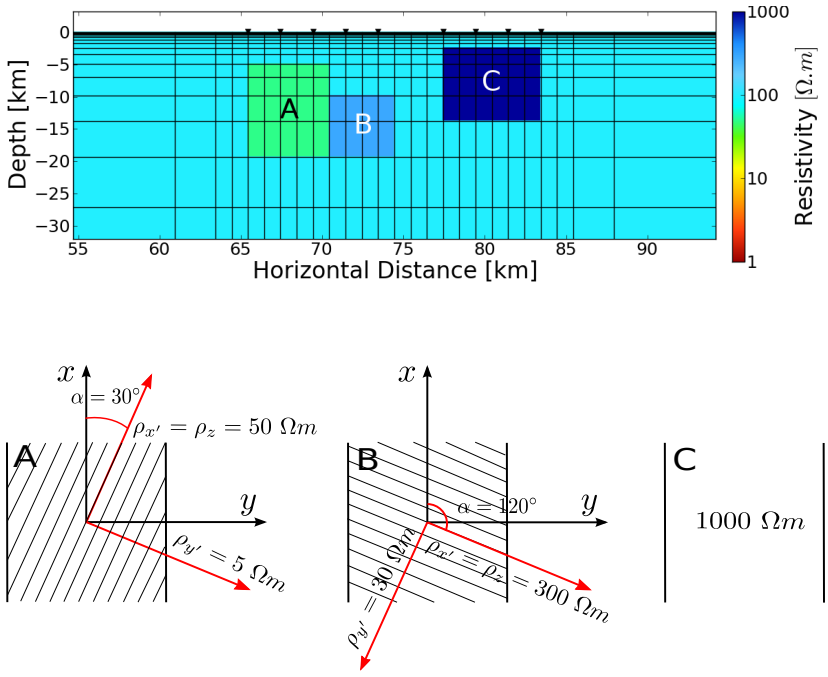

Figure 4.13.: "True" model consists of three anomalous blocks embedded in a homogeneous isotropic half-space with resistivity of $100\,\Omega\mathrm{m}$. The model is displayed at the top panel as a cross section and the properties of three anomalous blocks are displayed at the bottom panel. The forward responses of this model are used as "real" data for inversion test.

third panel, the percentage anisotropy is shown as image array along the increasing number of the inversion iteration. In the lower panel, the RMS error is plotted as a function of the inversion iteration number.

The final models generated by horizontal components of the principal resistivity are clearly similar (Figure 4.14). The isotropic block C is resolved in both components and the resolved resistivity approximates the "true" value of $1000\,\Omega\mathrm{m}$. However, in the ρ_x component, the upper, left and right bounds of block C are precisely resolved, while its lower bound is reconstructed much shallower than the "true" value. In contrast, in the ρ_y component, the upper bound of block C is precisely resolved and its lower bound approximates the "true" value, but the lateral extension of block C is much larger than its "true" value. If we compute the percentage anisotropy for the entire model, the area of the block C appears as anisotropic just because the different discussed above and can be observed clearly in the third panel of figure (4.15). The anisotropic blocks A and B appear in the resulting models as one block and cannot be distinguished from each other. As already discussed in previous subsection,

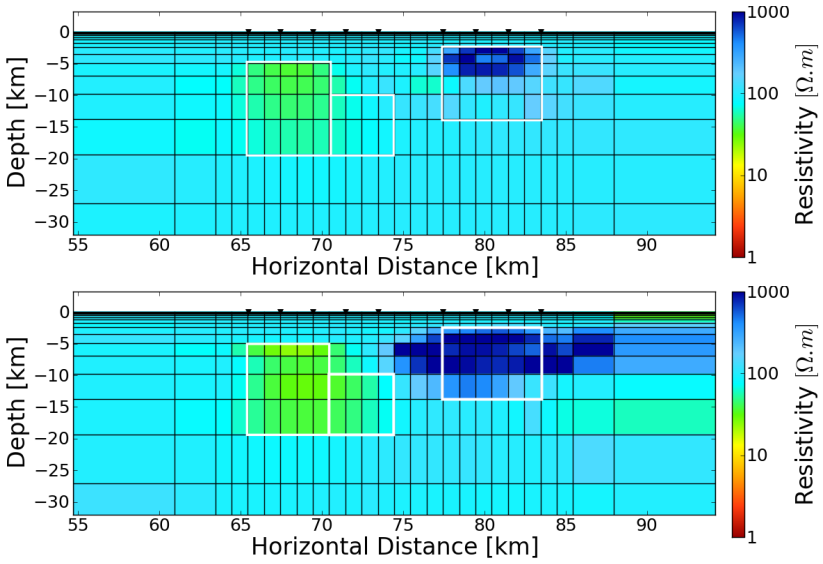

Figure 4.14.: Resulting inversion models. The ρ_x component (upper panel) and the ρ_y component (lower panel) with the original locations of three anomalous blocks (masked as white rectangular) as reference.

only the effective value of resistivity can be resolved for an oblique anisotropic structure, due to the loss of information about the rotation angles. For this particular case, the inversion procedure is only able to resolve an average of both effective values related to the block A and B due to the adjacency of these two blocks. Hence, these two blocks appear even less anisotropy than the isotropic block C (see third panel of figure 4.15). Nevertheless, the resolved rotation angles show that only angles are observed at the locations where the blocks A and B are, which is an evidence for possible anisotropy. As discussed in previous subsection and also demonstrated by forward studies in section 3.2 (Fig: 3.11 and 3.12), the same value will be observed for both the strike angle and the slant angle.

4.3.5. MT phases out of quadrant

The last experiment with synthetic data I examine the capability of the newly implemented inversion procedure for dealing with data containing phases out of the expected quadrant. I adopted a model from section 3.2.2 which is used for forward modeling and demonstration of the effect that MT phases out of quadrant can be modeled by 2D anisotropic forward modeling. The model consists of a $300\,\mathrm{m}$ isotropic surface layer and a isotropic half-space

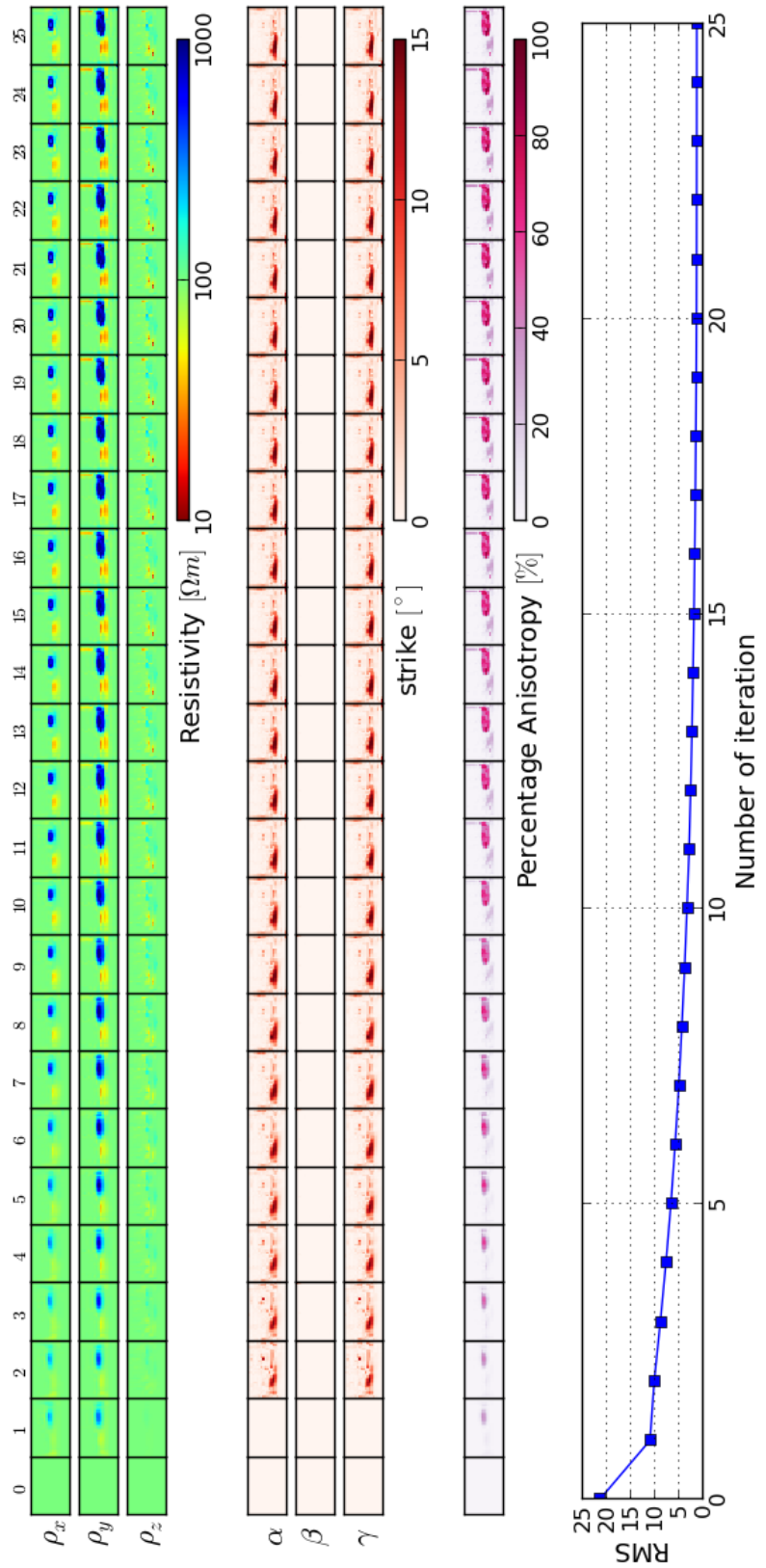

Figure 4.15.: Inversion results for three block model. The relaxation approach is applied and the initial penalty level of λ_s and λ_a are set both as 10, the maximal allowed number of CG iteration is set to 100. In rows one to three the resolved principal resistivities $\rho_{x,y,z}$ are plotted as image arrays against the number of inversion iteration. In rows four to six, the resolved rotation angles α, β and γ are displayed with same manner. In row seven, percentage anisotropy (derived from $\rho_{x,y,z}$) are displayed. In row eight, the RMS error is plotted as a function of the number of inversion iteration.

with resistivity of $100\,\Omega\mathrm{m}$. Two anisotropy blocks are embedded in the half-space. The first block started at depth of $300\,\mathrm{m}$ and shaped as a trapezoid, which is anisotropic with $\rho_x, \rho_y, \rho_z = 50, 0.5, 50\,\Omega\mathrm{m}$ and $\alpha, \beta, \gamma = 120°, 0°, 0°$. The second block is a rectangular body located beneath the first block and started at depth of 6.8 km (figure 4.16), it is also anisotropic with $\rho_x, \rho_y, \rho_z = 30, 0.3, 30\,\Omega\mathrm{m}$ and $\alpha, \beta, \gamma = 30°, 0°, 0°$. Its forward response was demonstrated in section 3.2.2 (figure 3.15, right lower panel) and shown that the MT phases out of the first quadrant ($> 90°$) are produced through the introduced model. The goal of this inversion test is to check if the anomalous large phases can be fitted by anisotropic inversion. The test uses synthetic data for both the E- and H-polarizations at 6 MT sites and 16 frequencies, which yields a total of 384 real-valued data. The frequencies range from 0.001 to 1000 Hz and are evenly spaced on a logarithmic scale. The model parameterization for inversion divides the Earth into a grid of blocks numbering 120 in the horizontal y-direction and 55 in the vertical z-direction, implying a total of 39600 model parameters with consideration of electrical anisotropy. The initial penalty parameters (λ_s and λ_a) are chosen as 1000 and 10, respectively, which will be relaxed by a factor of two after each successful inversion iteration (in this context, a successful inversion iteration means that the current RMS error is smaller than the one of the previous inversion iteration). The maximal allowed number of CG iterations (the inner loop) was chosen as 100 and the tolerance level of residual was set as 1.0×10^{-5}, which means that the CG iteration will be terminated if the maximal allowed iteration number is reached or the residual falls down to the tolerance level. The maximal allowed number of inversion iteration (the outer loop) was chosen as 25 and the tolerance level of RMS error was set as 1.05, which implies that the inversion will be terminated if the maximal number of inversion iteration is reached or the RMS error falls down to 1.05. The starting model was a uniform halfspace with $\rho = 100\,\Omega\mathrm{m}$.

Figure 4.17 displays the final inversion models generated after 18 iterations, which are the ρ_x component in the upper panel and the ρ_y component in the lower panel, respectively. The images are truncated spatially to display the best resolved parameters; deeper features and those laterally away from the station array are not shown. The inversion results show that the structures which produce the anomalous phases can not be fully reconstructed by the proposed inversion method. However, a remarkable degree of similarity can be observed between the true model and the inversion model. In the resolved ρ_x component, the upper panel in figure 4.17, two anomalous structures can be roughly recognized. However, the inversion tried to fill the inbetween area of these two structures with some intermediate features. In the resolved ρ_y component, the lower panel in figure 4.17, the two anomalous blocks are resolved as one big structure shaped as a trapezoid and extend from the top of

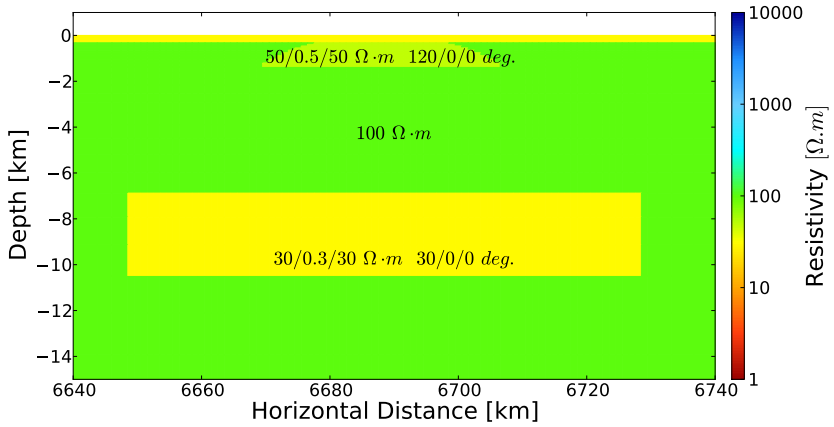

Figure 4.16.: "True" model with two anomalous blocks. Its forward responses contain phases out of quadrant ($> 90°$) and are used as "real" data for inversion test.

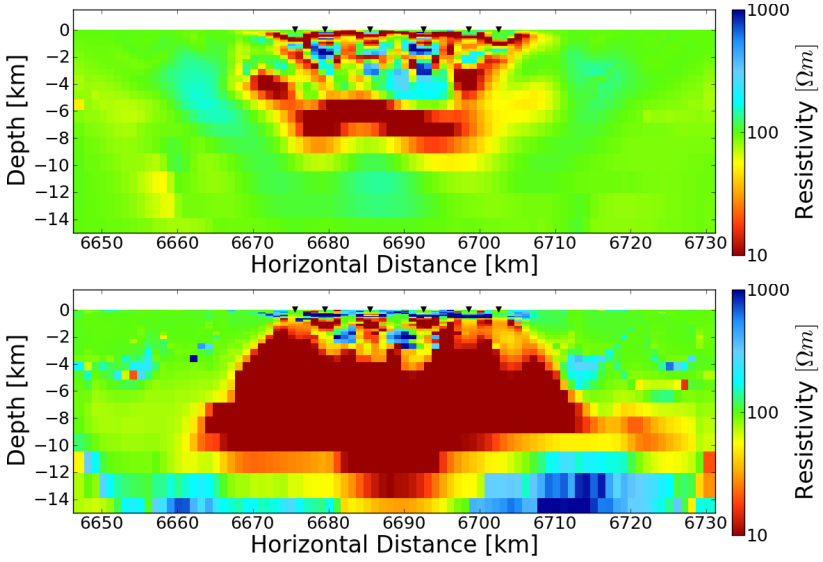

Figure 4.17.: Resulting inversion models. The ρ_x component (upper panel) and the ρ_y component (lower panel).

the model, approximately from 300 m beneath the surface, to a depth of 12 km with some intermediate features created at the shallow range between the sites location. Figure 4.19 displays the data fit of all the six sites located above the anomalies. The data fit reveals a great agreement in apparent resistivity, while the same effect can also be observed in phase as long as the phases of "true" data stay inside the first quadrant. When the phases of "true" data go into the second quadrant, the phases of the predicted data attempt to approximate

90° but will never be greater than it. This indicates that the effect of phases out of quadrant can not be reproduced using the proposed inversion method. One possible reason for this is that only the effective resistivities can be resolved if the rotation angles are involved into inversion. This is equivalent to a projection of different anisotropic properties, defined on different coordinates, onto the basis coordinate on which the model is defined. After the projection the information about rotation angles is lost. Since all the effective resistivities are defined on the same coordinate system, there is no potential to force the current flow changes its preferred direction and hence no phases out of quadrant can be observed. Nevertheless, a comparison of the impedance elements between the predicted data and the raw data (the forward responses of the "true" model for the site 003 shows that for the xy-component is positive for the entire period range and for both the raw data and the predicted data (left panel of figure 4.18), which explains why the phases of this component are all in the range of $(0^\circ, 90^\circ)$. In contrast, the yx-component of the raw data is negative in short period range $[0.001\,\mathrm{s} \sim 200\,\mathrm{s}]$ and it becomes positive in period range of $(200\,\mathrm{s} \sim 3000\,\mathrm{s})$, while the same component of the predicted data is negative for the entire period range (right panel of figure 4.18. This explains nicely why phases out of quadrant occur and where the large phase anomaly comes from. The zoomed image in the right panel of figure 4.18 demonstrates this behaviors and we may observe that the differences of the raw data and the predicted data are not that big, especially for the last $3\sim4$ data points. However, the change of sign is enough to cause the transition of phases into another quadrant, because the phases are calculated by the ratio of the real part and imaginary part of impedance. The change of sign for either the real part or the imaginary part will not affect the apparent resistivities, because they are measured by the quadratic values of impedance. This explains the phenomenon that we observed in figure 4.19 where a good data fit appears in the apparent resistivity but not in the phase.

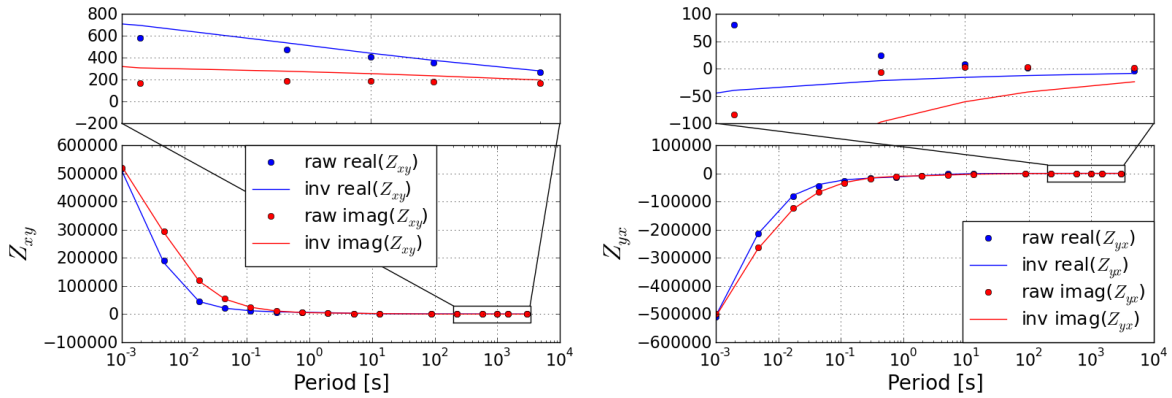

Figure 4.18.: Data fit of impedance tensor elements (the off-diagonal elements) for site 003. The xy-component (left panel) and the yx-component are displayed. Points represent the raw data (the forward responses of the "true" model) and the solid lines denote the inversion results , e.g. the predicted data. Blue indicates the real part of the impedance element and red denotes the imaginary part.

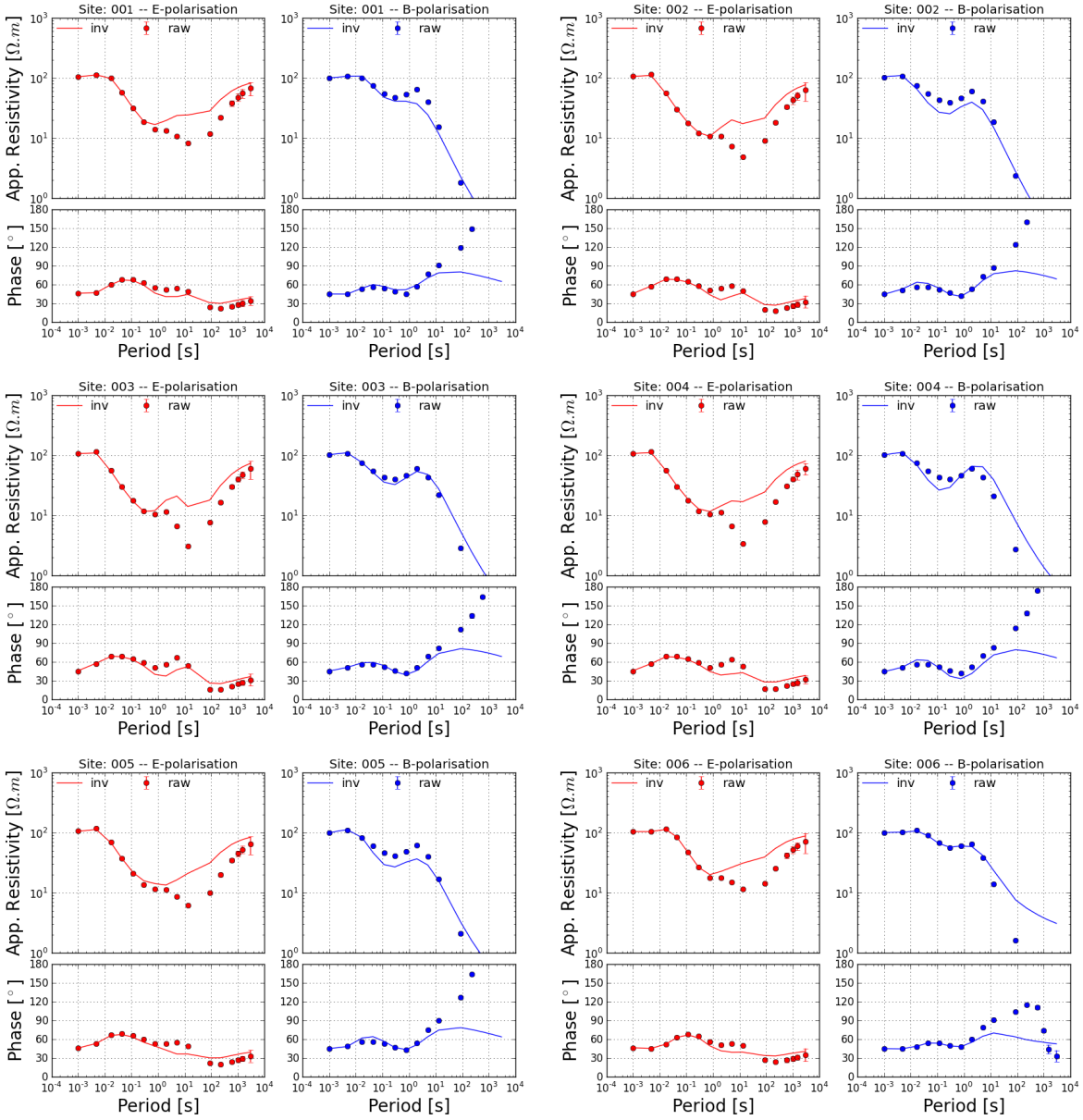

Figure 4.19.: Data fit of apparent resistivity and phase for all the six sites. The points represent the raw data (the forward responses of the "true" model) and the solid lines denote the inversion results , e.g. the predicted data, at each site. Red color indicates the E-polarisation component and blue indicates the B-polarisation component.

Chapter 5.

Magnetotelluric measurements across the Cape Fold Belt, RSA

5.1. Introduction

The Cape Fold Belt (CFB) in South Africa is a major Phanerozoic African structure that has been studied for more than a century (Reeves and de Wit, 2000, Milani and de Wit, 2008, de Wit et al., 2008). During the last two decades researchers who have focused on the structural geology of the Cape Fold Belt, in particular, have provided greater insight into local characteristics of the fold belt, but a broader understanding of the tectonic development of the fold belt is not without controversy (e.g. Shone et al., 1990, Newton et al., 2006, Paton, 2006, Tankard et al., 2009, Booth, 2011). Recent regional refraction- and tele-seismic experiments reveal only general crustal thickness variations, but poorly define internal structures beneath the CFB (Paton, 2006, Stankiewicz et al., 2008, Parsiegla et al., 2009).

This hampers further understanding of the structure and evolution of the CFB (Milani and de Wit, 2008). Within the framework of the German - South African geo-scientific research initiative Inkaba yeAfrica several magnetotelluric (MT) field experiments were conducted along the Agulhas-Karoo geoscientific Transect in South Africa. This transect is designed to cross the CFB with the kango Basin, the Namaqua-Natal Mobile Belt, the Karoo Basin and the transition into the Kaapvaal Craton. One magnetotelluric (MT) experiment is carried out across the CFB in November 2005. The location of the MT profile allows the construction of an upper crustal conductivity section across the CFB from its northern tectonic front to its southernmost coastal ranges.

5.2. Geological and tectonic background

The CFB is located at the southernmost tip of the African continent and extends for approximately 1300 km along the southern part of the South African coastal margin where predominantly meta-sedimentary rocks of Late Proterozoic (Pre-Cape), Palaeozoic (Cape Supergroup) and Mesozoic (Karoo Supergroup) age crop out and define two tectonic domains (Figure 5.1), separated by the Cape Syntaxis. The main southern domain has an east-west trend, and the north-northwesterly trending domain forms the western part of the fold belt. The syntaxis is the region approximately 100 kilometers east of Cape Town where the two domains of the fold belt meet, and interference fold structures are present (De Beer, 1992, Booth, 2011).

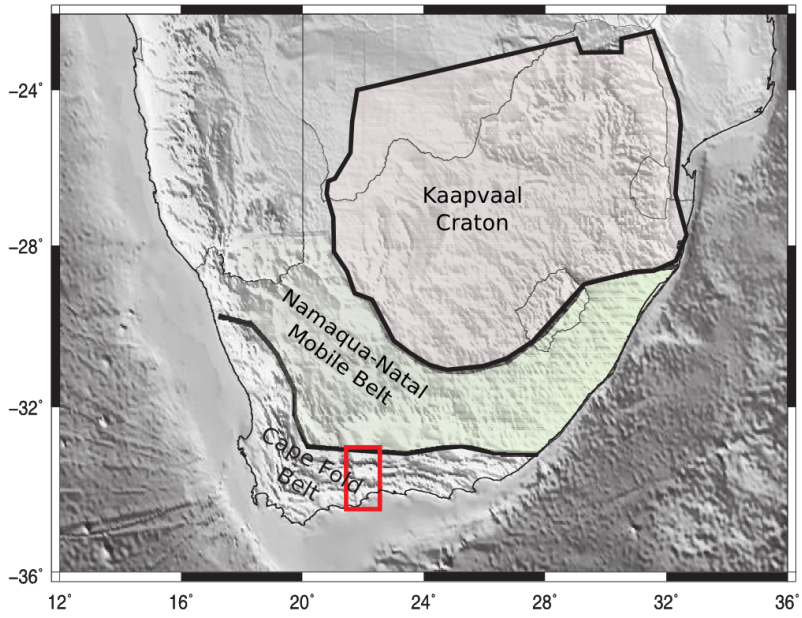

Figure 5.1.: Location map of the Cape Fold Belt (CFB). The study area across the CFB from its northern tectonic front to its southernmost coastal ranges and marked by red rectangle (pers. comm. Weckmann).

The CFB formed in response to subduction-related compression during Paleozoic-Mesozoic convergence along the southwestern margin of Gondwana resulted in a coupled CFB-Karoo Foreland Basin (Hälbich, 1983, Milani and de Wit, 2008, Tankard et al., 2009, Lindeque et al., 2011). The main deformation took place at ca. 250 Ma. This tectonism affected Proterozoic metasediments and an unconformably overlying Palaeozoic cover. Crystalline

Proterozoic basement is not exposed anywhere in the CFB. The MT experiment is carried out across the southern domain of the CFB, masked through red rectangle in figure 5.1, in this area the Proterozoic metasediments are exposed in tectonic windows known as the Kango and Kaaimans Inliers that range in age between ca. 520 and 1050 Ma (Barnett et al., 1997). Lower Cambrian granite intrudes the Kaaimans Group (figure 5.2).

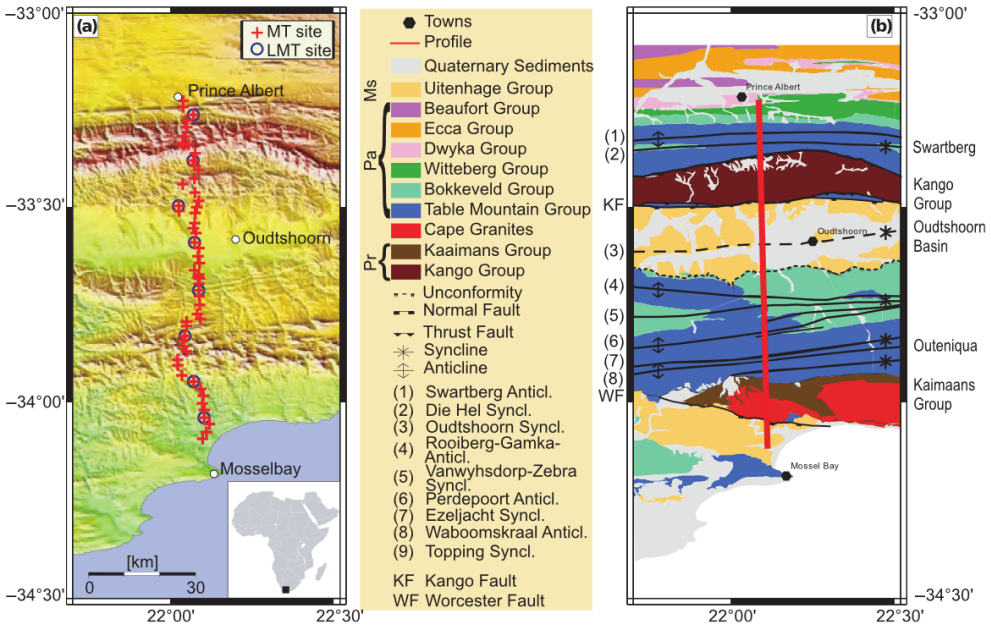

Figure 5.2.: Location map of the study area with geological map as reference. The MT profile is denoted as a set of red crosses in the left panel, where each cross represents a single MT site, and a red line in the right panel (Weckmann et al., 2012).

Unconformably overlying these rocks and making up the highest mountain ranges of the CFB are predominantly thick dense quartzite units of the lower Paleozoic Cape Supergroup (Table Mountain and Witteberg Groups). These prominent ranges, which outcrop for hundreds of kilometers along the strike of the CFB, are separated by softer Silurian-Devonian shales (Bokkeveld Group) exposed mostly in the adjacent valleys. Permo-Carboniferous tillites (Dwyka Group) and finer siliciclastic rocks of the Permo-Triassic Karoo Supergroup make up the uppermost sequences, but these are preserved predominantly only in the Karoo foreland basin (Johnson et al., 1997, Fildani et al., 2009).

The MT profile across the CFB runs close to an amphibian seismic refraction profile (Stankiewicz et al., 2008, Parsiegla et al., 2009) that reveals a steep decrease in crustal thickness from ca.

42 km below the tectonic front of the CFB (at the Swartberg Mountains) to ca. 30 km below the coastal ranges. A high-velocity mid-lower crust probably comprises Meso-Proterozoic crystalline basement (Stankiewicz et al., 2008). The Swartberg and the Outeniqua Mountains display slow p-wave velocities down to about 2 km depth, similar to the Kango and Kaaimans metasediments within the uppermost 1 km of the crust.

Cretaceous basins, located along strike of the CFB at the east coast, are known to project westward into the intermontaine basins of the CFB (Dingle et al., 1983, Brown et al., 1995, Paton, 2006). The correlations reveal that the normal south-dipping listric fault systems separate the onshore Cretaceous basins from the Proterozoic inliers with displacements of $2{\sim}6$ km (e.g. the Worcester and Kango Faults). Paton (2006) speculated that these faults are linked at mid-crustal depths to a mega-extensional detachment fault underlying the entire CFB and increasing in depth from ~ 10 km beneath the CFB tectonic front to about 30 km near the coast (i.e. close to Moho depths). Paton further speculated that above these Cretaceous normal faults systems exploited earlier Paleozoic thrusts systems and that the CFB changed from being a "thick-skinned" belt beneath the coastal ranges to a "thin-skinned" belt closer to its tectonic front. Farther north, the thrusts apparently extend into the adjacent Karoo Basin (Paton, 2006) where shallow ($2-3$ km depth) decollements have been mapped using a seismic reflection profile across the Karoo Basin (Lindeque et al., 2011). Other authors have suggested instead that the junction between the CFB and the Karoo Basin is a steeply dipping crustal transform fault that effectively decoupled these two tectonic domains (Johnston, 2000, Tankard et al., 2009). Tankard et al. (2009) further suggest that intermontaine listric Kango and Worchester Faults are part of transpressional flower structures, including the Kango and the Kaaimans inliers and their bounding mountain ranges. Such a model requires a depth extent of 8 km for the inliers, and 6-11 km for the Outeniqua and Swartberg Mountains respectively (Tankard et al., 2009). These widely different models serve as examples to emphasize the lack of consensus about even the simplest geometry of the upper crustal structures that underlie the CFB, and therefore its tectonic evolution. Hence, the MT data obtained along a profile across the CFB can be used to test some of these controversies.

5.3. Interpretation of the Cape-Fold-Belt MT data

5.3.1. Magnetotelluric data and regional strike direction analyses

Magnetotelluric data were recorded at 52 MT stations spaced at 2 km intervals along a 100 km long profile across the CFB (figure 5.2). Such a dense spacing facilitates high-resolution MT modeling compared with the typical spacing of ~ 10 km for regional surveys (e.g. Jones et al., 2009), which is a proxy for spatial resolution. Electric and magnetic field variations ($1\,\mathrm{kHz} - 1\,\mathrm{mHz}$) were measured using S.P.A.M. MkIII and CASTLE instruments, Metronix induction coils and Ag/AgCl electrodes and processed according to Ritter et al. (1998) and Weckmann (2005). Figure 5.3 shows the data displayed in pseudo-sections.

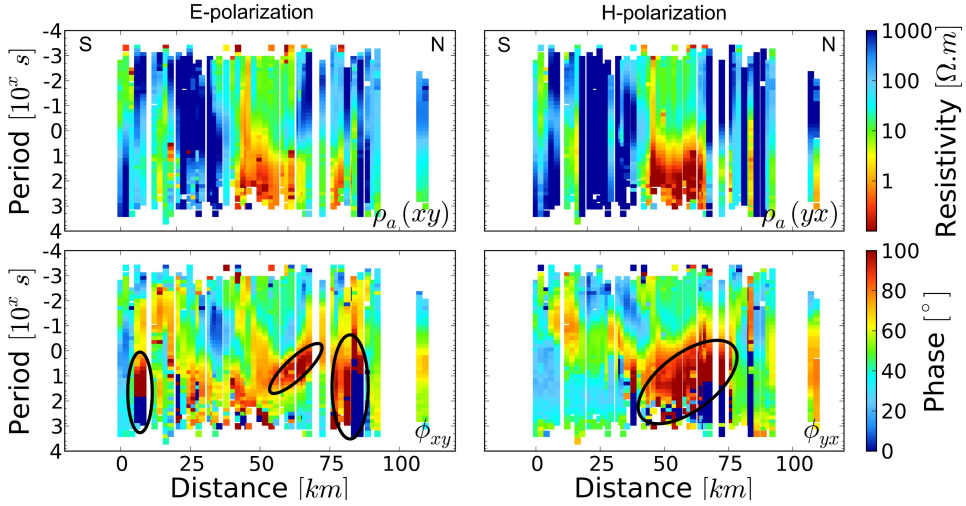

Figure 5.3.: Results of data processing, MT data displayed in pseudo-sections. Note that MT phases greater than 90° occur in the middle of the profile for periods $> 0.1s$ in both TE and TM component (marked with black ellipses in the lower panel).

The apparent resistivities measured inside the frequency range for all the sites are displayed in the upper panel of both E-polarization and H-Polarization. As common features we can observe that a big conductive zone located in the middle of the profile and it is neighbored by two resistive features. The resistive features start at the Earth's surface and extend to a great depth, while the conductive zone begins at a relatively long period of approximately 10 s. The phases which are displayed in the lower panel of both polarizations exhibit an area (> 10 km) where MT phases greater than 90° occur (marked with black ellipses in figure

5.3). From the pseudo-sections we are already able to recognize some features and it is clear that different period indicates resolution in different depth, but they are still in a stage of "raw" data and hence cannot be interpreted directly. In order to resolve the "true" locations of these features, appropriate modeling and inversion procedures are needed.

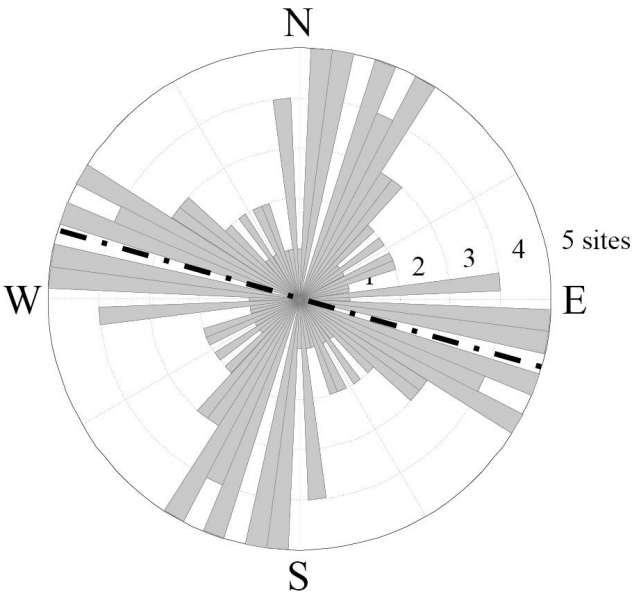

Figure 5.4.: The calculated strike directions using data from all sites and over the entire period range are displayed in form of a rose diagram. A general strike direction of $N76°W$ can be recognized and which represents the regional geologic structure of the east-west trending CFB, the perpendicular sector in the rose diagram show the $90°$ ambiguity in the calculated strike direction (Tietze et al., 2007).

Regional strike direction is calculated using the method described by Becken and Burkhardt (2004) including data from all sites and over the entire period range and displayed in a rose diagram (figure 5.4). Although the strike direction varies, a general strike direction of $N76°W$ can be still recognized and which represents the regional geologic structure of the east-west trending CFB, the perpendicular sector of $N14°E$ in the rose diagram show the $90°$ ambiguity in the calculated strike direction. The distribution of single site strike direction scatters around the average value and thus indicates the complexity of the underlying structures, e.g. not purely two-dimensional.

5.3.2. Isotropic 2D inversion and interpretation

Although a isotropic 2D inversion may not appropriate for the observed effects in the data, in a first approach we would like to get an idea what can be explained by a 2D isotropic model. In the process of doing so, I have observed that the standard 2D isotropic inversion procedure failed to deal with the data, mainly because a considerable amount of data can not be fitted, especially those with phases greater than $90°$. In order to satisfy the standard 2D isotropic inversion procedure I have to discard this part of data. Figure 5.5 shows the final data set used for 2D isotropic inversion. Note that data with phases greater than $90°$ are excluded.

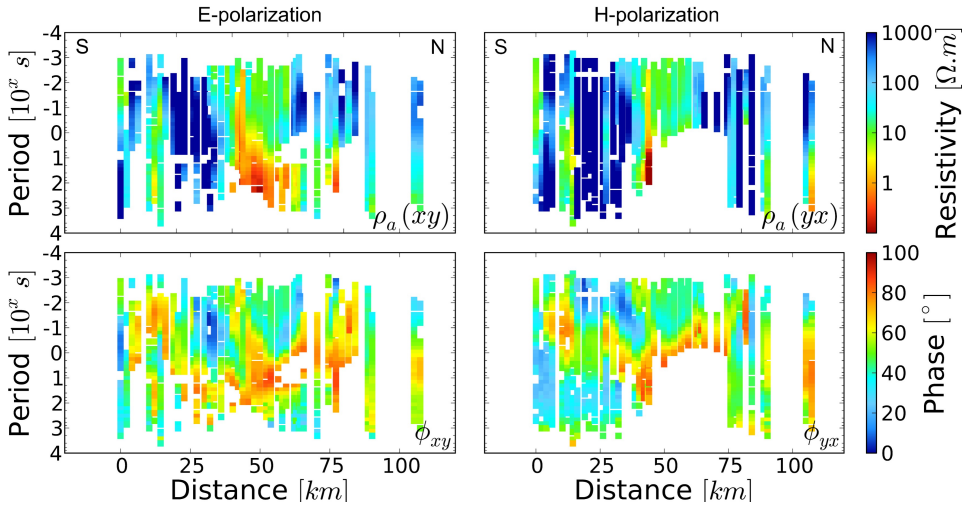

Figure 5.5.: Final data set used for 2D isotropic inversion. Data with phases greater than $90°$ are excluded in order to satisfy the standard 2D isotropic inversion procedure.

Isotropic 2D inversion is carried out using the RLM2DI algorithm (Rodi and Mackie, 2001). Inversion was started from a homogeneous half-space of $100\,\Omega\mathrm{m}$ with a mesh of 235 horizontal and 174 vertical cells and using E- and H-polarization data. The regularization parameter τ, which controls the trade-off between data misfit and model roughness, was chosen to be 10 after computing a trade-off for different τ values. Error bounds were set to $0.6°$ for the phases and to 10% for the H-polarization and 100% for the E-polarization apparent resistivities.

The inversion finished by a overall RMS error of 2.24 and the results yield several prominent conductive and resistive features (figure 5.6, labeled by c1$-$c5 and r1$-$r4, respectively). Resistor r1 is located beneath the Swartberg Mountains and extends to a depth of $\sim$10 km,

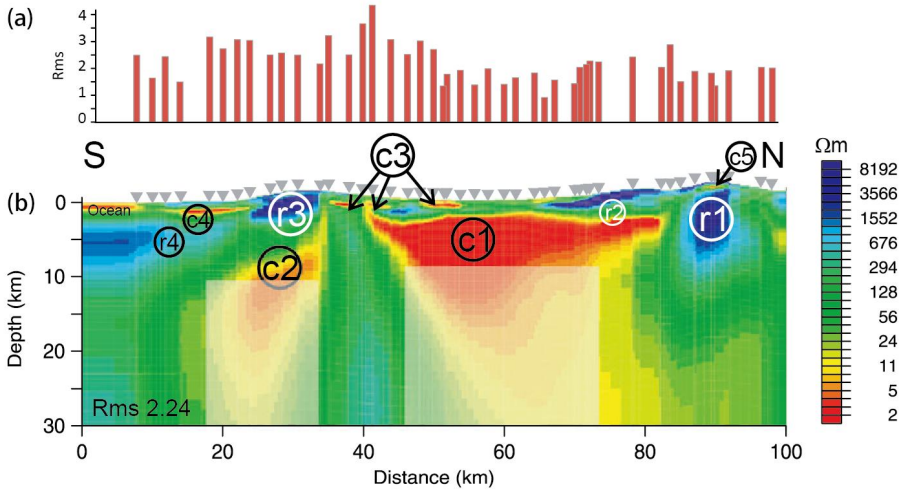

Figure 5.6.: Results of 2D isotropic inversion: Data fit at individual sites (a) for 2D inversion model (b). Several very prominent conductivity anomalies, labeled c1−c5 and r1−r4 (Weckmann et al., 2012).

enclosing a thin shallow conductive feature (c5). Flanking the Swartberg Mountains to the south, a shallow, south-dipping wedge (r2) with resistivities of $5000\,\Omega\mathrm{m}$ and a thickness of ~ 2 km can be observed. A third resistive structure (r3) extends to ~ 4 km depth beneath the Outeniqua Mountains. The most prominent feature in the model section is the high-conductivity body c1 centered beneath the Oudtshoorn Basin, with resistivity values of less than $1\,\Omega\mathrm{m}$. The well-resolved top of c1 (figure 5.6) lies between 3 km and 4 km below surface and can be traced along a horizontal distance of ~ 40 km. The conductor requires a minimum thickness of $4{\sim}5$ km to fit the data, but the bottoms of conductive structures are poorly resolved because the corresponding part of data is excluded (see figure 5.5). Laterally, c1 clearly reaches far beyond the surface expression of the Oudtshoorn Basin, deepening slightly beneath the Kango inlier to the north. It also extends towards the south beneath the surface outcrops of open-folded Bokkeveld shales, where it appears to terminate along a sub-vertical surface that apparently reaches close to Earth's surface along an inferred steep fault. Several isolated shallow conductive features (c3, c4) are located in the upper 2 km of the crust. These may represent conductive layers in the Cretaceous sediments of the Oudtshoorn Basin. Farther south, a conductive feature (c2, $\sim 10\,\Omega\mathrm{m}$) located beneath the resistive roots of the Outeniqua Mountains at ~ 10 km depth appears to connect to shallower levels at profile kilometer 35.

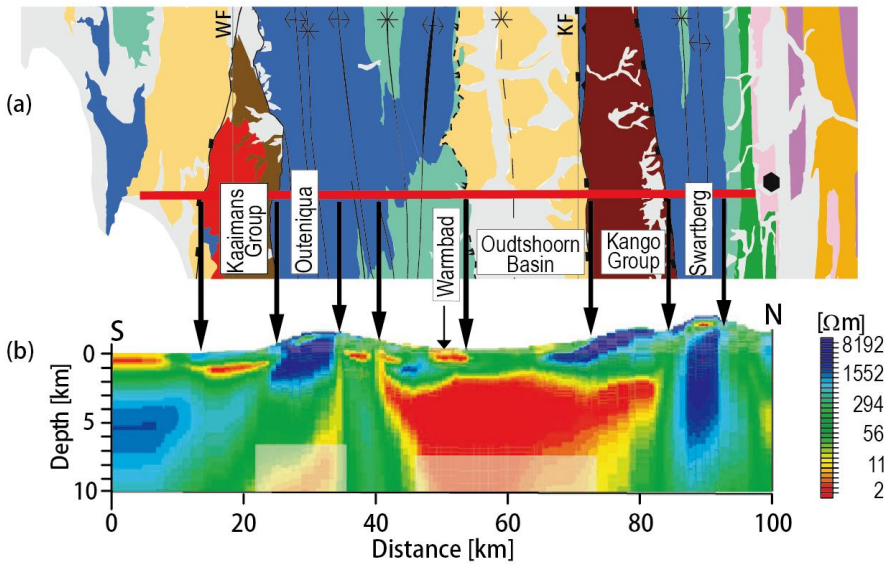

Figure 5.7.: Comparison of (a) the geological map from figure 5.2 with the upper 10 km of the MT resistivity section. Black arrows indicate surface traces of known faults and/or distinct lithological boundaries that correlate with the location of distinct electrical conductivity changes (Weckmann et al., 2012).

Visual comparison between the surface geology and the resistivity image reveals some striking coincidence between lateral variations in electrical conductivity and abrupt changes in the geology (e.g. black arrows in figure 5.7). The Swartberg Mountains, for example, appear in the resistivity section as a sub-vertical resistive zone extending to a depth of 10 km with a shallower wedge of high conductivities (c5 in figure 5.6) that at surface has been mapped as a syncline of Bokkefeld shales. At surface, the geology of this range comprises almost entirely a sub-vertical to steeply overturned section of Table Mountain Group (TMG) quartzites. The Kango inlier appears as a resistive wedge that continues southward to ~ 3 km depth beneath the sediments of the Oudtshoorn Basin that has a stratigraphic thickness of $2\sim 3$ km (Dingle et al., 1983). The Kango rocks are separated from the Oudtshoorn Basin by the Kango Fault. The conductivity model images the Kango fault indirectly as an exchange of different lithologies, and the fault appears to follow a shallow southward dip ($< 20°$) that can be traced down to $2\sim 3$ km. This does not support the Kango Fault being a high angle fault as part of a transpressional flower structure presented by Tankard et al. (2009), or penetrating as deep as 10 km (Stankiewicz et al., 2008). The MT data are also not consistent with a depth extent of the Kango inlier to 8 km as proposed by Tankard et al. (2009). The

Kango Fault clearly dips less steeply than suggested by Paton (2006). The Oudtshoorn Basin is imaged with intermediate ($\sim 40\,\Omega\mathrm{m}$) resistivities to a depth of $2{\sim}3$ km in its center. This is in excellent agreement with geological observations (Dingle et al., 1983). Both the Oudtshoorn Basin and the Kango inlier are underlain by a massive zone of high conductivity, with an upper boundary at $3{\sim}4$ km below surface and from there extending down to at least 7 km depth. To explain the high electrical conductivities, electrically conducting material must be interconnected over large distances. Possible candidates include mineralized phases such as disseminated sulphides or ore deposits. These are common in the Meso-proterozoic crystalline basement Namaqualand (Ryan et al., 1986). However, as the depth to crystalline basement beneath the Oudtshoorn Basin occurs at about $8{\sim}10$ km (Stankiewicz et al., 2008), it remains unlikely that the anomaly occurs in the basement. Alternatively, a thickness of up to 1 km of Bokkeveld shales and ca. 2 km of Peninsula quartzites can be inferred to exist directly beneath the Oudtshoorn Basin, calculated from the anticline/syncline structures in the adjacent Cape Supergroup rock south and east of the basin. The intermediate resistivities in the section are consistent with those of the Bokkeveld shales at the surface, although these are likely to be thin (< 1 km) or even absent beneath the Outdshoorn Basin (Dingle et al., 1983). The observed high-conductivity anomaly therefore most likely lies within the TMG quartzites, which are known to be fractured and to host major aquifers in the vicinity of Oudtshoorn (Umvoto Africa, 2005). In that case, highly fractured TMG and possibly Kango Group quartzites filled with saline fluids could also explain this large, prominent conductive anomaly. Towards the southern end of this anomaly, a sub-vertical conductor reaching close to the surface can be observed. Hot springs exist near the village of Warmbad (i.e. warm-bath, figure 5.7). The shallow patch of high conductivity near the surface could be related to fluids originating at a depth of ~ 1 km, and may be an expression of a fluid pathway along a sub-vertical fault zone connecting to a larger fluid reservoir at greater depth. The Outeniqua Mountains appear as a resistive zone reaching a depth of approximately 5 km. This is in general agreement with structural analyses of Hälbich (1983) that predicts a regional synform, but not with a proposed flower structure (Tankard et al., 2009). Beneath the Outeniqua Mountains, a deep (> 8 km) zone of high electrical conductivity (c2) bound on the north by a sub-vertical structure can be observed that reaches to shallower levels of approximately 5 km depth. To the south, the Kaaimans Group is expressed by intermediate conductivities ($\sim 400\,\Omega\mathrm{m}$) in the upper 1 km of the crust, underlain by a thin layer of high electrical conductivities.

5.3.3. Implication of geo-electrical anisotropy

In previous subsection, it is discovered that a considerable amount of the CFB data can not be fitted using standard 2D inversion procedure, mainly because their phases are greater than $90°$. There are two evidence which imply that the large phase anomaly measured in CFB could caused by electrical anisotropy. First of all, as already discussed in section 3.2.2, some authors suggest that MT phases out of quadrant can be modeled using a combination of two oblique anisotropic structures. Based on that I have also successfully reproduced this phenomenon with similar combination of structures. Secondly, as discussed in previous section, the prominent conductive feature observed beneath the Oudtshoorn basin in Cape Fold Belt is most likely related to the highly fractured Table Mountain Group quartzites. Fractured rocks usually exhibit direction dependency in terms of physical properties due to their fractured nature. According to that, I will examine the possibility of using electrical anisotropy to explain the large phase anomaly observed in CFB.

Isotropic 2D inversion results, as displayed in figure 5.6, are used as background models. For this particular test, I divided the smooth resistivity range into 18 evenly spaced levels and excluded the topography from the model (see figure 5.8). For a first test, the forward responses of the background model are calculated for two purposes: 1) to ensure that such a simplification, e.g. dividing resistivity range into 18 levels, does not change the main property of the model. 2) to examine that the anisotropic forward procedure is correctly implemented with a reliable accuracy. The forward responses are highly comparable with the observed data. As expected, the forward responses do not contain phases greater than $90°$. In the second test, three anisotropic zones are embedded into the background model. Two of them are located in the sediment basin (the Oudtshoorn basin). The one in the left has its top at 800 m beneath the surface and extends to a depth of 2 km and it is anisotropic with $\rho_x, \rho_y, \rho_z = 15, 1, 15\,\Omega\mathrm{m}$ and $\alpha, \beta, \gamma = 120°, 0°, 0°$. The other one in the right has its top at 500 m beneath the surface and extends to a depth with 1.5 km, it is also anisotropic with $\rho_x, \rho_y, \rho_z = 50, 0.5, 50\,\Omega\mathrm{m}$ and $\alpha, \beta, \gamma = 120°, 0°, 0°$. For the third zone I have chosen the prominent conductive feature itself. It is defined also as anisotropic with $\rho_x, \rho_y, \rho_z = 30, 0.3, 30\,\Omega\mathrm{m}$ and $\alpha, \beta, \gamma = 30°, 0°, 0°$. The model is also displayed as figure 5.10. Its forward responses are displayed in figure 5.11. Compare to the observed data shown in figure 5.3, one can see a remarkable agreement, especially in H-polarization. Besides all the features we can also observe phases greater than $90°$ occur in the H-polarization component, which confirms that the large phases observed in CFB can be explained with electrical anisotropy.

Applying the proposed anisotropic inversion method to the CFB data set, I have to face several serious problems. Firstly, a real world (large scale) problem usually requires a fine discretization of model domain. This will dramatically increase the number of model parameters. Currently, the proposed inversion method is based on the Levenberg-Marquardt scheme, which is a Newton-type method and as a requirement, the sensitivity matrix has to be explicitly formed and stored for each inversion iteration. For the CFB data set with a discretized mesh of 235 horizontal and 174 vertical cells, it will produce 245340 model parameters. If we invert 20 periods for all 52 sites will produce 4160 data points. It means, for such a problem 15.2 GB memory is required only for storing the sensitivity matrix. It is impossible to perform such a calculation on a PC. Secondly, as known from previous section, the proposed inversion method is not able to resolve rotation angles. If any angle is involved into inversion, only the effective resisitivies can be resolved (see section 4.3.3). This is equivalent to project different anisotropic properties, defined on different coordinates, onto the basis coordinate on which the model is defined. Since all the effective resistivities are defined on the same coordinate system after projection, the current flow is not forced to change its preferred direction and hence no phases out of quadrant can be observed (see section 4.3.5). However, forward modeling studies with the CFB data have shown that surface electrically anisotropic zones, or highly conductive heterogeneity in near surface range, in combination with a mid-crustal electrically anisotropic zone are required to fit the data. In combination with previous subsection, I may deduce that the current test confirms that the mid-crustal conductive zone is most likely electrically anisotropy and can be interpreted as deep aquifer related to the fractured Table Mountain Group rocks in the Cape Fold Belt.

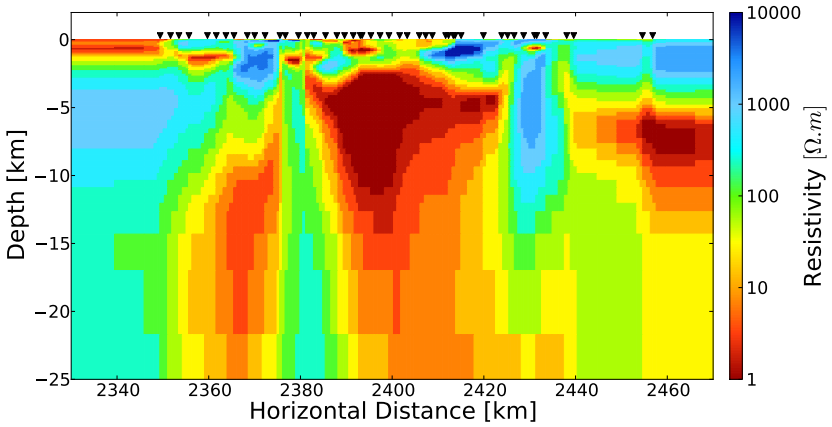

Figure 5.8.: Isotropic 2D inversion results without topography used for anisotropic forward modeling. The resistivity range is divided into 18 levels, which leads to a rougher model than the one displayed in figure 5.6, however, its main features remain.

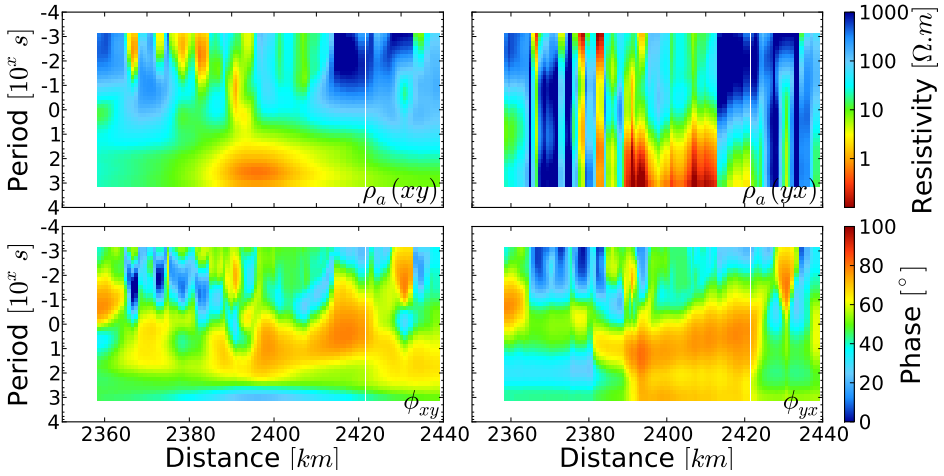

Figure 5.9.: Forward responses calculated using model described in figure 5.8, which are comparable to the pseudo-sections displayed in figure 5.3. No phases greater than 90° occur.

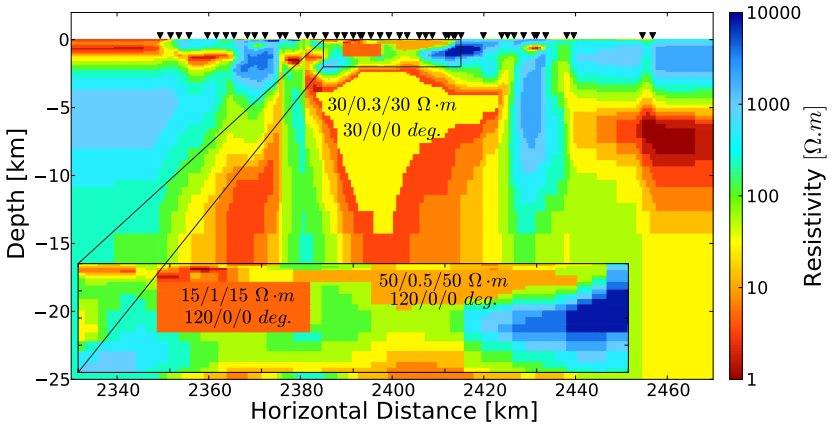

Figure 5.10.: Shallow and deep anisotropic zones are embedded into isotropic 2D inversion results displayed in figure 5.8.

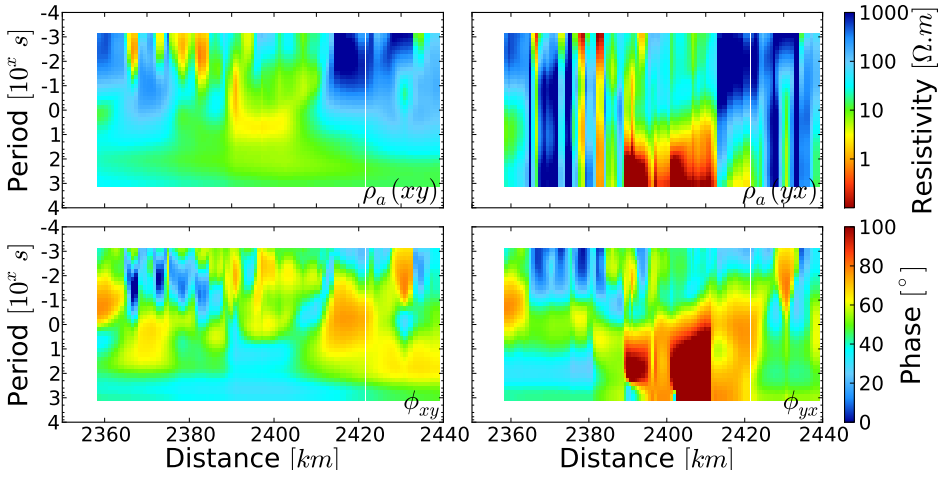

Figure 5.11.: Forward responses calculated using model described in figure 5.10, which are comparable to the pseudo-sections displayed in figure 5.3. Phases greater than 90° are observed in H-polarization.

Chapter 6.

Discussion and conclusions

The proposed inversion method is applied to the interpretation of magnetotelluric (MT) data with consideration of electrical anisotropy. The inverse problem in MT represents in general a non-linear and ill-posed minimization problem with a large number of degrees of freedom even under the assumption of electrical isotropy. Due to electrical anisotropy a tensorial conductivity (or resistivity) distribution in Earth model has to be taken into consideration, which significantly increases the number of degrees of freedom of the inverse problem. In order to successfully invert for anisotropic conductivities, e.g. be able to identify the direction dependency of the conductivities, and also to deal with the non-uniqueness of the solution of the inverse problem it is necessary to use appropriate constraints on the class of allowed models. To accomplish this task I include constraints on the allowed structure, which is measured by the gradient or discretized Laplacian of the model, as well as the allowed anisotropy, measured by the sum of the square difference of the principal conductivity values, of the model (Pain et al., 2003).

The feasibility of anisotropic electrical inversion is demonstrated using simple two-dimensional models. Based on the two-dimensional anisotropic MT forward procedures, forward modeling tests are carried out in order to investigate the limitations of the proposed inversion method. The reason for doing so is straightforward: features which cannot be discerned by forward modeling would be unresolved by inversion. The results show that the forward responses are sensitive to the variations of the principal conductivities defined in horizontal plane while any changes of principal conductivity defined in vertical direction can not be perceived by the forward procedure. This is caused by the assumption of a plane wave diffusion required by magnetotelluric induction and the difficulties to measure the vertical component of the electric field at the Earth's surface. Hence, the vertical component of the principal conductivity is inherently unresolvable. Furthermore, inversion tests are also carried out in order

to examine performance characteristics of the proposed inversion method. The results show that the successful inversion for anisotropic conductivity distributions relies heavily on the application of appropriate constraints. In this thesis I have applied smoothness constraints and anisotropy constraints to the entire model space. Using this approach well resolved model parameters and model parameters that are in the null-space of the inverse problem are both forced to comply with the constraints.

After the objective functional to be minimized is established the major task to ensure a successful anisotropic inversion is to choose appropriate penalty level (or regularization level), e.g. the values of different trade-off parameters, at each iteration of the inversion. For classic 2D isotropic inversion, only one trade-off parameter is needed and the task for gauging of appropriate penalty level becomes searching for the "best" point along a so-called "L-curve", defined by a wide range of trade-off parameter and the resulting RMS error, at which a geologically "reasonable" inversion model is given as well as a relatively low level of the RMS error is reached. For anisotropic inversion two real valued regularization parameters are used as trade-off between data misfit, model roughness and anisotropy, evaluation of appropriate penalty level becomes searching for the "best" point or area on a two-dimensional curved surface, defined by these two regularization parameters and the resulting RMS error. Inversion studies with fixed penalty level are carried out for a wide range of each regularization parameter. The results show that in general the data fit improves while the values of both regularization parameters decrease (Fig. 4.7). A small value of regularization parameter means that the corresponding constraint term has less weight in the objective functional and thus has less influence to the resulting model. Hence, if the values of both trade-off parameters are chosen to be small, the model roughness and the anisotropy constraints become less important, the data misfit is dominant and mainly minimized which will lead to a better data fit. However, using values that are too small for both trade-off parameters will result in over-fitting of the data and back-projection of data errors into the inversion model. This phenomenon can be observed as the artificial features created in the resulting models (Fig. 4.3 to 4.5). When the regularization parameters lie in a range where they are comparable to the initial data misfit, the behavior of the inversion iterations can be described in two phases. In the first phase, which includes the first few iterations, large structure are created and the inversion converges well, while the data misfit falls down to some level where it is smaller than the constraint terms, the inversion goes into the second phase where the regularizations are dominant and in this phase only small scale structure is created. This is an expected behavior. However, using a fixed penalty level usually causes the premature or the post-mature of the inversion, in other words, the inversion usually finishes with either

a smooth inversion model and relatively high RMS error or a rough inversion model and small RMS error. For the first case, the inversion transits too early into the second phase and for the latter case, the transition happens too later or even there is no second phase exists. To overcome this problem, I included a relaxation approach on the penalty level. The basic idea is to start with relatively large values of both regularization parameters, after each successful inversion iteration the parameters relaxes by a factor of two (see Pain et al., 2003, Newman and Hoversten, 2000). The use of the relaxation on the penalty level aims to identify the "optimum" transition of the two phases and achieve the "best" inversion model. It is anticipated that the "optimum" penalty level are encountered somewhere along the way of the relaxation and the inversion process can then be terminated. The results indicate that the inversion with relaxation of penalty parameters produces smooth images and effectively controls the possible premature or post-mature in the inversion process. However, I would like to print out that the initial values of the trade-off parameters still have to be chosen with care. Values that are too small will cause artificial structure in the inversion model, which is the same effect as observed by using a small but fixed penalty level. In contrast, if the initial values are chosen too large, the resulting model is smooth but the inversion will converge significantly slow (Fig. 4.8 to 4.10).

In general, the proposed inversion method is adequate for resolving the principal conductivities defined in horizontal plane. If the rotation angles (e.g. the Euler angles) are involved in the inversion, e.g. the anisotropic coordinate axes on which the principal conductivities are defined do not coincide with the model coordinate axes, only the effective conductivities, e.g. the values projected from the anisotropic coordinate to the coordinate on which the model is defined, can be resolved and hence the inverted rotation angles are insignificantly small (Fig. 4.11 and 4.12). Synthetic inversion tests are also carried out in order to examine the capability to deal with data set containing phases out of quadrant which is typically indicative of electrical anisotropy. My tests are based on the forward response of a model with two anisotropic structures of oblique anisotropy strike directions (see Pek and Verner, 1997, Heise and Pous, 2003, Weckmann et al., 2003). The inversion results show that the structures which produce the anomalous phases can not be fully reconstructed by the proposed inversion method. However, a remarkable degree of similarity can be observed from the true model and the inversion model. The data fit reveals a great agreement in apparent resistivity, while the same effect can also be observed in phase as long as the phases of "real" data stay inside the first quadrant. When the phases of "real" data go into the second quadrant, the phases of the predicted data approximate 90° but will never be greater than it. A possible explanation for this is that the proposed inversion method can only resolve the

effective conductivities defined on the coordinate on which the model is defined and hence lose the information about the rotation angles. This is equivalent to a projection of different anisotropic properties, defined on different coordinates, onto the basis coordinate on which the model is defined. Since all the effective resistivities are defined on the same coordinate system after projection, the current flow is not forced to change its preferred direction and hence no phases out of quadrant can be observed.

Currently, the proposed inversion method is implemented into a numerical finite volume framework and embedded in the ModEM modeling and inversion software package (Egbert and Kelbert, 2012). The philosophy behind the ModEM is a generally applicable set of forward modeling, inversion and auxiliary routines which can be extended by more specific applications. For minimization I use the Levenberg-Marquardt method and which is based on the well-known Gauss-Newton method. The sensitivity matrix is defined as the first derivative of predicted data with respect to model parameters and describes how sensitive the predicted data are towards a small changes in the model parameters. The calculation of the sensitivity matrix is the key point for almost all inversion methods, especially for the Newton type method. In the anisotropic case, the electrical property of each grid cell has to be defined with a symmetric second-order tensor and for practical reason its representatives (the principal values and the Euler angles) are used for all numerical calculation instead of the tensor itself. Hence, the calculation of the sensitivity matrix is not as straightforward as it in isotropic case. In this thesis, I present an algorithm which is adequate to calculate the sensitivity matrix for an anisotropic conductivity distribution. As a requirement of Newton based methods, the sensitivity matrix for each inversion iteration has to be explicit formed and stored. The storage of the approximated Hessian matrix can be avoided by implementing of a matrix-vector multiplication procedure. This results in a remarkable memory savings over the traditional Gauss-Newton approach. Even so the storage of the sensitivity matrix already makes the implemented procedure inadequate for large-scale problems.

The MT data set taken in the Cape Fold Belt in South Africa exhibits an area (> 10 km) where MT phases over $90°$. This part of data can not be modeled by standard isotropic modeling procedure and hence can not be properly interpreted. The proposed inversion method, however, could not reproduce the anomalous large phases as desired because of losing the information about rotation angles. MT phases outside the first quadrant are usually obtained by different anisotropic anomalies with oblique anisotropy strike. In order to achieve this challenge, the algorithm needs further developments. However, forward modeling studies with the MT data have shown that surface highly conductive heterogeneities in combination with a mid-crustal electrically anisotropic zone are required to fit the data. According to

known geological and tectonic information the mid-crustal zone is interpreted as a deep aquifer related to the fractured Table Mountain Group rocks in the Cape Fold Belt.

Much works remain to be done to make the procedure practical for realistic data and Earth models. The improvement of anisotropic inversion algorithm, especially for magnetotelluric data, should involve the following tasks:

1. Extending the procedure so that the diagonal elements of the impedance tensor and/or the apparent resistivity and the phase can be fit.
2. Defining and applying "appropriate" constraints to ensure successful inversion.
3. Exploring the range of equivalent results for electrical anisotropy.
4. Developing of the algorithm which is adequate to resolve the Euler angles required by the diagonalization of the second order conductivity/resistivity tensor.
5. Reducing of computational cost without loss of computational accuracy, e.g. acceleration of computational algorithm (Approximate from of sensitivity, data space inversion) or parallel computing.
6. 3D anisotropic inversion using appropriate constraints.

Chapter 7.

Acknowledgements

Many people, directly or indirectly, were involved in my work over the course of the past years and without their inspiration, contribution and help, I would not have been able to write these final pages of my thesis at this moment.

In particular, I am heartily thankful to my supervisor, Dr. Ute Weckmann, for her encouragement, support, supervision and endless patience over all the years. Dr. Weckmann supervised my PhD-work and supported me from the early to the concluding stages. She encouraged me to work on a broad range of topics while providing the freedom to pursue my own ideas. The instructive discussions with Dr. Weckmann helped me to gain a deeper insight into the MT method. Besides all these, she also supported me to participate in national and international conferences, which provides me a great opportunity to network with other colleagues and learn from experienced scientists.

I am very grateful to PD Dr. Oliver Ritter, who contributed a lot to my understanding of analyzing and interpretation of magnetotelluric data, which is instructional for the entire work. My special thanks goes to Dr. Michael Becken, who gave me an opportunity to finish my diploma thesis with him in the MT group at the GFZ and hence guided me into the door of magnetotelluric. From Dr. Becken I have learned the theoretical background of MT. He also taught me how to deal with MT instrument and how to process the MT data during my first MT field campaign. I am also grateful to Dr. Naser Meqbel for his kindness and patience. During these years I had uncountable discussions with him, mainly about theoretical and practical details of MT inversion. Dr. Meqbel was always obliging and patient with me. The developing of the proposed method and its implementation were guided by his long experience in numerical modeling and inversion.

I am especially grateful to Dr. Josef Pek at Czech Academy of Sciences (Prague), who contributed a lot to my understanding of anisotropic modeling and inversion. His articles, computer programs and numerous personal discussions during conferences and workshops, helped me to penetrate many theoretical and numerical details about anisotropic modeling and inversion. Dr. Pek also spent one-week of his valuable time to visit the MT group at GFZ. During that time I had the chance to show him my work systematically. His opinions and suggestions not only helped me to improve my work but also boosted my confidence. In the course of my PhD work, Dr. Weckmann provided me the opportunity to work with Prof. Dr. Gary Egbert at Oregon State University (Corvallis, USA) for six weeks. During that time I had numerous constructive discussions with Prof. Egbert and which helped me to gain a deeper insight into the field of numerical modeling and inversion. I am grateful to Prof. Egbert for his patience. In this respect I would also like to thank Dr. Anna Kelbert for many useful discussions and suggestions during my stay in Corvallis.

I would like to heartfelt thank all my colleagues at the GFZ; the collaboration with them was of utmost importance for the preparation of my thesis. They shared their knowledge and made many helpful suggestions. Whenever I have problem involved numerical details and it's implementation, Dr. Rita Streich was my direct contact person and she is always patient with me and all my questions. From Dr. Gerard Munoz I obtianed numerous small and quick tips for data processing and inverting. With Dipl. Geophysicist Kristina Tietze I enjoyed to discuss about theoretical and practical nodus. My office-mates Dipl. Geophysicist Sissy Kütter and Dipl. Physicist Paul Saß were my direct sources for quick tips and Sissy has spent a lot of her free time to help me to translate the summary into German. With Msc. Geophysicist Alexander Grayver I enjoyed to discuss about the details of EM inversion techniques. Many thanks go to all other members of the MT-team at the GFZ and to the colleagues from the Free University of Berlin and University of Potsdam for many fruitful discussions in our MT-AG meeting.

Beyond geophysics, I enjoyed support of manifold type and also interest in my work from my family for the whole period of studies and during the PhD time. I wish to thank my wife Nan, who had uncomplainingly accepted, that I have been in the field for several times, each time several weeks or even months. Without Nan's understanding, patience and encouragement I could not have done this work. I am deeply grateful to her.

Finally, I would like to thank the German Research Foundation (Deutsche Forschungsgemeinschaft (DFG) for the funding of this research. I would also like to thank the IAGA (WGI.2: Electromagnetic Induction in the Earth) for providing me a financial support, so that I was

able to attend the 20st EM induction workshop.

List of Figures

Bibliography

Abramovici, F. (1974). The forward magnetotelluric problem for an inhomogeneous and anisotropic structure, Geophysics **39**(1): 56–68.

Baba, K., Chave, A. D., Evans, R. L., Hirth, G. and Mackie, R. L. (2006). Mantle dynamics beneath the East Pacific Rise at 17° S: Insights from the Mantle Electromagnetic and Tomography (MELT) experiment, Journal of Geophysical Research **111**(B2): 1–18.
URL: *http://www.agu.org/pubs/crossref/2006/2004JB003598.shtml*

Bahr, K., Smirnov, M., Steveling, E. and Working group, B. (2002). A gelation analogy of crustal formation derived from fractal conductive structures, Journal of Geophysical Research **107**(B11): 1–10.
URL: *http://www.agu.org/pubs/crossref/2002/2001JB000506.shtml*

Barnett, W., Armstrong, R. A. and de Wit, M. J. (1997). Stratigraphy of the upper neoproterozoic Kango and lower paleozoic Table Mountain Group of the Cape Fold Belt revisited, S. Afr. J. Geol. **100**: 237–250.

Becken, M. and Burkhardt, H. (2004). An ellipticity criterion in magnetotelluric tensor analysis, Geophysical Journal International **159**(1): 69–82.
URL: *http://doi.wiley.com/10.1111/j.1365-246X.2004.02376.x*

Booth, P. (2011). Stratigraphic, structural and tectonic enigmas associated with the Cape Fold Belt: challenges for the future, S. Afr. J. Geol., Inkaba yeAfrica Special volume 2. **114**: 235–248.

Brown, L., Jr Benson, J., Brink, G., Doherty, S., Jollands, A., Jungslager, E., Keenan, J., Muntingh, A. and van Wyk, N. (1995). Sequence Stratigraphy in Offshore South African Divergent Basins: An Atlas on Exploration for Cretaceous Lowstand Traps by Soekor (Pty) Ltd, Vol. 41, AAPG Studies in Geology.

Cagniard, L. (1953). Basic theory of the magnetotelluric method of geophysical prospecting, Geophysics **18**: 605–635.

Claerbout, J. and Muir, F. (1973). Robust modeling with erratic data, Geophysics **38(1)**: 826–844.

Constable, S. C., Parker, R. L. and Constable, C. G. (1987). Occam's inversion: A practical algorithm for generating smooth models from electromagnetic sounding data, Geophysics **52**(3): 289–300.
URL: *http://linkinghub.elsevier.com/retrieve/pii/0021999188900629*

De Beer, C. H. (1992). Inversion Tectonics of the Cape Fold Belt, Karoo and Cretaceous Basins of Southern Africa, Balkema, Rotterdam, Netherlands, chapter Structural evolution of the Cape Fold Belt syntaxis and its influence on syntectonic sedimentation in the SW Karoo Basin, pp. 197–206.

de Wit, M. J., Stankiewicz, J. and Reeves, C. (2008). West Gondwana: Pre-Cenozoic Correlations Across the South Atlantic Region, Geological Society, London, Special Publications, chapter Restoring Pan-African-Brasiliano connections: more Gondwana control, less Trans-Atlantic corruption, pp. 399–412.

DeGroot-Hedlin, C. and Constable, S. (1990). Occam's inversion to generate smooth, two-dimensional models from magnetotelluric data, Geophysics **55**(12): 1613–1624.
URL: *http://link.aip.org/link/?GPY/55/1613/1&Agg=doi*

Dingle, R. V., Siesser, W. G. and Newton, A. R. (1983). Mesozoic and Tertiary Geology of Southern Africa, A. A. Balkema, Rotterdam.

Egbert, G. (2006). Efficient inversion of multi-frequency and multi-source electromagnetic data, Technical report, College of Oceanic and Atmospheric Sciences, Oregon State University.

Egbert, G. D. (1990). Comments On "Concerning dispersion relations for the magnetotelluric impedance tensor" By E. Yee and K. V. Paulson, Geophysical Journal International **102**(1): 1–8.
URL: *http://doi.wiley.com/10.1111/j.1365-246X.1990.tb00525.x*

Egbert, G. D. and Kelbert, A. (2012). Computational recipes for electromagnetic inverse problems, Geophys. J. Int. .

Eisel, M. and Bahr, K. (1993). Electrical anisotropy in the lower crust of an interpretation of a magnetotelluic profile after tensor decomposition, J. Geomag. Geoelectr. **45**: 1115–1126.

Eisel, M. and Haak, V. (1999). Macro-anisotropy of the elastical conductivity of the crust: a magnetotelluic study of the german continental deep drilling site (ktb), Geophys. J. Int. **136**: 109–122.

EMSLAB-Group (1988). The emslab electromagnetic sounding experiment, EOS, Trans. Am. Geophys. Un. **69**: 89–91.

Farquharson, C. G. and Oldenburg, D. W. (1998). Non-linear inversion using general measures of data misfit and model structure, Geophysical Journal **134**: 213–227.

Fildani, A., Wieislogel, A., Drinkwater, N. J., McHargue, T., Tankard, A., Wooden, J., Hodgson, D. and Flint, S. (2009). U-Pb Zircon ages from the south-western Karoo Basin, South Africa – Implications for the Permian-Triassic boundary, Geology **37**: 719–722.

Golub, G. and Van Loan, C. (1996). Matrix Computations, Johns Hopkins University Press, London.

Günther, T. (2004). Inversion Methods and Resolution Analysis for the 2D/3D Reconstruction of Resistivity Structures from DC Measurements, PhD thesis, Fakultät für Geowissenschaften, Geotechnik und Bergbau der Technischen Universität Bergakademie Freiberg.

Hälbich, I. W. (1983). Geodynamics of the Cape Fold Belt, Geological Society of South Africa, Johannesburg, South Africa. Special Publication No.12., chapter A geodynamic model for the Cape Fold Belt, pp. 177–184.

Hansen, P. (1992). Regularization tools - a matlab packager for analysis and solution of discrete ill-posed problems. `http://www.imm.dtu.dk/~pch`.

Hansen, P. C. (1998). Rank-Deficient and Discrete Ill-Posed Problems: Numerical Aspects of Linear Inversion, Society for Industrial and Applied Mathematics, Philadelphia.

Heise, W. and Pous, J. (2001). Effects of anisotropy on the two-dimensional inversion procedure, Geophysical Journal International **147**(3): 610–621.
URL: *http://doi.wiley.com/10.1046/j.0956-540x.2001.01560.x*

Heise, W. and Pous, J. (2003). Anomalous phases exceeding 90° in magnetotellurics: anisotropic model studies and a field example, Geophysical Journal International

155(1): 308–318.
URL: *http://doi.wiley.com/10.1046/j.1365-246X.2003.02050.x*

Hestenes, C. and Stiefel, E. (1952). Methods of conjugate gradients for solving linear systems, J. Res. Nat. Bur. Stand **49**: 409–436.

Ichihara, H. and Mogi, T. (2009). A realistic 3-D resistivity model explaining anomalous large magnetotelluric phases: the L-shaped conductor model, Geophysical Journal International **179**(1): 14–17.
URL: *http://blackwell-synergy.com/doi/abs/10.1111/j.1365-246X.2009.04310.x*

Johnson, M. R., Van Vuuren, C. J., Visser, J. N. J., Cole, D. I., de Wickens, H. V., Christie, A. D. M. and Roberts, D. L. (1997). Sedimentary Basins of the World, African Basins, Amsterdam, The Netherlands., chapter The foreland Karoo Basin, South Africa, pp. 269–317.

Johnston, S. T. (2000). The Cape Fold Belt and Syntaxis and the rotated Falkland Islands: dextral transpressional tectonics along the southwest margin of Gondwana, J. Afr. Earth Sci. **31**: 51–63.

Jones, A. G., Evans, R. L. and Eaton, D. W. (2009). Velocity-conductivity relationships for mantle mineral assemblages in archean cratonic lithosphere based on a review of laboratory data and hashin-shtrikman extremal bounds, Lithos **109**: 131–143.

Leibecker, J., Gatzemeier, A., Hönig, M., Kuras, O. and Soyer, W. (2002). Evidence of electrical anisotropic structures in the lower crust and the upper mantle beneath the Rhenish Shield, Earth and Planetary Science Letters **202**(2): 289–302.
URL: *http://linkinghub.elsevier.com/retrieve/pii/S0012821X02007835*

Levenberg, K. (1944). A method for the solution of certain non-linear problems in least squares, Quart. Appl. Math. **2**: 164–168.

Lezaeta, P. (2001). Distortion analysis and 3-D modelling of magnetotelluric data in the Southern Central Andes, PhD thesis, Inst. für Geol. Geoph. und Geoinform., Freie Universität Berlin.

Li, Y. (2000). Numerische Modellierungen von elektromagnetischen Feldern in 2- und 3-dimensionalen anisotropen Leitfähigkeitsstrukturen der Erde nach der Methode der finiten Elemente, PhD thesis, Universität Göttingen.

Li, Y. (2002). A finite-element algorithm for electromagnetic induction in two-dimensional anisotropic conductivity structures, Geophysical Journal International **148**: 389–401.

Li, Y., Pek, J. and Brasse, H. (2003). Magnetotelluric inversion for 2D anisotropic conductivity structures, in Proceedings of the 22th Colloquium on Deep Electromagnetic Sounding, Königstein.

Lindeque, A., de Wit, M. J., Ryberg, T., Weber, M. and Chevallier, L. (2011). Deep crustal profile across the southern Karoo Basin and Beattie Magnetic Anomaly, South Africa: an integrated interpretation with tectonic implications., S. Afr. J. Geol. **114**: 265–292.

Livelybrooks, D., Mareschal, M., Blais, E. and Smith, J. (1996). Magnetotelluric delineation of the Trillabelle massive sulfide body in Sudbury, Ontario, Geophysics **61**: 971–986.

Loewenthal, D. and Landisman, M. (1973). Theory for magnetotelluric observation on the surface of a layered anisotropic half-space, Geophys. J.R. astr. Soc. **35**: 195–214.

Mackie, R. L. and Madden, T. R. (1993a). Conjugate direction relaxation solutions for 3-D magnetotelluric modeling, Geophysics **58**(7): 1052–1057.
URL: *http://link.aip.org/link/?GPY/58/1052/1&Agg=doi*

Mackie, R. L. and Madden, T. R. (1993b). Three-dimensional magnetotelluric inversion using conjugate gradients, Geophysical Journal International **115**: 215–229.
URL: *http://www.ncbi.nlm.nih.gov/pubmed/21638006*

Madden, T. and Nelson, P. (1963). A defense of Cagniard's magnetotelluric method, Technical report, Report for Office of Naval Research. Published in Vozoff (1966), pages 89 - 95.

Mareschal, M., Kellett, R. L., Kurtz, R. D., Ludden, J. N., Ji, S. and Beiley, R. C. (1995). Archean cratonic roots, mantle shear zones and deep electrical anisotropy, Nature **375**: 134–137.

Marquardt, D. W. (1963). An algorithm for least-squares estimation of nonlinear parameters, J. Soc. Indust. Appl. Math. **11**: 431–441.

Meqbel, M. N. (2009). The electrical conductivity structure of the Dead Sea Basin dervied from 2D and 3D inversion of magnetotelluic data, PhD thesis, Fachbereich Geowissenschaften der Freien Universität Berlin.

Miensopust, M. P. and Jones, A. G. (2011). Artefaces of isotropic inversion applied to magnetotelluic data from an anisotropic earth, Geophys. J. Int. **187**: 677–689.

Milani, E. J. and de Wit, M. J. (2008). West Gondwana: Pre-Cenozoic Correlations Across the South Atlantic Region, Geological Society, London, Special Publications, chapter Correlations between classic Parana and Cape-Karoo basins of South America and southern Africa and their basin infills flanking the Gondwanides: Du Toit revisited., pp. 319–342.

Newman, G. a. and Alumbaugh, D. L. (2000). Three-dimensional magnetotelluric inversion using non-linear conjugate gradients, Geophysical Journal International **140**(2): 410–424. **URL:** *http://doi.wiley.com/10.1046/j.1365-246x.2000.00007.x*

Newman, G. a. and Boggs, P. T. (2004). Solution accelerators for large-scale three-dimensional electromagnetic inverse problems, Inverse Problems **20**(6): S151–S170.

Newman, G. A. and Hoversten, G. M. (2000). Solution strategies for two- and three-dimensional electromagnetic inverse problems, Inverse Problems **16**: 1357–1375.

Newton, A. R., Shone, R. W. and Booth, P. W. K. (2006). The Geology of South Africa, Geological Society of South Africa Council for Geoscience, Johannesburg/Pretoria, South Africa., chapter The Cape Fold Belt, pp. 521–530.

Nocedal, J. and Wright, S. (1999). Numeric Optimization, Operations Research, springer.

O'Brien, D. P. and Morrison, H. F. (1967). Electromagnetic Fields in an N-layer anisotropic half-space, Geophysics **XXXII**(4): 668–677.

Onsager, L. (1931). Reciprocal relations in irreversible processes, Phys. Rev. **37**: 405–426.

Osella, A. M. and Martinelli, P. (1993). Magnetotelluric response of anisotropic 2-d structures, Geophys. J. Int. **115**: 819–828.

Pain, C. C., Herwanger, J. R. V., Saunders, J. H., Worthington, M. H. and Oliveira, C. R. E. D. (2003). Anisotropic resistivity inversion, Inverse Problems **19**(5): 1081–1111.

Parsiegla, N., Stankiewicz, J., Gohl, K., Ryberg, T. and Uenzelmann-Neben, G. (2009). Southern African continental margin: dynamic processes of a transform margin, Geochem. Geophy. Geosy. **10**: Q03007. doi:10.1029/2008GC002196.

Paton, D. (2006). Influence of crustal heterogeneity on normal fault dimensions and evolution: southern South Africa extensional system, Journal of Structural Geology **28**(5): 868–886. **URL:** *http://linkinghub.elsevier.com/retrieve/pii/S0191814106000204*

Pek, J. and Santos, F. A. M. (2002). Magnetotelluric impedances and parametric sensitivities for 1-D anisotropic layered media, Computers & Geosciences **28**(8): 939–950.
URL: *http://linkinghub.elsevier.com/retrieve/pii/S0098300402000146*

Pek, J. and Verner, T. (1997). Finite-difference modelling of magnetotelluric fields in two-dimensional anisotropic media, Geophysical Journal International **128**(3): 505–521.
URL: *http://doi.wiley.com/10.1111/j.1365-246X.1997.tb05314.x*

Pous, J., Heise, W., Schnegg, P., Munoz, G., Martí, J. and Soriano, C. (2002). Magnetotelluric study of the las canadas caldera (tenerife, canary islands): structural and hydrogeological implications, Earth planet. Sci. Lett. **204**: 249–263.

Pratt, R. G. and Chapman, C. P. (1992). Traveltime tomography in anisotropic media - ii. application, Geophys. J. Int. **109**: 20–37.

Price, A. T. (1962). The theory of magnetotellur methods when the source field is considered, Journal of Geophysical Research **67**: 1907–1918.

Reddy, I. K. and Rankin, D. (1975). Magnetotelluric response of laterally inhomogeneous and anisotropic media, Geophysics **40**(6): 1035–1045.

Reddy, I. and Rankin, D. (1970). Magnetotelluric Effect of Dipping Anisotropies, Geophysical Prospecting **XIX**(June): 84–97.

Reeves, C. and de Wit, M. J. (2000). Making ends meet in Gondwana: retracing the transforms of the Indian Ocean and reconnecting continental shear zones, Terra Nova **12**: 272–280.

Ritter, O., Junge, A. and Dawes, G. (1998). New equipment and processing for magnetotelluric remote reference observations, Geophysical Journal International **132**(3): 535–548.
URL: *http://doi.wiley.com/10.1046/j.1365-246X.1998.00440.x*

Rodi, W. L. (1976). A Technique for Improving the Accuracy of Finite Element Solutions for Magnetotelluric Data, Geophys. J. R. astr. Soc. **44**(2): 483–506.
URL: *http://doi.wiley.com/10.1111/j.1365-246X.1976.tb03669.x*

Rodi, W. and Mackie, R. L. (2001). Nonlinear conjugate gradients algorithm for 2-D magnetotelluric inversion, Geophysics **66**(1): 174–187.
URL: *http://link.aip.org/link/GPYSA7/v66/i1/p174/s1&Agg=doi*

Ryan, P., Lawrence, A., Lipson, R., Moore, J., Paterson, A., Stedman, D. and Van Zyl, D. (1986). Mineral Deposits of Southern Africa, Special Publication of the Geological Society of South Africa, Johannesburg, South Africa., chapter The Aggeneys base metal sulphide deposits, Namaqualand district, pp. 1447–1474.

Saraf, P. D., Negi, J. and Červ, V. (1986). Magnetotelluric response of a laterally inhomogeneous anisotropic inclusion, Phys. Earth Planet. Inter. **43**: 196–198.

Schmucker, U. (1994). 2-d model computations of the induction in nhomogeneous thin sheets above anisotropic layered half-spaces, Proceding of the Colloquium on Deep Electromagnetic Sounding, pp. 3-26, eds. Bahr, K. and Junge, A., German Geophysical Society, Potsdam (in German).

Shewchuk, J. R. (n.d.). An introduction to the conjugate gradient method without the agonizing pain. 1994.
URL: *http://www.cs.cmu.edu/ quake-papers/painless-conjugate-gradient.pdf*

Shone, R. W., Nolte, C. C. and Booth, P. W. K. (1990). Pre-Cape rocks of the Gamtoos area - a complex tectono-stratigraphic package preserved as a horst block, S. Afr. J. Geol. **93**: 616–621.

Simpson, F. and Bahr, K. (2005). Practical Magnetotellurics, Cambridge University Press.

Siripunvaraporn, W., Egbert, G., Lenbury, Y. and Uyeshima, M. (2005). Three-dimensional magnetotelluric inversion: data-space method, Physics of The Earth and Planetary Interiors **150**(1-3): 3–14.
URL: *http://linkinghub.elsevier.com/retrieve/pii/S0031920104003590*

Stankiewicz, J., Parsiegla, N., Ryberg, T., Gohl, K., Weckmann, U., Trumbull, R. and Weber, M. (2008). Crustal structure of the southern margin of the African Plate: results from geophysical experiments, J. Geophys. Res. **113**: B103103, doi:10.1029/2008JB005612.

Tankard, A., Welsink, H., Aukes, P., Newton, R. and Stettler, E. (2009). Tectonic evolution of the Cape and Karoo basins of South Africa, Marine and Petroleum Geology **26**(8): 1379–1412.
URL: *http://linkinghub.elsevier.com/retrieve/pii/S026481720900049X*

Tarantola, A. (1978). Inverse Problem Theory, Elsevier, Amsterdam.

Tietze, K., Weckmann, U., Hübert, J. and Ritter, O. (2007). MT measurements in the Cape Fold Belt, South Africa, poster presented on the 22th Colloquium on Deep Electromagnetic Sounding, Děčín, Czech Republic.

Tikhonov, A. N. (1950). The determination of electrical properties of the deep layers of the earth's crust, Dokl. Acad. Nauk. SSR **73**: 295–297. In russian.

Tikhonov, A. N. and Arsenin, V. Y. (1977). Solutions of ill-posed problems, V. H. Winston & Sons.

Umvoto Africa (2005). Deep artesian groundwater for the Oudtshoorn municipal supply, Technical report, Water Research Commission, WRC Report No. 1254/1/05.

Vozoff, K. (1972). The magnetotelluric method in hte exploration of sedimentary basins, Geophysics **37**: 98–141.

Wait, J. R. (1954). On the relation between telluric currents and the earth's magnetic field, Geophysics **19**: 281–289.

Wannamaker, P. E., Stodt, J. a. and Rijo, L. (1987). A stable finite element solution for two-dimensional magnetotelluric modelling, Geophys. J. R. astr. Soc. **88**(1): 277–296. **URL:** *http://doi.wiley.com/10.1111/j.1365-246X.1987.tb01380.x*

Ward, H. S. and Hohmann, G. W. (1987). Electromagnetic Methods in Applied Geophysics: Volume 1, Theory, SEG, chapter Electromagnetic Theory for Geophysical Applicaitons, pp. 131–308.

Weaver, J. (1994). Mathematical methods for geo-electromagnetic induction, Research Studies Press (Taunton, Somerset, England and New York).

Weckmann, U. (2002). Entwicklung eines Verfahrens zur Abbildung krustaler Leitfähigkeitsstrukturen anhand der Magnetotellurik Daten aus Namibia, PhD thesis, Inst. für Geol. Geoph. und Geoinform., Freie Universität Berlin.

Weckmann, U. (2005). Phase Splitting: Evidence for mantle anisotropy?, Proceding of the 21th Colloquium on Deep Electromagnetic Sounding, Haus Wohldenberg.

Weckmann, U., Ritter, O., Chen, X., Tietze, K. and de Wit, M. J. (2012). Magnetotelluric image linked to surface geology across the Cape Fold Belt, South Africa, Terra Nova **24**: 207–212.

Weckmann, U., Ritter, O. and Haak, V. (2003). A magnetotelluic study of the Damara Belt in Namibia. 2. MT phases over 90° reveal the internal structure of the Waterberg Fault/Omaruru Lineament, Phys. Earth Planet. Inter. **138**: 91–112.

Weidelt, P. (1999). 3-d conductivity models: Implications of electrical anisotropy, in M. Oristaglio and B. Spies (eds), Three-dimensional Electromagnetics, Geohpys. Dev. Series, 7, SEG, Tulsa, OK, pp. 119–137.

Wiese, H. (1962). Geomagnetische Tiefentellurik Teil: II. die Streichrichtung der Untergrundstrukturen des elektrischen Widerstandes, erschlossen aus geomagnetischen Variationen, Geofis. Pura Appl. **52**: 82–103.

Appendix A.

A.1. Theoretical assumptions for magnetotellurics

In order to derive and solve the induction equation that forms the theoretical basis of magnetotellurics, following assumptions are made:

1. All electromagnetic sources are outside the Earth. The natural electromagnetic source field used in magnetotellurics is generated by large-scale ionospheric current systems. The origin of these current systems is far away from the Earth's surface so that the electromagnetic fields can be treated as uniform, plane-polarized waves impinging on the Earth at near-vertical incidence. This assumption is the most important one for magnetotellurics and has first been used by Tikhonov (1950) and Cagniard (1953), its validity has been discussed by Price (1962) and Madden and Nelson (1963). For electromagnetic plane waves, the electric field $\mathbf{E}$ and the magnetic field $\mathbf{B}$ with amplitude $\mathbf{E_0}$ and $\mathbf{B_0}$ at the origin and the angular frequency ω have the mathematical form:

$$\mathbf{E} = \mathbf{E_0} e^{i\omega t} \tag{A.1}$$

$$\mathbf{B} = \mathbf{B_0} e^{i\omega t} \tag{A.2}$$

2. For Earth materials we can assume the conventional linear relationships between the electric displacement $\mathbf{D}$ and the electric field $\mathbf{E}$, the magnetic induction $\mathbf{B}$ and the magnetic field strength $\mathbf{H}$:

$$\mathbf{D} = \varepsilon_0 \varepsilon_r \mathbf{E} \tag{A.3}$$

$$\mathbf{B} = \mu_0 \mu_r \mathbf{H} \tag{A.4}$$

where $\varepsilon_0 = 8.85 \cdot 10^{-12}\,\mathrm{As/Vm}$ and $\mu_0 = 4\pi \cdot 10^{-7}\,\mathrm{Vs/Am}$ are two universal constants, called the dielectric permittivity of free space and magnetic permeability of free space,

ε_r and μ_r are the relative dielectric permittivity and the relative magnetic permeability, respectively. For magnetotellurics, changes in dielectric permittivities and magnetic permeabilities can be neglected, so equations (A.3) and (A.4) can be simplified to:

$$\mathbf{D} = \varepsilon_0 \mathbf{E} \tag{A.5}$$

$$\mathbf{B} = \mu_0 \mathbf{H} \tag{A.6}$$

3. The Earth acts as an ohmic conductor so that current density $\mathbf{J}$ and electric field $\mathbf{E}$ are linearly related through Ohm's Law by the electrical conductivity σ (in S/m):

$$\mathbf{J} = \sigma \mathbf{E} \tag{A.7}$$

4. Displacement currents $\partial \mathbf{D}/\partial t$ are assumed to be negligible. Most magnetotelluric surveys use frequencies between $10,000 - 0.0001\,\mathrm{Hz}$. Given typical resistivities of the Earth of $10^6 - 10^{-2}\,\Omega\mathrm{m}$ we can compare the terms in equation (2.2),

$$\frac{\partial \mathbf{D}/\partial t}{\mathbf{J}} = \frac{i\omega\varepsilon_0}{\sigma} \approx 0.1 - 10^{-19} \tag{A.8}$$

For the highest frequencies in extremely resistive areas displacement currents are an order of magnitude smaller than the current density and we would start to see some effects from these currents. Typically both the measurement frequencies and the resistivities will be much smaller and we will not see any effect.

A.2. Induction equation in different dimensionalities

A.2.1. Layered half-space: one-dimensional structures

Consider a structure consisting of a number of layers overlying a homogeneous half-space. We choose a system of orthogonal right-handed Cartesian coordinates (x, y, z) with z positive downward and the xy-plane with $z = 0$ coincides with the Earth-Air interface. The components of the conductivity tensor depend upon depth z in all the layers and are constant in the half-space. In this case the EM-fields in the horizontal xy-plane can be treated as homogenous which means the partial derivatives of the electric and magnetic fields with respect to x and y are significantly small and hence negligible comparing with the partial derivative of the fields with respect to z, i.e., $\partial/\partial x = \partial/\partial y = 0$.

Assuming a part of the structure (one or more of the layers) is anisotropic. The Maxwell's equations (2.15) and (2.16) in each of the layers for a frequency ω reduce to:

$$\begin{aligned}
\frac{\partial E_x}{\partial z} &= -i\omega\mu_0 H_y && \text{(A.9)}\\
\frac{\partial E_y}{\partial z} &= i\omega\mu_0 H_x && \text{(A.10)}\\
\frac{\partial H_y}{\partial z} &= -\sigma_{xx}E_x - \sigma_{xy}E_y - \sigma_{xz}E_z && \text{(A.11)}\\
\frac{\partial H_x}{\partial z} &= \sigma_{yx}E_x + \sigma_{yy}E_y + \sigma_{yz}E_z && \text{(A.12)}\\
0 &= \sigma_{zx}E_x + \sigma_{zy}E_y + \sigma_{zz}E_z && \text{(A.13)}\\
H_z &= 0 && \text{(A.14)}
\end{aligned}$$

Equations (A.13) and (A.14) express simply the absence of the vertical magnetic field and of vertical electric currents anywhere in the anisotropic layered medium. In contrast to that equation (A.13) also implies the existence of a vertical component of electric field:

$$E_z = -\frac{\sigma_{zx}}{\sigma_{zz}}E_x - \frac{\sigma_{zy}}{\sigma_{zz}}E_y \qquad \text{(A.15)}$$

From equations (A.9) and (A.10) the horizontal magnetic field components can be expressed as:

$$\begin{aligned}
H_y &= -\frac{1}{i\omega\mu_0}\frac{\partial E_x}{\partial z} && \text{(A.16)}\\
H_x &= \frac{1}{i\omega\mu_0}\frac{\partial E_y}{\partial z} && \text{(A.17)}
\end{aligned}$$

which implies that the x-component of the magnetic field only depends on the y-component of the electric field and H_y only depends on the E_x. Unfortunately, this statement is non-reversible. In fact each of the horizontal components of electric field are dependent on the both horizontal components of magnetic field and this can be proved as follows:

Substituting (A.15) into (A.11) and (A.12) yields

$$\begin{aligned}
\frac{\partial H_y}{\partial z} &= -\left(\sigma_{xx} - \frac{\sigma_{xz}\sigma_{zx}}{\sigma_{zz}}\right)E_x - \left(\sigma_{xy} - \frac{\sigma_{xz}\sigma_{zy}}{\sigma_{zz}}\right)E_y\\
&= -A_{xx}E_x - A_{xy}E_y && \text{(A.18)}
\end{aligned}$$

and

$$\begin{aligned}\frac{\partial H_x}{\partial z} &= \left(\sigma_{yx} - \frac{\sigma_{yz}\sigma_{zx}}{\sigma_{zz}}\right) E_x + \left(\sigma_{yy} - \frac{\sigma_{yz}\sigma_{zy}}{\sigma_{zz}}\right) E_y \\ &= A_{yx}E_x + A_{yy}E_y \end{aligned} \tag{A.19}$$

in which

$$\begin{aligned} A_{xx} &= \sigma_{xx} - \frac{\sigma_{xz}\sigma_{zx}}{\sigma_{zz}}, \quad A_{xy} = \sigma_{xy} - \frac{\sigma_{xz}\sigma_{zy}}{\sigma_{zz}} \\ A_{yx} &= \sigma_{yx} - \frac{\sigma_{yz}\sigma_{zx}}{\sigma_{zz}}, \quad A_{yy} = \sigma_{yy} - \frac{\sigma_{yz}\sigma_{zy}}{\sigma_{zz}} \end{aligned}$$

with clearly $A_{xy} = A_{yx}$ for a symmetric conductivity tensor $\underline{\underline{\sigma}}$. Following (A.18) and (A.19) the horizontal components of electric field can be expressed as

$$E_x = \frac{-1}{A_{xx}A_{yy} - A_{xy}A_{yx}} \left(A_{xy}\frac{\partial H_x}{\partial z} + A_{yy}\frac{\partial H_y}{\partial z}\right) \tag{A.20}$$

$$E_y = \frac{1}{A_{xx}A_{yy} - A_{xy}A_{yx}} \left(A_{xx}\frac{\partial H_x}{\partial z} + A_{yx}\frac{\partial H_y}{\partial z}\right) \tag{A.21}$$

The induction equations in one-dimensional anisotropic structure can be easily derived through substituting (A.16) into (A.18) and (A.17) into (A.19):

$$\frac{\partial^2 E_x}{\partial z^2} + i\omega\mu_0 A_{xx}E_x + i\omega\mu_0 A_{xy}E_y = 0 \tag{A.22}$$

$$\frac{\partial^2 E_y}{\partial z^2} + i\omega\mu_0 A_{yx}E_x + i\omega\mu_0 A_{yy}E_y = 0 \tag{A.23}$$

These two equations express the fact that the horizontal components of electric field are dependent on each other because the existence of electric anisotropy and the induction equations build a coupled system. Therefore, to solve the forward problem of one-dimensional structures with electric anisotropy the both induction equations have to be solved simultaneously. Furthermore, the MT field in a layered anisotropic medium depends on the elements of the conductivity tensor solely through the cumulative conductivities $A_{ij},\ i,j \in (x,y)$. Whatever the particular form of the conductivity tensor $\underline{\underline{\sigma}}$, the electromagnetic field does not change if the elements of the 2×2 matrix A remain unchanged. This means the MT field of a plane wave does not allow us to resolve the full conductivity tensor in a one-dimensional medium without any additional information (see Pek and Santos, 2002).

If all the layers including the underlying half-space are isotropic, the conductivity becomes a scalar value instead of a tensor and the equations (A.11), (A.12) and (A.13) can be further simplified to:

$$\frac{\partial H_y}{\partial z} = -\sigma E_x \tag{A.24}$$

$$\frac{\partial H_x}{\partial z} = \sigma E_y \tag{A.25}$$

$$E_z = 0 \tag{A.26}$$

These equations together with (A.9), (A.10) and (A.14) show that only horizontal field components exist in one-dimensional isotropic medium and each component of electric field depends only on the perpendicular component of magnetic field and vice versa. The induction equations in one-dimensional isotropic structure can be formulated as

$$\frac{\partial^2 E_x}{\partial z^2} + i\omega\mu_0\sigma E_x = 0 \tag{A.27}$$

$$\frac{\partial^2 E_y}{\partial z^2} + i\omega\mu_0\sigma E_y = 0 \tag{A.28}$$

and they are no longer coupled, hence can be solved separately.

A.2.2. Two-dimensional structures

In two-dimensional (2D) structures we consider the conductivity varying in two directions. Let's say the y- and z-direction, if the same coordinate system as discussed in previous section is used. This means the location dependency of EM fields in x-direction is negligible, i.e., $\partial/\partial x = 0$.

Assuming a 2D structure which contains some anisotropic features. The Maxwell's equations

(2.15) and (2.16) for a frequency ω can be reduced to:

$$\frac{\partial E_z}{\partial y} - \frac{\partial E_y}{\partial z} = -i\omega\mu_0 H_x \tag{A.29}$$

$$\frac{\partial E_x}{\partial z} = -i\omega\mu_0 H_y \tag{A.30}$$

$$\frac{\partial E_x}{\partial y} = i\omega\mu_0 H_z \tag{A.31}$$

$$\frac{\partial H_z}{\partial y} - \frac{\partial H_y}{\partial z} = \sigma_{xx}E_x + \sigma_{xy}E_y + \sigma_{xz}E_z \tag{A.32}$$

$$\frac{\partial H_x}{\partial z} = \sigma_{yx}E_x + \sigma_{yy}E_y + \sigma_{yz}E_z \tag{A.33}$$

$$-\frac{\partial H_x}{\partial y} = \sigma_{zx}E_x + \sigma_{zy}E_y + \sigma_{zz}E_z \tag{A.34}$$

These equations show that all components of the EM fields exist and they are coupled with each other. The y- and z-components of magnetic field can be expressed by use of the x-component of the electric field. Equation (A.30) and (A.31) yield

$$H_y = -\frac{1}{i\omega\mu_0}\frac{\partial E_x}{\partial z} \tag{A.35}$$

$$H_z = \frac{1}{i\omega\mu_0}\frac{\partial E_x}{\partial y} \tag{A.36}$$

From equation (A.33) the z-component of the electric field can be stated as:

$$E_z = \frac{1}{\sigma_{yz}}\left(\frac{\partial H_x}{\partial z} - \sigma_{yx}E_x - \sigma_{yy}E_y\right) \tag{A.37}$$

Substituting (A.37) into (A.34) gives

$$E_y = \frac{\sigma_{yz}}{D}\frac{\partial H_x}{\partial y} + \frac{\sigma_{zz}}{D}\frac{\partial H_x}{\partial z} + BE_x \tag{A.38}$$

where

$$D = \sigma_{zz}\sigma_{yy} - \sigma_{yz}\sigma_{zy}, \quad B = (\sigma_{zx}\sigma_{yz} - \sigma_{zz}\sigma_{yx})/D \tag{A.39}$$

Substituting (A.38) into (A.37) yields

$$E_z = -\frac{\sigma_{yy}}{D}\frac{\partial H_x}{\partial y} - \frac{\sigma_{zy}}{D}\frac{\partial H_x}{\partial z} + AE_x \tag{A.40}$$

where

$$A = (\sigma_{yx}\sigma_{zy} - \sigma_{yy}\sigma_{zx})/D \tag{A.41}$$

The induction equations in 2D anisotropic structure can be derived through substituting (A.35), (A.36), (A.38) and (A.40) into (A.32) and (A.38), (A.40) into (A.29):

$$\frac{\partial^2 E_x}{\partial y^2} + \frac{\partial^2 E_x}{\partial z^2} + i\omega\mu_0(WE_x + A\frac{\partial H_x}{\partial y} - B\frac{\partial H_x}{\partial z}) = 0 \tag{A.42}$$

$$\begin{aligned}\frac{\partial}{\partial y}\left(\frac{\sigma_{yy}}{D}\frac{\partial H_x}{\partial y}\right) + \frac{\partial}{\partial z}\left(\frac{\sigma_{zz}}{D}\frac{\partial H_x}{\partial z}\right) + \frac{\partial}{\partial y}\left(\frac{\sigma_{yz}}{D}\frac{\partial H_x}{\partial z}\right) + \cdots \\ + \frac{\partial}{\partial z}\left(\frac{\sigma_{yz}}{D}\frac{\partial H_x}{\partial y}\right) + i\omega\mu_0 H_x - \frac{\partial\left(AE_x\right)}{\partial y} + \frac{\partial\left(BE_x\right)}{\partial z} = 0\end{aligned} \tag{A.43}$$

where

$$W = \sigma_{xx} + \sigma_{xy}B + \sigma_{xz}A \tag{A.44}$$

A,B and D are defined in equations (A.39) and (A.41).

They express that the x-component of the electric and magnetic field are coupled through the first partial derivative because the existence of electric anisotropy. Therefore, equations (A.42) and (A.43) have to be solved simultaneously. The MT field in a two-dimensional anisotropic medium depends on the elements of the conductivity tensor through 6 cumulative conductivities, namely σ_{yy}/D, σ_{zz}/D, σ_{yz}/D,A,B and W. Equations (A.39), (A.41) and (A.44) provide a unique linear transformation between the cumulative conductivities and the real conductivity tensor elements. In other words the full conductivity tensor is resolvable in a two- dimensional medium.

If the two-dimensional structure is isotropic, the conductivity becomes a scalar value and the equations (A.32), (A.33) and (A.34) can be further simplified to:

$$\frac{\partial H_z}{\partial y} - \frac{\partial H_y}{\partial z} = \sigma E_x \tag{A.45}$$

$$\frac{\partial H_x}{\partial z} = \sigma E_y \tag{A.46}$$

$$-\frac{\partial H_x}{\partial y} = \sigma E_z \tag{A.47}$$

The MT problem hence breaks down into two distinct modes, the Transverse Electric (TE) mode (or E-polarization) and the Transverse Magnetic (TM) mode (or B-polarization).

E-Polarization			B-Polarization		
$\frac{\partial H_z}{\partial y} - \frac{\partial H_y}{\partial z}$	$=$	σE_x	$\frac{\partial E_z}{\partial y} - \frac{\partial E_y}{\partial z}$	$=$	$-i\omega\mu_0 H_x$
$\frac{\partial E_x}{\partial z}$	$=$	$-i\omega\mu_0 H_y$	$\frac{\partial H_x}{\partial z}$	$=$	σE_y
$\frac{\partial E_x}{\partial y}$	$=$	$i\omega\mu_0 H_z$	$-\frac{\partial H_x}{\partial y}$	$=$	σE_z

The equations on the left contain only one horizontal electric field component (E_x) which oscillates parallel to the conductivity contrast and induced by a magnetic field (H_y) perpendicular to it. This is known as E-polarization and in this mode there does exist a vertical magnetic field (H_z). On the right hand side the case of B-polarization is described: a horizontal magnetic field (H_x) oscillates parallel to the conductivity contrast and induces a electric field (E_y) across the conductivity contrast and a vertical electric field (E_z).

The induction equations in two-dimensional isotropic structure can be formulated as

$$\frac{\partial^2 E_x}{\partial y^2} + \frac{\partial^2 E_x}{\partial z^2} + i\omega\mu_0\sigma E_x = 0 \tag{A.48}$$

$$\frac{\partial}{\partial y}\left(\frac{1}{\sigma}\frac{\partial H_x}{\partial y}\right) + \frac{\partial}{\partial z}\left(\frac{1}{\sigma}\frac{\partial H_x}{\partial z}\right) + i\omega\mu_0 H_x = 0 \tag{A.49}$$

and can be solved separately.

A.2.3. Three-dimensional structures

In three-dimensional (3D) structures we consider the conductivity varying in all the three spatial directions. In this case the general form of the Maxwell's equations, namely the equations (2.15) and (2.16), has to be considered. The induction equation for general 3D anisotropic structures is given by taking the curl of equations (2.15) and substituting $\nabla \times \mathbf{H}$ from equation (2.16):

$$\nabla \times \nabla \times \mathbf{E} - i\omega\mu_0 \underline{\underline{\sigma}}\mathbf{E} = 0 \tag{A.50}$$

If the electrical conductivity is independent of the spatial direction, the conductivity tensor $\underline{\underline{\sigma}}$ is reduced to scalar value σ.

A.3. One-dimensional (1D) structure with anisotropic conductivities

For horizontally layered isotropic media the 1-D magnetotelluric (MT) forward problem can be solved analytically. The electromagnetic fields and hence the impedances can be calculated at the boundaries between layers and consequently on the surface. An analytical solution of this problem is firstly derived by Wait (1954) and discussed in many publications, e.g.Weaver (1994), Simpson and Bahr (2005) and others. In this work I will not go into detail through this topic, the interested reader is referred to the publications cited above.

The 1-D MT forward problem for anisotropic layered media is a classical problem that has been considered in a series of studies, e.g. O'Brien and Morrison (1967), Reddy and Rankin (1970), Loewenthal and Landisman (1973), Abramovici (1974) and others. Recently, Pek and Santos (2002) presented a new algorithm, based on early work of Loewenthal et al and Abramovici, for jointly evaluating the MT impedances and their parametric sensitivities for 1-D layered media with generally anisotropic layers. This algorithm is further discussed by Li (2000). In the following paragraph, I will briefly summarize the definition of a 1-D MT model with anisotropic layers, as well as the key steps of the forward problem solution for that model. For details on particular aspects of the electromagnetic theory for anisotropic layered media and more detailed mathematical derivation the reader is referred to the previous chapter and of course the papers mentioned above.

A simple one-dimensional anisotropic layered model consists of N homogeneous horizontal layers with thicknesses $h_l,\ l = 1, \ldots, N$. The stack of layers is underlain by a homogeneous conductive halfspace (Fig. A.1). The electrical conductivity in each of the layers, as well as in the basement, is given by a conductivity tensor $\underline{\underline{\sigma_1}},\ l = 1, \ldots, N, N+1$.

I adopt the induction equations for 1-D anisotropic structure derived in previous chapter (Eqs.: A.22 and A.23) as a starting point.

$$\frac{\partial^2 E_x}{\partial z^2} + i\omega\mu_0 A_{xx} E_x + i\omega\mu_0 A_{xy} E_y = 0 \tag{A.51}$$

$$\frac{\partial^2 E_y}{\partial z^2} + i\omega\mu_0 A_{yx} E_x + i\omega\mu_0 A_{yy} E_y = 0 \tag{A.52}$$

where

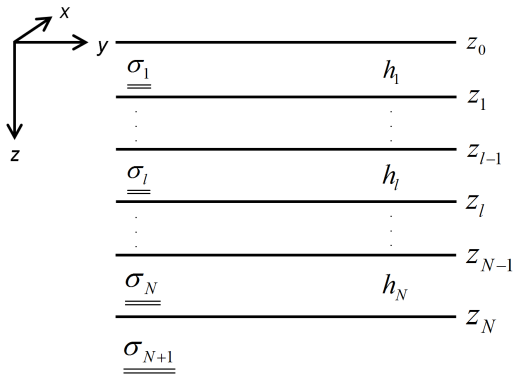

Figure A.1.: Cross-section of a simple one-dimensional anisotropic layered model. Electric anisotropy is characterized through conductivity tensor $\underline{\underline{\sigma_1}}$.

$$\begin{aligned} A_{xx} &= \sigma_{xx} - \frac{\sigma_{xz}\sigma_{zx}}{\sigma_{zz}}, \quad A_{xy} = \sigma_{xy} - \frac{\sigma_{xz}\sigma_{zy}}{\sigma_{zz}} \\ A_{yx} &= \sigma_{yx} - \frac{\sigma_{yz}\sigma_{zx}}{\sigma_{zz}}, \quad A_{yy} = \sigma_{yy} - \frac{\sigma_{yz}\sigma_{zy}}{\sigma_{zz}} \end{aligned}$$

and σ_{ij} represents an element of conductivity tensor $\underline{\underline{\sigma}}$.

Equations (A.51) and (A.52) are second-order linear differential equations. To solve both equations simultaneously two basic solutions can be considered.

$$E_x = Ce^{\pm kz}, \qquad E_y = De^{\pm kz} \tag{A.53}$$

Substituting (A.53) into (A.51) and (A.52) yields:

$$\begin{aligned} \left(k^2 + i\omega\mu_0 A_{xx}\right) C + \quad & i\omega\mu_0 A_{xy} D = 0 \\ i\omega\mu_0 A_{yx} C + & \left(k^2 + i\omega\mu_0 A_{yy}\right) D = 0 \end{aligned}$$

In order to ensure this homogeneous linear equation system has non-trivial solution (in other words, solution with $C, D \neq 0$), the determinant of the system coefficient matrix must equal zero, e.g.

$$\begin{vmatrix} k^2 + i\omega\mu_0 A_{xx} & i\omega\mu_0 A_{xy} \\ i\omega\mu_0 A_{yx} & k^2 + i\omega\mu_0 A_{yy} \end{vmatrix} = 0$$

which is equivalent to:

$$k^4 + i\omega\mu_0 \left(A_{xx} + A_{yy}\right) k^2 - \omega^2 \mu_0^2 \left(A_{xx}A_{yy} + A_{xy}A_{yx}\right) = 0 \tag{A.54}$$

Equation (A.54) has two solutions and they represent two different wave numbers in quadratic form

$$k_{1,2}^2 = -\frac{i\omega\mu_0}{2}\left[A_{xx} + A_{yy} \pm \sqrt{\left(A_{xx} - A_{yy}\right)^2 + 4A_{xy}A_{yx}}\right] \tag{A.55}$$

Consequently, the horizontal electric field component E_x can be formulated as a sum of 4 particular solutions which related to the wave numbers $\pm k_1$ and $\pm k_2$, respectively.

$$E_x = C^+ e^{k_1 z} + C^- e^{-k_1 z} + D^+ e^{k_2 z} + D^- e^{-k_2 z} \tag{A.56}$$

where vector C and D contain unspecified constants that scale the amplitudes of two upwards (C^+ and D^+) and downwards (C^- and D^-) diffusing wave modes.

Substituting (A.56) into (A.51) a general solution of E_y can be obtained

$$E_y = -Q_1 C^+ e^{k_1 z} - Q_1 C^- e^{-k_1 z} - Q_2 D^+ e^{k_2 z} - Q_2 D^- e^{-k_2 z} \tag{A.57}$$

where

$$Q_1 = \frac{i\omega\mu_0 A_{yx}}{k_1^2 + i\omega\mu_0 A_{yy}}, \qquad Q_2 = \frac{i\omega\mu_0 A_{yx}}{k_2^2 + i\omega\mu_0 A_{yy}}$$

Combine (A.9) and (A.10) with (A.55) and (A.56) general solutions of H_x and H_y can also be obtained

$$\begin{aligned} H_x &= \frac{1}{i\omega\mu_0}\frac{\partial E_y}{\partial z} \\ &= Q_1\xi_1 C^+ e^{k_1 z} - Q_1\xi_1 C^- e^{-k_1 z} + Q_2\xi_2 D^+ e^{k_2 z} - Q_2\xi_2 D^- e^{-k_2 z} \qquad \text{(A.58)} \\ H_y &= -\frac{1}{i\omega\mu_0}\frac{\partial E_x}{\partial z} \\ &= \xi_1 C^+ e^{k_1 z} - \xi_1 C^- e^{-k_1 z} + \xi_2 D^+ e^{k_2 z} - \xi_2 D^- e^{-k_2 z} \qquad \text{(A.59)} \end{aligned}$$

where

$$\xi_1 = -\frac{k_1}{i\omega\mu_0}, \qquad \xi_2 = -\frac{k_2}{i\omega\mu_0}$$

Equations (A.55) to (A.59) form a linear equation system and can be expressed in matrix format as

$$\underbrace{\begin{pmatrix} E_x \\ E_y \\ H_x \\ H_y \end{pmatrix}}_{F(z,\omega)} = \underbrace{\begin{pmatrix} e^{k_1 z} & e^{-k_1 z} & e^{k_2 z} & e^{-k_2 z} \\ -Q_1 e^{k_1 z} & -Q_1 e^{-k_1 z} & -Q_2 e^{k_2 z} & -Q_2 e^{-k_2 z} \\ Q_1\xi_1 e^{k_1 z} & -Q_1\xi_1 e^{-k_1 z} & Q_2\xi_2 e^{k_2 z} & -Q_2\xi_2 e^{-k_2 z} \\ \xi_1 e^{k_1 z} & -\xi_1 e^{-k_1 z} & \xi_2 e^{k_2 z} & -\xi_2 e^{-k_2 z} \end{pmatrix}}_{M_(z,\omega)} \underbrace{\begin{pmatrix} C^+ \\ C^- \\ D^+ \\ D^- \end{pmatrix}}_{X} \tag{A.60}$$

The vector X contains arbitrary multiplicative constants. Since all the horizontal field components are continuous on the layer boundaries, which is ensured by the general continuity conditions, a connection of two neighboring layers can be hence established,

$$F_l(z_l,\omega) = F_{l+1}(z_l,\omega) \quad \text{or} \quad M_l(z_l,\omega)X_l = M_{l+1}(z_l,\omega)X_{l+1} \tag{A.61}$$

where $l = 1,\ldots,N$. Consequently, the field within the $l-$th layer can be written in the form

$$F_l(z_l,\omega) = M_l(z_l,\omega)X_l = \prod_{j=l+1}^{N} M_j(z_{j-1},\omega)M_j^{-1}(z_j,\omega)M_{N+1}(z_N,\omega)X_{N+1} \tag{A.62}$$

Equation (A.62) defines the horizontal field components on arbitrary layer boundaries. Within one particular layer the vector X remains unchanged and the field distribution hence sorely depends on the depth $z \in [z_{l-1}, z_l]$. Summarize (A.61) and (A.62) the field inside a particular layer can be computed through

$$\begin{aligned} F_l(z,\omega) &= M_l(z,\omega)X_l \qquad (A.63) \\ &= M_l(z,\omega)M_l^{-1}(z_l,\omega)\prod_{j=l+1}^{N} M_j(z_{j-1},\omega)M_j^{-1}(z_j,\omega)M_{N+1}(z_N,\omega)X_{N+1} \end{aligned}$$

The only unknown in equation (A.63 is the vector X related to the homogenous basement (where $z > N+1$). The upwards diffusing wave modes must vanish in homogeneous basement (where $z > N+1$) for energetic reasons, i.e., $C^+ = D^+ = 0$, otherwise they would increase to infinity for $z \to \infty$. Only downwards diffusing wave modes exist in the basement. Since no electric field exists in Air above the layered Earth model the remained constants C^- and D^- can be obtained by using of normalized magnetic field defined on the Earth/Air interface.

A.4. Conjugate Gradient (CG) method and the preconditioned Conjuagte Gradient (PCG) method

Algorithm 1 A example of Conjugate Gradients algorithm. Given the inputs $\mathbf{A}, \mathbf{b}$ and a starting value of $\mathbf{x}$, a maximum number of iterations i_{max} and an error tolerance $\epsilon < 1$. In each iteration a conjugate direction $\mathbf{d}$ and a approximated solution $\mathbf{x}$ are computed.

$i = 0$
$\mathbf{r} = \mathbf{b} - \mathbf{A}\mathbf{x}$
$\mathbf{d} = \mathbf{r}$
$\delta_{new} = \mathbf{r}^T\mathbf{r}$
$\delta_0 = \delta_{new}$
while $i < i_{max}$ and $\delta_{new} > \epsilon^2\delta_0$ **do**
  $\mathbf{q} = \mathbf{A}\mathbf{d}$
  $\alpha = \frac{\delta_{new}}{\mathbf{d}^T\mathbf{q}}$
  $\mathbf{x} = \mathbf{x} + \alpha\mathbf{d}$
  $\mathbf{r} = \mathbf{r} - \alpha\mathbf{q}$
  $\delta_{old} = \delta_{new}$
  $\delta_{new} = \mathbf{r}^T\mathbf{r}$
  $\beta = \frac{\delta_{new}}{\delta_{old}}$
  $\mathbf{d} = \mathbf{r} + \beta\mathbf{d}$
  $i = i + 1$
end while

Algorithm 2 A example of preconditioned Conjugate Gradients algorithm. Given the inputs $\mathbf{A}, \mathbf{b}$ and a starting value of $\mathbf{x}$, a preconditioner $\mathbf{M}$ (perhaps implicitly defined), a maximum number of iterations i_{max} and an error tolerance $\epsilon < 1$. In each iteration a conjugate direction $\mathbf{d}$ and a approximated solution $\mathbf{x}$ are computed.

$i = 0$
$\mathbf{r} = \mathbf{b} - \mathbf{A}\mathbf{x}$
$\mathbf{d} = \mathbf{M}^{-1}\mathbf{r}$
$\delta_{new} = \mathbf{r}^T\mathbf{d}$
$\delta_0 = \delta_{new}$
while $i < i_{max}$ and $\delta_{new} > \epsilon^2\delta_0$ **do**
  $\mathbf{q} = \mathbf{A}\mathbf{d}$
  $\alpha = \frac{\delta_{new}}{\mathbf{d}^T\mathbf{q}}$
  $\mathbf{x} = \mathbf{x} + \alpha\mathbf{d}$
  $\mathbf{r} = \mathbf{r} - \alpha\mathbf{q}$
  $\mathbf{s} = \mathbf{M}^{-1}\mathbf{r}$
  $\delta_{old} = \delta_{new}$
  $\delta_{new} = \mathbf{r}^T\mathbf{s}$
  $\beta = \frac{\delta_{new}}{\delta_{old}}$
  $\mathbf{d} = \mathbf{s} + \beta\mathbf{d}$
  $i = i + 1$
end while

A.5. Implementation details

A.5.1. Transformations of model parameter

In an anisotropic material the conductivity is represented by a second rank, tensor $\underline{\underline{\sigma}}$, which is symmetric and positive definite (for detailed discussion the reader is referred to section 2.2). At a point (x, y, z) in a Cartesian coordinate system the second-rank conductivity tensor can be denoted as

$$\underline{\underline{\sigma}} = \begin{pmatrix} \sigma_{xx} & \sigma_{xy} & \sigma_{xz} \\ \sigma_{yx} & \sigma_{yy} & \sigma_{yz} \\ \sigma_{zx} & \sigma_{zy} & \sigma_{zz} \end{pmatrix} \tag{A.64}$$

The induction equation for 2D anisotropic structure can be derived from Maxwell's equation with considering of the conductivity tensor (see also section A.2.2) $\underline{\underline{\sigma}}$.

$$\frac{\partial^2 E_x}{\partial y^2} + \frac{\partial^2 E_x}{\partial z^2} + i\omega\mu_0 \left(\pi_1 E_x + \pi_2 \frac{\partial H_x}{\partial y} + \pi_3 \frac{\partial H_x}{\partial z} \right) = 0 \tag{A.65}$$

$$\frac{\partial}{\partial y}\left(\pi_4 \frac{\partial H_x}{\partial y}\right) + \frac{\partial}{\partial z}\left(\pi_5 \frac{\partial H_x}{\partial z}\right) + \frac{\partial}{\partial y}\left(\pi_6 \frac{\partial H_x}{\partial z}\right) + \frac{\partial}{\partial z}\left(\pi_6 \frac{\partial H_x}{\partial y}\right) + i\omega\mu_0 H_x - \frac{\partial\left(\pi_2 E_x\right)}{\partial y} + \frac{\partial\left(\pi_3 E_x\right)}{\partial z} = 0 \tag{A.66}$$

where $\pi = (\pi_1, \pi_2, \pi_3, \pi_4, \pi_5, \pi_6)$ and denotes cumulative conductivities $\pi_j \, (j \in [1, 6])$, which is an algebraic combination of several elements of $\underline{\underline{\sigma}}$. The explicit expression of each element of π can be obtained by following equations (A.39) to (A.44). Hence, one can define a function $\pi = f(\underline{\underline{\sigma}})$.

A symmetric and positive definite tensor can always be diagonalised and expressed as three principal values and three rotation angles (see section 2.2 for detailed discussion). In other words, the tensor $\underline{\underline{\sigma}}$ can be transformed to

$$\eta = (\sigma_1, \sigma_2, \sigma_3, \alpha, \beta, \gamma) \tag{A.67}$$

where $\sigma_{1,2,3}$ are the three principal values of the diagonalised tensor and α, β and γ are the three rotation angles. The transformation can also be defined as a function, which yields $\underline{\underline{\sigma}} = f(\eta)$.

It is obvious that the expression with three principal values and three rotation angles (eq. A.67) gives an intuitive description of the spatial orientation of the different conductivity values. The full tensor form (eq. A.64) is the mathematical definition of the anisotropic conductivity based on a predefined coordinate system and serves as a transition between η and π. The cumulative conductivity π has no direct physical meaning but it is very convenient from the numerical point of view to formulate the induction equation in terms of π.

The parametric sensitivity of any MT response function F is defined as its first derivative with respect to model parameter $\mathbf{m}$. Thus, the i-th element of the sensitivity matrix can be then derived through

$$\frac{\partial F}{\partial m_i} = \frac{\partial F}{\partial \eta_i} = \sum_{j=1}^{6} \frac{\partial F}{\partial \pi_j} \left(\sum_{k=1}^{6} \frac{\partial \pi_j}{\partial \sigma_k} \frac{\partial \sigma_k}{\partial \eta_i} \right) \tag{A.68}$$

For the right hand side of equation (A.68), the term left of the brackets depends on physical nature and numerical discretization and can be computed following the discussion in previous section. In contrast, the term in brackets is a pure mathematical operator and easy to calculate. Thus, it is convenient to implement the term in brackets as an independent subroutine which only need to be invoked once for each inversion iteration after the calculation of the term left of the brackets is finished.

A.5.2. Model roughness matrix R and the anisotropy matrix K

The matrix $\mathbf{R}$ represents the so-called roughness matrix and the product $\mathbf{R}^T\mathbf{R}$ builds the inverse of model covariance matrix $\mathbf{C}^{-1}$ which is required by the penalty functional to be minimized and for calculating the model update. Within a discretized model space, the product of roughness matrix $\mathbf{R}$ and model parameter $\mathbf{m}$ can be considered as the first derivative between the adjacent model parameters. For 2D case, the roughness matrix $\mathbf{R}$ consists of two roughening matrices in horizontal y- and vertical z-directions (DeGroot-Hedlin and Constable, 1990).

$$\mathbf{R} = \mathbf{W}\mathbf{R}_y + \mathbf{R}_z = \mathbf{W} \begin{pmatrix} 1 & -1 & \cdots & 0 \\ 0 & 1 & -1 & \vdots \\ \vdots & \cdots & \ddots & \vdots \\ 0 & \cdots & 0 & 1 \end{pmatrix} + \begin{pmatrix} -1 & \cdots & 0 & 1 & 0 & 0 & \cdots \\ 0 & -1 & \cdots & 0 & 1 & 0 & \cdots \\ & & \ddots & & & \ddots & \\ & & & -1 & & \cdots & 1 \\ & & & \mathbf{0} & & & \end{pmatrix} \tag{A.69}$$

Suppose the grid consist of a total of N elements, with N_y elements in the horizontal direction and N_z elements in the vertical direction. $\mathbf{R}_y$, $\mathbf{R}_z$ and $\mathbf{W}$ are the $N \times N$ matrices, where $\mathbf{W}$ containing the ratio of cell dimension in vertical and horizontal direction, e.g. $\Delta z/\Delta y$, and $\mathbf{0}$ is a $N_y \times N$ matrix of zeros. There are $N_y - 1$ zeros between the entries in the rows of $\mathbf{R}_z$. Thus, $\mathbf{R}_y$ and $\mathbf{R}_z$ difference the model parameters between horizontally and vertically adjacent blocks, respectively.

The matrix $\mathbf{K}$ defines the degree of anisotropy in the studied model domain. As already discussed in previous section, the positive semi-definite matrix $\mathbf{K}$ has the form of a discretized Laplacian and its purpose is to make the principal conductivities equal. A typical form of $\mathbf{K}$ would be

$$\mathbf{K} = \begin{pmatrix} 2 & -1 & -1 \\ -1 & 2 & -1 \\ -1 & -1 & 2 \end{pmatrix}$$

Therefore, the anisotropy of a particular grid cell k can be expressed as

$$\text{anisotropy of cell } k = (\sigma_{k1}, \sigma_{k2}, \sigma_{k3}) \begin{pmatrix} 2 & -1 & -1 \\ -1 & 2 & -1 \\ -1 & -1 & 2 \end{pmatrix} \begin{pmatrix} \sigma_{k1} \\ \sigma_{k2} \\ \sigma_{k3} \end{pmatrix}$$

If the grid consists of a total of N elements, the model parameter $\mathbf{m}$ is then a vector of length $6N$

$$\mathbf{m} = (\underbrace{\cdots \sigma_{k1} \cdots}_{\text{length of } N}, \cdots \sigma_{k2} \cdots, \cdots \sigma_{k3} \cdots, \cdots \alpha_k \cdots, \cdots \beta_k \cdots, \cdots \gamma_k \cdots)$$

Hence, the anisotropy matrix $\mathbf{K}$ for all grid cells can be organized in a matrix with dimension of $6N \times 6N$

$$\mathbf{K} = \begin{pmatrix} 2 & 0 & \cdots & -1 & 0 & \cdots & -1 & 0 & \cdots & \\ 0 & 2 & 0 & & -1 & 0 & & -1 & & \\ \vdots & & \ddots & & & \ddots & & & \ddots & \\ -1 & 0 & & 2 & 0 & & -1 & & & \\ 0 & -1 & 0 & & 2 & 0 & & -1 & & \mathbf{0} \\ \vdots & & \ddots & & & \ddots & & & \ddots & \\ -1 & 0 & & -1 & 0 & & 2 & 0 & & \\ 0 & -1 & 0 & & -1 & 0 & & 2 & & \\ \vdots & & \ddots & & & \ddots & & & \ddots & \\ & & & & \mathbf{0} & & & & & \mathbf{0} \end{pmatrix}$$

where **0** is a $3N \times 3N$ matrix of zeros. Hence, the anisotropy penalty $\Phi(\mathbf{m})$ can be expressed as $\mathbf{m}^T\mathbf{K}\mathbf{m}$.

A.6. Influence of CG iteration number on inversion model

When the conjugate gradient method is used to solve the least-squares equation (4.41), the inversion procedure will involve two levels of iteration, e.g there will be two loops in the inversion procedure. The outer loop is the iteration of the least-squares equation, while the inner loop is the iteration of the conjugate gradient procedure that is used to solve for the approximate model update at each iteration of inversion. The question, how many CG iterations are required in order to ensure a reliable accuracy of model update at each inversion iteration, is an issue of contention. Some authors suggest that only few CG iterations are necessary at each inversion iteration since one must update the model and begin the whole process again (e.g. Mackie and Madden, 1993b). In this particular test, I found that the number of desired CG iteration for each inversion iteration is a factor which affects the appearance of the inversion model and the rate of convergence of the inversion, hence should be treated with care.

To examine how the maximal allowed CG iteration number will affect the inversion model, I reuse one of the inversion runs performed in previous subsection. For this inversion test the structural and the anisotropy penalty parameters are fixed to 1000.0 and 1.0, respectively. Other inversion settings remain unchanged as described in previous subsection except the number of CG iteration for each inversion iteration. Three test inversion runs are carried out with 20, 100 and 200 as the maximal allowed CG iteration number for each inversion iteration. All three tests are performed with a maximal allowed number of inversion iteration of 25 and the initial model is a homogeneous isotropic half-space with resistivity of $100\,\Omega\mathrm{m}$ and the results are displayed in figures A.2, A.3 and A.4, respectively. Each figure consists of three panels, in the upper panel the resolved principal resistivities ρ_x, ρ_y and ρ_z are displayed as image arrays against the inversion iterations, in the middle panel the percentage anisotropy is shown for all the 25 inversion iterations, in the lower panel the root mean square (RMS) error is displayed as a function of the number of the inversion iteration. In general, all the three inversion tests are able to resolve the anomalous structure in the model and the resolved principal resistivities are all (except the z-component for known reason, see previous subsection) approximate the real resistivity values of $50\,\Omega\mathrm{m}$ in x-direction and $10\,\Omega\mathrm{m}$ in

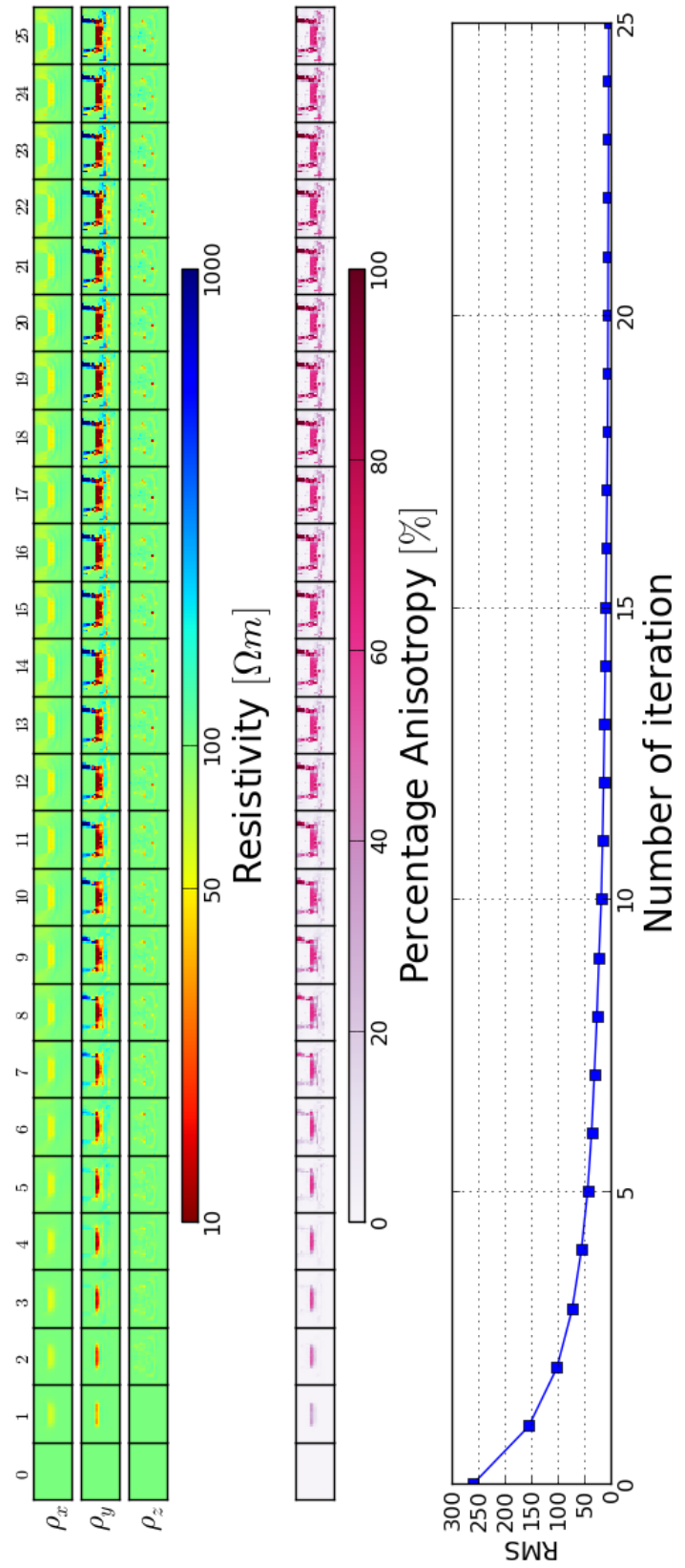

Figure A.2.: Inversion of synthetic data by applying fixed penalty level of $\lambda_s = 1000$ and $\lambda_a = 1$), the maximal number of CG iteration is set to 20. In rows one to three the resolved principal resistivities $\rho_{x,y,z}$ are plotted as image arrays against the number of inversion iteration. In row four, percentage anisotropy (derived from $\rho_{x,y,z}$) are displayed. In row five, the RMS error is plotted as a function of the number of inversion iteration.

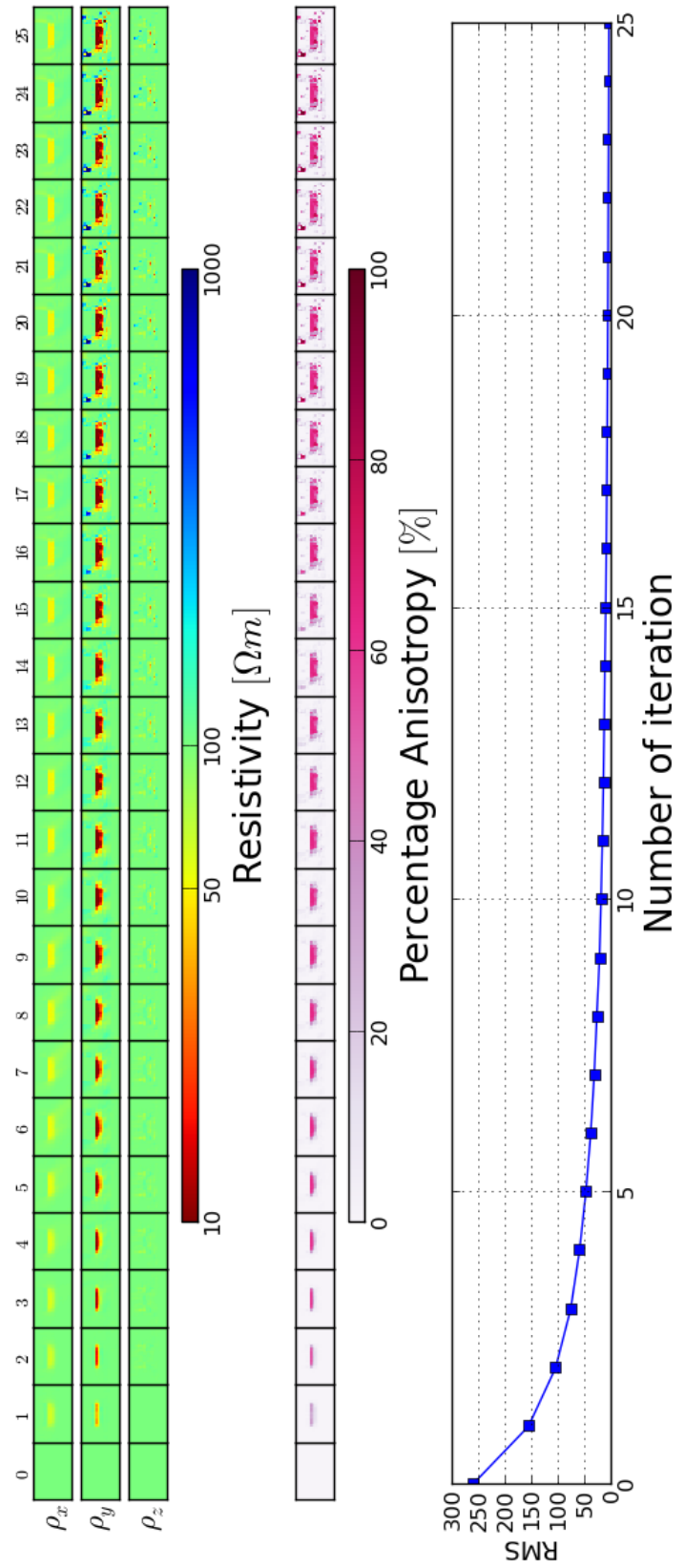

Figure A.3.: Inversion of synthetic data by applying fixed penalty level of $\lambda_s = 1000$ and $\lambda_a = 1$), the maximal number of CG iteration is set to 50. In rows one to three the resolved principal resistivities $\rho_{x,y,z}$ are plotted as image arrays against the number of inversion iteration. In row four, percentage anisotropy (derived from $\rho_{x,y,z}$) are displayed. In row five, the RMS error is plotted as a function of the number of inversion iteration.

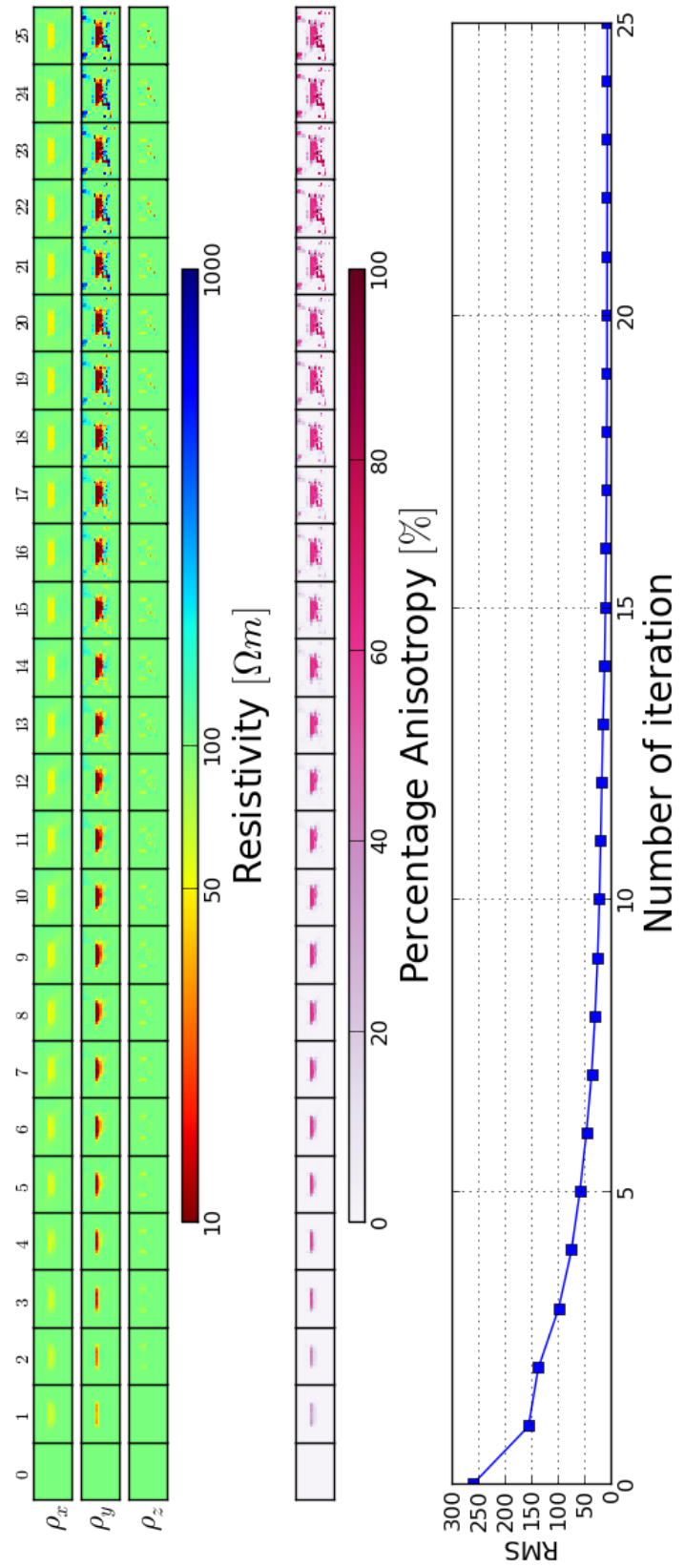

Figure A.4.: Inversion of synthetic data by applying fixed penalty level of $\lambda_s = 1000$ and $\lambda_a = 1$), the maximal number of CG iteration is set to 100. In rows one to three the resolved principal resistivities $\rho_{x,y,z}$ are plotted as image arrays against the number of inversion iteration. In row four, percentage anisotropy (derived from $\rho_{x,y,z}$) are displayed. In row five, the RMS error is plotted as a function of the number of inversion iteration.

y-direction. The anomalous structure shows distinct anisotropy both in the view of principal resistivities and in the percentage anisotropy. All three inversions converge well, after 25 inversion iterations the RMS error for all three tests are below 5. But one can observe clear differences if we compare the inversion results. For the first test, where only 20 CG iterations are allowed for each inversion iteration, the predefined norm of residual with value of 1.0×10^{-5} is never reached and the CG iteration is always terminated when the maximal allowed number of CG iterations is executed. One can observe that artificial structure started to create at an early stage (after only 5 inversion iterations) due to rough accuracy of the solution at each inversion iteration (see figure A.2). In contrast, with a maximal allowed CG iteration number of 100 and 200 the solutions (the model update) computed at each inversion iteration are more accurate. No artificial structure is created until the inversion reached a relatively stable stage, where large-scale structure has been created and the RMS error falls down to a significantly small level (e.g. 15 inversion iteration; see figures A.3 and A.4). After 15 inversion iterations only small-scale structure is created and the inversion procedure starts a "fine tuning". In this later stage we observe that for the test with 100 CG iterations for each inversion iteration few slight structures are created above the "true" anomalous structure. For the test with 200 CG iterations for each inversion iteration, more artificial structures are created both above and below the "true" anomalous structure. This phenomenon can be explained as following: at the early stage, where the large-scale structure is created, the round-off error of each inversion iteration is insignificant compares to the model update, while at the later stage, where only small-scale structure is created, the model update becomes small and the round-off error becomes comparable to the model update. Since the CG method is an iterative method and because the solution is small, it will hold that the more the procedure iterates, the bigger the accumulated round-off error will be. Hence I may deduce that applying different number of CG iteration does change the inversion model and set the CG iteration number to 100 seems to be the best choice for this particular test.